Novel Trapping Techniques For Shaping Bose-Einstein Condensates

by

Micah Boyd

Submitted to the Department of Physics
in partial fulfillment of the requirements for the degree of

Doctor of Philosophy

at the

MASSACHUSETTS INSTITUTE OF TECHNOLOGY

October 2006

© Massachusetts Institute of Technology 2006. All rights reserved.

Author .....
Department of Physics
October 24, 2006

Certified by .....
Wolfgang Ketterle
John D. MacAurthur Professor of Physics
Thesis Supervisor

Certified by .....
David E. Pritchard
Cecil and Ida Green Professor of Physics
Thesis Supervisor

Accepted by .....
Thomas J. Greytak
Professor of Physics, Associate Department Head for Education

Novel Trapping Techniques For Shaping Bose-Einstein Condensates

by

Micah Boyd

Submitted to the Department of Physics
on October 24, 2006, in partial fulfillment of the
requirements for the degree of
Doctor of Philosophy

Abstract

A combination of radio frequency radiation and magnetic field gradients was used to trap atoms in dressed states. In a magnetic field with a quadrupole minimum, RF fields resonant with the $(|F, m_f\rangle)$ $|1, -1\rangle \rightarrow |1, 0\rangle$ transition trapped the atoms on the surface of a sphere, and gravity caused the atoms to pool at the bottom of the sphere. BECs were transferred into this dressed Zeeman trap with 100% efficiency, with lifetimes of up to 30 s, and trapping frequencies of up to 250 Hz were measured.

A hard disk platter with a specially written magnetic pattern was used to generate magnetic fields to confine atoms tightly. Detrimental interactions with the surface were avoided by using an extremely thin film with a large magnetic remnant. BECs of up to 5×10^4 atoms were produced in cigar shaped traps $\sim$40 μm above the surface, and trap frequencies up to 5 kHz were measured. After evaporation, condensed clouds moved closer to the surface to probe imperfections in the magnetic potential, revealing defects at distances closer than 35 μm. Finally, BECs were dropped from a height of 350 μm in an attempt to achieve specular reflection, but a large amount of dispersion was observed.

Finally, BECs were loaded into a three-dimensional optical lattice, and a quantum phase transition from a superfluid to a Mott insulator was observed. Using microwave spectroscopy, the density dependent "clock shift" was was found to depend on the occupation number of the wells. The singly occupied lattice sites were then investigated as an atomic clock system with no density shift. Linewidths as small as 1 Hz FWHM out of 6.8 GHz are comparable to current atomic frequency standards.

Thesis Supervisor: Wolfgang Ketterle
Title: John D. MacAurthur Professor of Physics

Thesis Supervisor: David E. Pritchard
Title: Cecil and Ida Green Professor of Physics

To my wife Karin

Without whom this work would be empty.

Acknowledgments

Naivete and optimism.

Those probably best described my mental state as I walked into the empty lab on my first day. When I joined the Ketterle group, I was assigned to the still imaginary Rubidium lab. We had some temporary space to start work while our destination lab was being renovated, but no optics table, no racks, no drawers, nothing. The task before us was daunting, but eventually came success.

I started in the lab with fellow graduate student Erik Streed, and together we built the bulk of the machine. I'd like to thank Erik for his keen wit, awesome hat, and being a friend as well as a co-worker. We were soon joined by postdoc Yoshio Torii, whose delicate command of the optics table impresses me to this day. Then came Dominik Schneble. Fresh from his own Ph.D., he led the lab out of the dark ages of construction into the first breaths of the golden age of experiment. I'd like to thank Dominik for his leadership, his science, but most of all his insightful advice.

Soon after Dominik came another new graduate student, Gretchen Campbell. Quiet as a churchmouse, and humble as a nun, a few years in the Rubidium lab changed her. Now she breathes a fire of science, and everything she touches turns to gold. Gold or a Science paper. Kind of a science Midas, except probably nicer. I really can't thank her enough for all her help, motivation, help, coffee breaks, help, procrastination, and smart discussions over the years, and I'm sure that she will meet unparalleled success in her academic career.

Jongchul Mun also deserves his thanks. Blessed with Yoshio's skill at the optics table, and an incredible deal of patience, I am sure that he will blaze new trails with the lab. Patrick Medley is the youngest member in the lab, but his day of leadership will soon be upon him. I am certain that his enthusiasm and intelligence will bring him much success, and I thank him for his efforts when we worked as a team. As a postdoc, Aaron Leanhardt deserves special recognition. I learned a tremendous amount about science, patience and experimental stamina from him, and for this he has my thanks. I would also like to thank Luis Marcassa for all his help in the time

he has been here on his sabbatical, doing all the mundane and dirty things that a professor thinks he will never have to do again.

The Rubidium lab is certainly not the only lab in the Ketterle group, and I have many Sodium friends who also deserve thanks, even though they are forced to work with a lesser element. Tom Pasquini, as of right now a new father of twins, deserves my thanks for getting all of us a raise, giving incredibly useful feedback when reading papers, being an awesome guy, and being a friend. I hope that he will be as patient a father as you are a scientist, and that you use your powers for good, as well as for awesome. Dan Miller has a special place in my heart as a gracious host for some "memorable" parties, as well as keeping up the general lab morale. I am sure that the John Harvard statue will be relieved when Dan graduates. Jamil Abo-Shaeer left the lab quite a while ago, but his presence is still felt, and missed. He set a standard for shenanigans, tomfoolery and the fine french art of *grabáss* that will only be imitated for years to come. He was, and still is, my friend.

I would also like to thank Min Xiao and Liesl Folks at Hitachi Global Storage Technologies. They provided invaluable guidance during my pursuit of the hard disk platter project, and Min spent many hours preparing disks for me to put in vacuum. Her willingness to donate her time gave the project life, and I very much appreciate it.

I'd like to thank Jit-Kee Chin and Yingmei Liu for their patience as I repeatedly scoured their lab for various pieces of equipment I claimed they had stolen, only to discover that I had only hidden it from myself. Speaking of stealing, my thanks also goes to Widagdo Setiawan for his secret stash of RF components and electronics. Professor Martin Zwierlein, a character if there ever was one, has my thanks for his brilliant scientific discussions and enthusiastic renditions of Beatles songs. He also has my thanks in advance in case I ever need a job (blackmail). My thanks goes to Andre Schirotzek for his inappropriate German comments and his chiropractic skills, and to Christian Schunck for being both hilarious and a good travel partner. Yong-Il Shin, Caleb Christensen, Peter Zarth, Gyu-Boong Jo, Ye-ryoung Lee, and Sebastian Will, thanks for your help, discussions, lunch money, and laughs. It is people like you

who make stuff like this worth it.

Speaking of worth it, I don't really know how to thank my wife Karin enough. How she ever put up with my bizarre schedule, long hours, and broken experiment bad moods, I'll never know. Hopefully, any future problems will seem small in comparison. Thank you.

Finally, I would like to thank Dave Pritchard and Wolfgang Ketterle. From inviting me to join their group in the beginning, to fatherly career advice at the end, I could not have asked for better advisors.

Contents

List of Figures

Chapter 1

Introduction

1.1 In the Beginning

In the beginning, there was an empty room. Construction of the ^{8}7Rb Bose-Einstein condensate (BEC) machine started in the Fall of 2000, and the first BECs were produced a little more than a year later.

1.2 Bose-Einstein Condensation

It is somewhat of an atomic physics thesis tradition to give a brief overview of BEC in the preferred style of the writer, and I won't break this tradition. Starting from the de Broglie wavelength

$$\lambda_T = \sqrt{\frac{2\pi\hbar^2}{mk_BT}} \tag{1.1}$$

where m is the mass of one particle, k_B is Boltzmann's constant, and T is the temperature, matter-wave overlap occurs in a regime where λ_T becomes comparable the spacing between atoms, $\Delta x = n^{-1/3}$. Thus the phase transition to BEC occurs at (or near) a phase space density of $\lambda_T^3 n \approx 1$. Conveniently, this simple description is very close to the actual phase space density required ($\lambda_T n^{-1/3} \approx 2.612$) to create a quantum saturated vapor where all thermally accessible states are occupied. The

critical density required can be expressed as

$$\frac{N}{V} = \zeta(3/2)\left(\frac{mk_BT}{2\pi\hbar^2}\right)^{3/2} \tag{1.2}$$

where $\zeta(3/2) \approx 2.612$ is the Riemann Zeta function. In the case of harmonically confined atoms with trap frequencies $(\omega_x, \omega_y, \omega_z)$, the excitation energies are $\epsilon(n_x, n_y, n_z) = (n_x + 1/2)\hbar\omega_x + (n_y + 1/2)\hbar\omega_y + (n_z + 1/2)\hbar\omega_z$, resulting in a critical temperature

$$T_c = \frac{\hbar\bar{\omega}}{k_B}\left(\frac{N}{\zeta(3)}\right)^{1/3} \tag{1.3}$$

where $\bar{\omega} = (\omega_x\omega_y\omega_z)^{1/3}$ and $\zeta(3) \approx 1.202$. For a typical experimental value of $N = 10^6$ and $\bar{\omega} = 50$ Hz, we must achieve $T_c < 225$ nK and a density of $n > 4 \times 10^{13}$ atoms / cm^3. Most BEC experiments work in parameter regimes within two orders of magnitude of these values.

1.2.1 Chemical Potential

Once the condensate has been formed, all of the atoms are described by a single wavefunction. Adding a term to the Schrödinger equation to account for atom-atom interactions yields the Gross-Pitaevskii equation,

$$\left(-\frac{\hbar^2}{2m}\bigtriangledown^2 + V(\vec{r}) + \frac{4\pi\hbar^2 a}{m}|\psi(\vec{r})|^2\right)\psi(\vec{r}) = \mu\psi(\vec{r}), \tag{1.4}$$

where $V(\vec{r})$ is the magnitude of the trapping potential, a is the s-wave scattering length between two atoms, and μ is the chemical potential. The regime where the atom-atom interaction energy is large compared to the kinetic energy is called the Thomas-Fermi limit, and we may rewrite the wavefunction as

$$\left(V(\vec{r}) + \frac{4\pi\hbar^2 a}{m}|\psi(\vec{r})|^2\right)\psi(\vec{r}) = \mu\psi(\vec{r}). \tag{1.5}$$

This equation may be solved in terms of the local density

$$|\psi(\vec{r})|^2 = n(\vec{r}) = \frac{m}{4\pi\hbar^2 a}[\mu - V(\vec{r})]. \tag{1.6}$$

One can simply imagine a pool of atoms filling the trapping potential to a constant height (μ). This chemical potential also sets the time evolution of the wavefunction as $\Psi(\vec{r}, t) = \psi(\vec{r})e^{-i\mu t/\hbar}$,

The chemical potential μ is a measure of interaction between the atoms which is constant throughout the cloud, and is one of the properties of the BEC most relevant to work in this thesis. The chemical potential may be calculated quickly from $\mu = 4\pi\hbar^2 a n_0/m$, where n_0 is the peak density of the atomic cloud. The ratio between μ and any trapping potentials or perturbations greatly affects the behavior of the atomic system.

1.2.2 Experimental Realization

Since its first observation in dilute atomic gasses, BEC has been achieved with the entire first column of the periodic table (except for francium, in order of atomic mass [21, 4, 12, 48, 1, 78]), metastable ^{4}He [53], ^{52} Cr [25], and ^{174}Yb [74]. In fact, what was once the goal is now only a tool; BECs are used to model solid state systems, probe interactions with surfaces, and measure properties of the atoms themselves, sometimes with great precision.

1.3 Lower Dimensional Systems

One area of great interest in ultracold gas research is systems with reduced dimensionality. While it is easy to make a BEC[1] in three dimensions, it is quite difficult to solve many of the relevant equations of motion in three dimensions. Contrapositively, many two and one-dimensional systems are theoretically rich, but extremely difficult to achieve experimentally. Sometimes reducing the dimensionality of a system can

[1]Correction: Easy to make the *second* BEC.

make solutions to the wavefunction simpler, such as the case in two dimensions with the Kosterlitz-Thouless transition [39] and in one dimension with the Tonks gas [50]. One characteristic of both of these phenomena is the increase of phase fluctuations which may destroy the coherence across the atomic cloud. Studies in these regimes thus may not deal with BEC at all in the end, but it's a good place to start. The three main experiments described in this thesis follow a general theme of shaping the confining potential in such a way to remove degrees of freedom from the system.

1.4 Outline

The outline of this thesis follows an order of reduction of atomic motion. First, I discuss an experiment using adiabatic potentials to trap an atomic cloud in two dimensions called the "Dressed Zeeman Trap." Second, I describe an experiment using magnetic thin films to trap atoms in one dimension called the "Hard Disk Platter Trap." Lastly, I detail work done in an optical lattice, where removing all motional degrees of freedom eliminated detrimental effects of inter-atomic interactions, creating the "Mott Insulator Atomic Clock".

Chapter 2

Bose-Einstein Condensate Production

A detailed description of the construction of the ^{87}Rb BEC machine can be found in Erik Streed's thesis [70]. The art of creating BEC is well documented in places too numerous to cite, so the aim of this chapter is to give a quick summary off the apparatus for reference in the rest of this thesis. I will discuss the creation of BEC as well as delivery to the science chamber, glossing over many of the technical details which can be found in Erik's exhaustive work. A cartoon of the machine is shown in Fig. 2-1.

A hot beam of rubidium atoms streams out of an effusive oven. The atoms are first cooled in a Zeeman slower, then captured and further cooled in a magneto-optical trap (MOT). The MOT beams are turned off, and the cloud is then transferred to a Ioffe-Pritchard magnetic trap. Radiofrequency (RF) evaporation then cools the atomic cloud to BEC.

2.1 The Oven

A flexible bellows containing up to 5 g of rubidium metal is heated to ∼110 C under vacuum to produce the alkali vapor. Hot rubidium atoms leave the oven nozzle at ∼300 m/s in a stream directed at the main chamber. Excess rubidium flux is

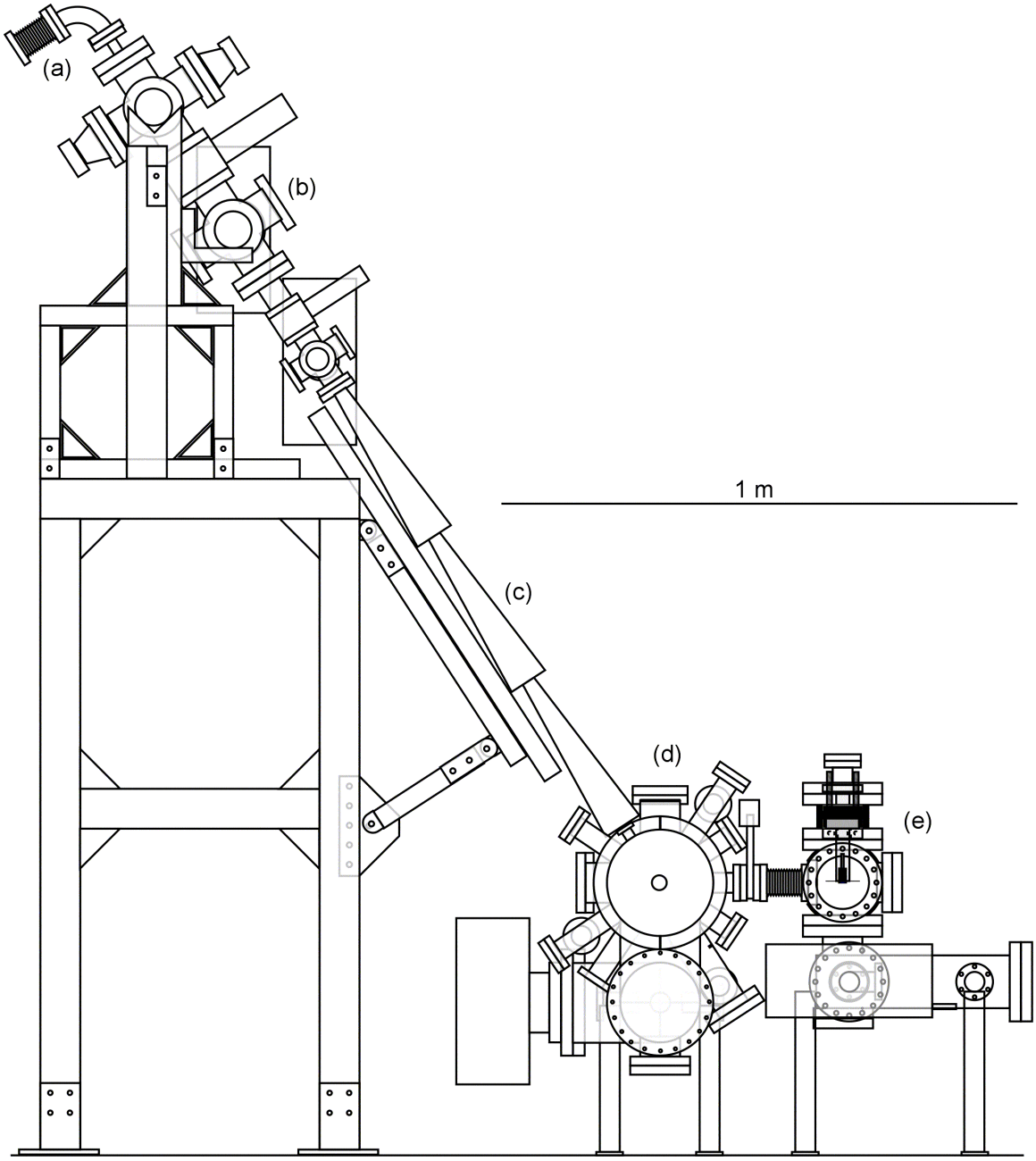

Figure 2-1: Machine overview. A) Oven. B) Beam shutter. C) Zeeman slower. D) Main chamber. E) Science chamber. The left / right axis is the "tweezer" or "transport" axis, and in and out of the page is referred to as the "pennywindow" axis.

captured with a "cold cup" that encompasses 2π sr of the oven nozzle effusive cone. Maintaining a cold cup temperature of -20 C prevents rubidium contamination of the rest of the oven chamber, and a 5 mm hole in the center of the cup allows a collimated beam of approximately 10^{11} atoms/s to continue downstream. Each 5 g ampoule of rubidium lasts 6-8 months (depending on the duty cycle), and adding more takes about a day, but can take significantly longer depending on experimental skill. The cold cup must be removed and carefully cleaned after every second rubidium change to prevent clogging.

While the melting temperature of rubidium metal is listed as 39 C [69], in normal laboratory conditions rubidium is a flaming liquid. Moisture in the air reacts with the metal in an exothermic process melting it while releasing flammable hydrogen. If rubidium metal in an enclosed space comes into contact with water, the result will be a violent explosion. In order to dispose of rubidium safely, it must *never* be put into a container (such as a beaker) until *completely* neutralized with methanol. I write this in the hope that my words may save some future rubidium lab member from losing facial hair, or worse.

2.2 The Zeeman Slower

Atoms leaving the oven scatter photons from a counter-propagating laser beam, and are thus slowed as they make their way to the main chamber. This section discusses first the theory behind Zeeman slowing, then practical design constraints for our machine, then the design, winding and performance of the slower.

2.2.1 Slowing Theory

Each photon delivers a momentum kick $p = \hbar k$ to the atom, so resonant scattering at a rate of $\Gamma/2$ will impart a maximum acceleration of $a = \Gamma\hbar k/2m$ to the atom, where k is the wavenumber of the photon, and the excited state lifetime $\tau = 1/\Gamma$, assuming a fully saturated transition. As the velocity of the atom changes, it will be doppler shifted out of resonance with the slowing laser beam. In fact, in only a

few hundred photon scatterings, the atom will be completely out of resonance with the slowing laser. While it is possible to change (chirp) the laser frequency to stay in resonance with small groups of atoms as they are slowed [18], a more efficient solution is to use magnetic fields to tune the atomic levels back into resonance via the Zeeman shift [57].

The magnitude of the magnetic field as a function of position then can be expressed as

$$B(x) = B_0 - \frac{1}{\mu_B \lambda}\sqrt{v_0^2 - \frac{f\Gamma\hbar k x}{m}} \tag{2.1}$$

Where B_0 is a bias magnetic field, μ_B is the Bohr magneton, λ is the wavelength of the slowing laser, v_0 is the velocity of the atom as it exits the oven, m is the atomic mass, and f is a safety factor to account for finite laser power and magnetic field imperfections. If f is set too close to 1.0, small errors in design or construction of the Zeeman slower can result in slowed atom flux reduction by an order of magnitude or more; our design used $f = 0.6$.

2.2.2 Design Considerations

Given the design parameters of our oven, with $v_0 = 350$ m/s, and the properties of ^{87}Rb, with $\lambda = 780$ nm, and $\Gamma = 2\pi \times 6$ MHz for the linewidth, the resulting Zeeman slower is $\sim$1 m long with a magnetic field change of $\Delta B = 320$ Gauss. We chose a large $B_0 \approx 500$ Gauss to maintain a large Zeeman splitting, preserve the polarization, and prevent unwanted hyperfine state mixing. An additional laser beam resonant with the $F = 1 \rightarrow F' = 1$ transition repumps atoms into the $F = 2$ state. It is also desirable to choose a sufficiently large bias field to prevent absorption of the slowing beam by atoms that have already exited the Zeeman slower.

The slowing laser beam is σ^- polarized and resonant on the $5^2S_{1/2}|2,-2\rangle \rightarrow 5^2P_{3/2}|3,-3\rangle$ transition ($|F, m_F\rangle$). This polarization on the cycling transition keeps atoms in a "stretched" state where decay into off-resonant states is unlikely. During the process of slowing, each atom will scatter $N \approx 60{,}000$ photons into a dipole pattern symmetric about the axis of travel. This results in a mean random, transverse

velocity of about $\hbar k\sqrt{N/3}/m_{Rb} \approx 1$ m/s as atoms exit the slower. If the exit velocity is 20 m/s, this corresponds to a 6 degree cone within which 2/3 of the atoms will fall. The exit of the Zeeman slower must be close enough to the MOT so that most of the slowed atoms will be captured.

The design of the magnetic solenoids also presents a challenge. The high field section of the slower must be near the exit, but the magnetic field must drop off rapidly so as to not significantly effect the MOT. This demands coils with high current, but small diameter. However, the low field section must maintain a good field shape at very small magnetic fields, demanding low current and large diameter. Finally, cooling water must be able to enter and exit the solenoid structure at finite intervals, perhaps necessitating multiple solenoid segments.

The ideal solution would be a series of single loops (hundreds of them), each provided the ideal current by its own power supply. However, this solution grossly violates funding constraints and invites mockery. The design finally chosen consisted of three solenoid segments, each with up to 10 concentric solenoids, and one power supply per segment.

2.2.3 The Slower Design Program

Traditionally, Zeeman slowers have been designed by hand. Each solenoid section is modeled in a computer program, such as Mathematica, and the parameters of each are modified by the experimentalist in an effort to converge to a viable solution. My solution was to design a computer program which calculated the parameters governing all possible ($\sim$30) solenoids. The fitting method was governed by only a few hand-controlled parameters, greatly reducing the parameter space and the final design time. A copy of this program has been provided in Appendix A. It should compile in any ANSI C environment, and can be copied and pasted from the electronic version of this thesis.

The output of the program is a simple drawing which represents a cross section of the idea solenoid structure. This reduces guesswork and errors during the winding

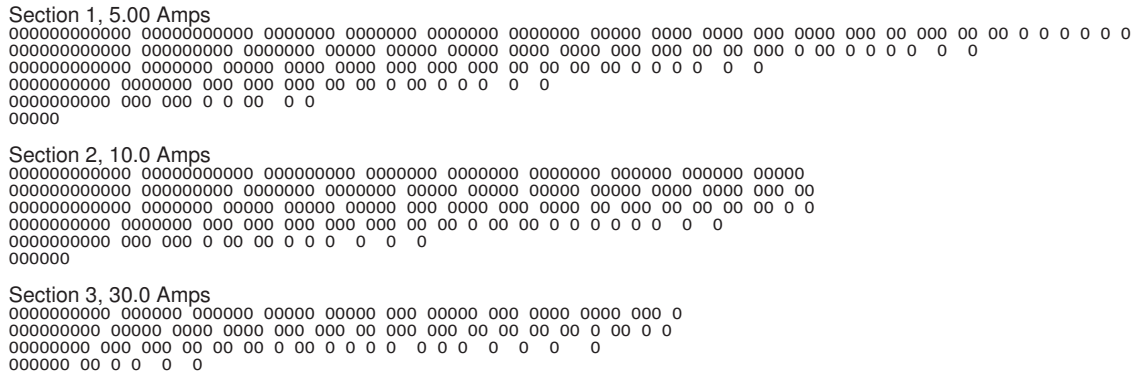

Figure 2-2: Zeeman slower winding diagram. This figure shows the output of the Zeeman slower program, which represents cross sections of the three solenoid segments. The circles represent cross sections of individual wires. Spaces in between wires are used to guide the winding process to lower the current density in some sections.

process, and provides a much finer control of the magnetic field shape with variable loop spacing - effectively each solenoid has a current density which may vary with the axial position.

2.2.4 Construction

The solenoids were wound with square, hollow core, glass insulated copper tubing, and glued in place with high temperature epoxy [70]. The wire had an overall cross section of 3.2 mm, but including insulation when wound provided a coil spacing of 3.5 mm. The hollow core was 1.6 mm square, and high pressure water at 220 psi provided cooling. The water flow Q through a straight tube is given by

$$Q = \alpha\sqrt{P/L} \tag{2.2}$$

where P is the pressure, L is the length of the tube, and $\alpha = 124$ m^2/kg$^{1/2}$ was experimentally measured. Assuming that the water temperature must increase no more than 25 C before it exits the tube, the minimum water flow through an energized solenoid must be

$$Q_{min} = \beta I^2 L \tag{2.3}$$

where I is the electrical current in the wire and $\beta = 1.5 \times 10^{-3}$. Thus the maximum lengths of any unbroken wire in the Zeeman slower is then given by

$$L_{max} = \left[\left(\frac{\alpha}{\beta} \right)^2 \frac{P}{I^4} \right]^{1/3} \tag{2.4}$$

Breaks in the winding pattern were designed to not exceed this value.

Each of the three coils was wound around a 1 inch diameter brass tube, then slid over a 0.75 inch diameter vacuum tube. This vacuum tube attaches to the main system at each end with 1.3-inch diameter flanges. This would ordinarily prevent sliding the slower coils over the vacuum tube, but one of the flanges was rotatable, and the retaining ring was cut in half. The retaining ring was then installed after solenoid assembly.

2.2.5 Performance

The magnetic field profile of the Zeeman slower is shown in Fig. 2-3. The desired field calculated from equation 2.1, the modeled solenoid field from the computer design program, and the measured field are shown as a function of distance from the MOT. The functionality of the slower was measured with an absorption spectrum as shown in Fig. 2-4, indicating that there was no significant loss of any velocity groups below the calculated capture velocity (350 m/s). Limited only by the oven efficiency and laser power, we have achieved slowed atom fluxes as high as 10^{11} atoms / s.

2.2.6 The Field Subtraction Slower

When designing an increasing field slower with solenoids, it is difficult to match the field shapes due to the sign of the curvature. One possible solution is to invert this curvature with a "field subtraction" slower. A single, inner solenoid with a small diameter provides a large bias field, and additional concentric solenoids of larger radii with current flow *in the opposite direction* remove portions of the bias field to create the correct field shape. The result is a single solenoid cone that appears to be

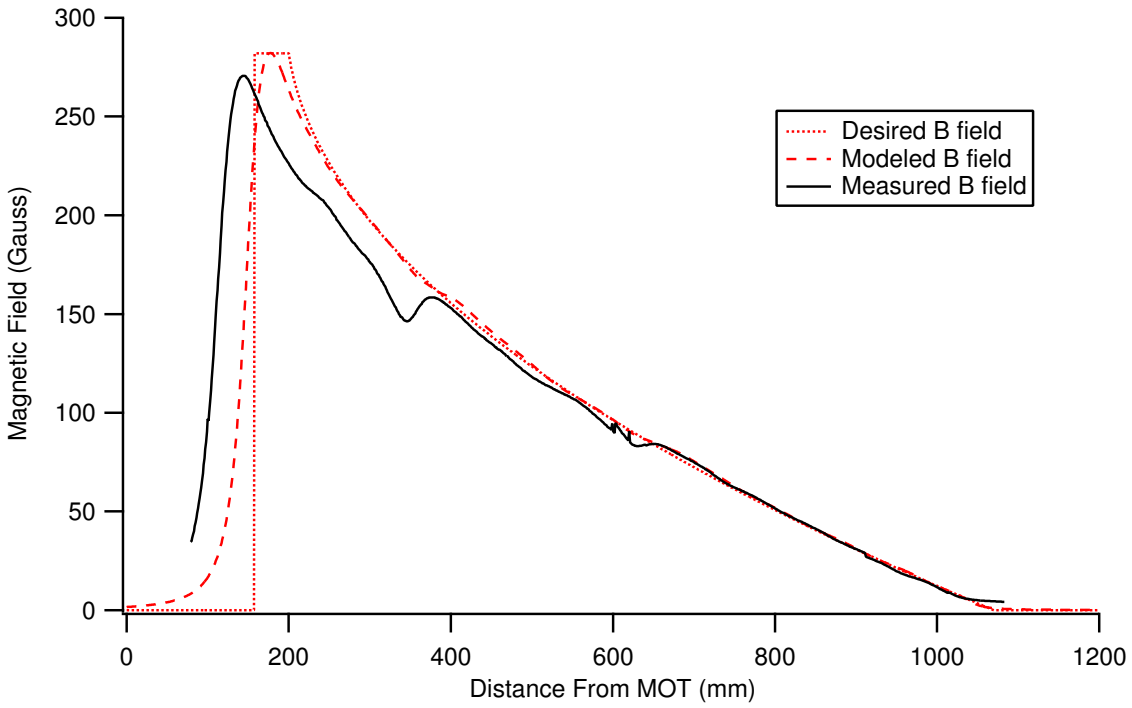

Figure 2-3: Zeeman slower field profile. The dotted line is the theoretically desired field, the dashed line is the computer generated model field, and the solid line is the measured field after construction. The dips in the field profile are a result of finite solenoid spacing for wire insertion, and were largely corrected with additional small solenoids. This profile does not include an additional ∼200 G bias field.

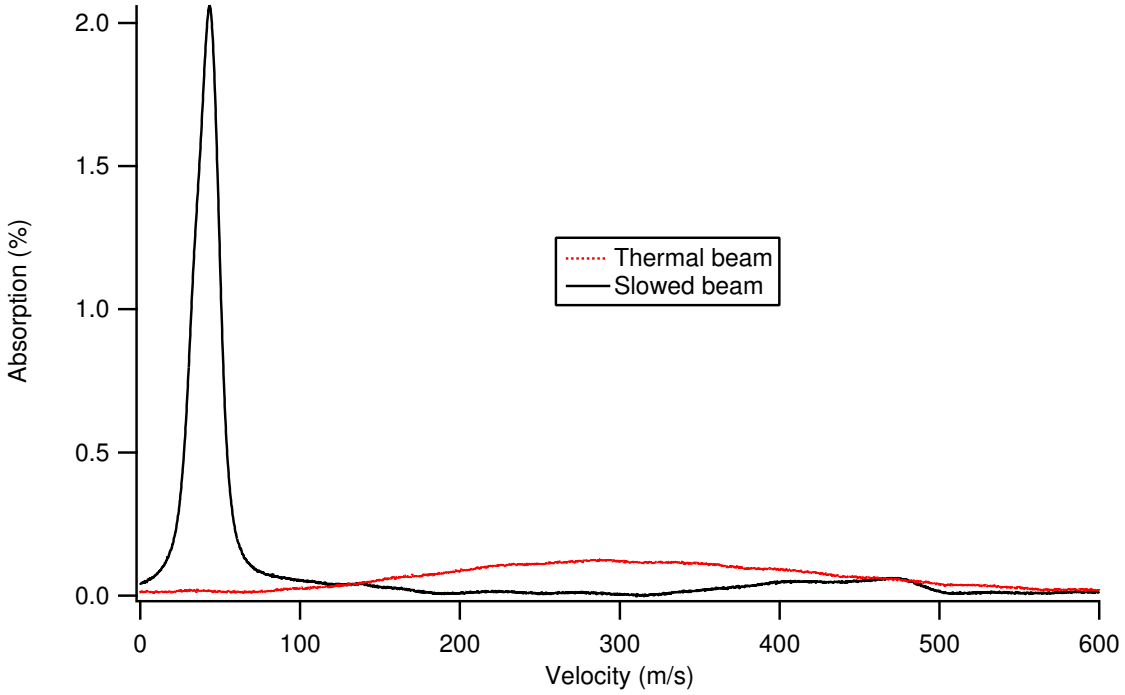

Figure 2-4: Atomic velocity profile. The absorption of the atomic beam at a 45 degree angle is shown as a function of the velocity. The red, dotted line shoes the velocity distribution of the atoms as they leave the oven, and the solid line shows a peak in the velocity distribution from atoms cooled in the Zeeman slower.

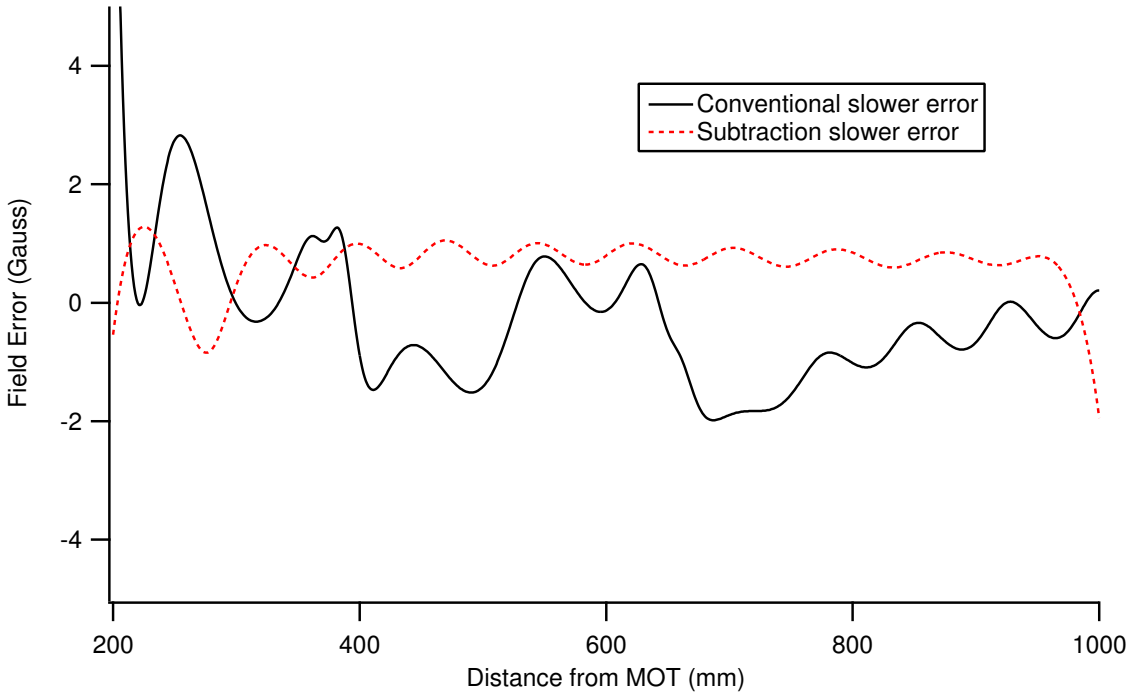

Figure 2-5: Zeeman slower error analysis. The difference between the modeled field and the desired field is plotted as a function of distance from the MOT, showing that deviations from ideal are small compared to the linewidth of the slowing transition ($\Gamma = 4.2$ Gauss). The field subtraction slower design (dotted line) theoretically reduces field deviations by an average of $\sim$2.

backwards. The narrowest section is closest to the MOT, but produces the largest field.

While not used on this machine, this design method provides several advantages. First, at the exit off the slower, the solenoid is as small as possible, greatly reducing stray fields which affect the MOT. Second, the use of only a single section removes discontinuities from the need to break out wires for cooling. Finally, the minimization of magnetic field errors ensures more robust performance. The main disadvantage is that this design method uses much more ($\sim 4\times$) power, and thus may be difficult to cool effectively. The calculated field error for the two different design methods is shown in Fig. 2-5, indicating a $2\times$ reduction in the deviation from ideal. The result is that the Zeeman slower may be designed with a safety factor f closer to 1.0, shortening the physical length and increasing the atom flux.

2.3 The Main Chamber

The main trapping chamber of the rubidium machine is based on the design for a sodium BEC machine, originally designed by Todd Gustavson. I modified Todd's design to include a few more features, including a never-used cold plate for catching unslowed rubidium atoms, and both designs are discussed thoroughly in other publications [41, 71, 70]. The design uses recessed or "bucket" flanges which place the magnetic trap as close to the atoms as possible. The magnetic trap may then be replaced without compromising the vacuum. Six optical axes intersect in the center of the chamber, and the complexity of the vacuum flange geometry prevents ideal optical access for some experiments.

2.3.1 The Magneto-Optical Trap

Upon arrival in the main chamber, atoms are trapped in a potential created by the combination of radiation pressure from three laser beams and the interaction of the atoms' magnetic dipole and a magnetic field minimum. Two electromagnets in an anti-Helmholts configuration create the magnetic field minimum, and laser beams counter-propagating on three orthogonal axes cool the resulting atomic cloud. The MOT operates with a field gradient of 16.5 G/cm, and a peak laser intensity of 5 mW/cm^2 at a detuning of -18 MHz from the $5^2S_{1/2}|2,2\rangle \rightarrow 5^2P_{3/2}|3,3\rangle$ transition. When operating the oven at 110 C, it takes approximately 10 s to load the MOT. Once full, the MOT is compressed by increasing the current in a coils by a factor of four in 200 ms, then the atoms are released by switching off the current. After release from the MOT, the laser detuning is increased and the power decreased to further cool the atoms for 7 ms in an optical molasses. A 3 ms pulse of "depumping" light transfers the atoms from the $F = 2, m_F = -2$ state to the $F = 1, m_F = -1$ state.

2.3.2 The Magnetic Trap

Immediately after depumping, the Ioffe-Pritchard magnetic trap is switched on. This trap is also described in [41, 71, 70], and produces a magnetic field theoretically

described by

$$\mathbf{B} = B_0 \begin{pmatrix} 0 \\ 0 \\ 1 \end{pmatrix} + B' \begin{pmatrix} x \\ -y \\ 0 \end{pmatrix} + \frac{B''}{2} \begin{pmatrix} -xz \\ -yz \\ z^2 - \frac{1}{2}(x^2 + y^2) \end{pmatrix} \tag{2.5}$$

In the axial (pennywindow) direction, trapping is provided by the field curvature term, and the radial trapping is analogous to a quadrupole field zero with an additional bias field. The B_0 term prevents Majorana spin flips by removing the magnetic field zero.

2.3.3 Construction

The magnetic trap was wound with the same wire as the Zeeman slower, and cast with the same high temperature epoxy. A photograph of the magnetic trap just prior to installation is shown in Fig. 2-6. Water is forced through the coils at 230 PSI to provide up to 10 kW of cooling when up to 500 Amps are driven through the coils. Flow switches (McMillan model 501) monitor the cooling water flow through every coil, and in the rare event that they are all simultaneously functional they may be linked to the electrical interlock safety system.

2.4 Evaporation

After transfer to the magnetic trap, RF radiation is introduced which drives a transition from the trapped $|1, -1\rangle$ state to the untrapped $|1, 0\rangle$ and $|1, 1\rangle$ states. Sweeping the frequency from high ($f \gg \mu_B B_0$) to low ($f \approx \mu_B B_0$) evaporates the hottest atoms from the trap in a process that cools the remaining atoms. Evaporative cooling is well documented in the literature [29, 13, 56], and cooling the atomic cloud to BEC in our magnetic trap takes about one minute.

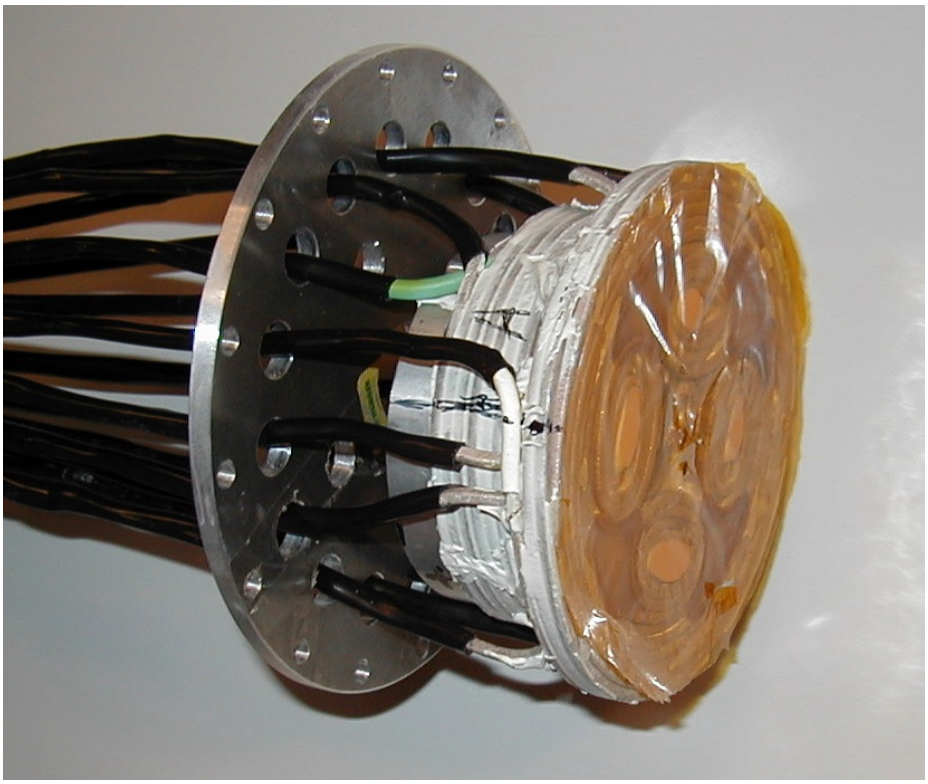

Figure 2-6: Photo of the magnetic trap. Just prior to installation on the machine, the magnetic trap coils are covered in high temperature epoxy and further insulated with Kapton film. These two protections have prevented any electrical shorts in five years of operation.

2.4.1 GPIB Control

The RF signal is generated by an Agilent 33250a synthesizer, which is computer controlled over a general purpose instruments bus (GPIB) link. The frequency can be updated every 30 ms, or the frequency and power can be updated together every 90 ms. This method provides an advantage over voltage controlled oscillators (VCOs) because it combines a large sweep range (80 MHz) with extremely precise frequency control ($\sim$ 1 mHz). However, some experimental procedures, such as rapid sweeps, cannot be generated by this method and additional synthesizers must be used.

2.5 Imaging

All experiments in this thesis detected the atom clouds with resonant absorption imaging. The ^{87}Rb D_2 line has wavelength $\lambda = 780.241$ nm and a linewidth of $2\pi \times 6.07$ MHz. Atomic clouds in the $F = 2$ state were imaged on the $F = 2 \rightarrow F' = 3$ transition, and clouds in the $F = 1$ state were first optically pumped into the $F = 2$ state along a different axis before and during imaging. Mixtures of $F = 1$ and $F = 2$ could be separately resolved by first imaging the $F = 2$ atoms, then adding the repumping light to image the $F = 1$ atoms. The duration of the imaging light pulse was kept short to minimize atomic motion during the image, with typical durations of 50 - 100 μs.

The imaging light was collected on a Princeton Instruments NTE/CCD-1024-EB camera with a square pixel size of 13 μm. Three frames were taken for each image; first a probe with atoms (PWA) frame to detect the atoms, then a probe without atoms (PWOA) frame to determine the reference laser intensity, then a dark field (DF) frame without laser illumination to determine the background noise. The final absorption image (ABS) was then determined by

$$\mathsf{ABS} = \frac{\mathsf{PWA} - \mathsf{DF}}{\mathsf{PWOA} - \mathsf{DF}}. \tag{2.6}$$

Pixels that image no atoms have a value of around 1.0, corresponding to no absorption,

and pixels that image an optically dense column of atoms have values that may approach zero. The number of atoms, N, in the absorption image can be calculated by

$$N = -\frac{A}{\sigma_0} \sum_{x,y} \ln \mathsf{ABS} \tag{2.7}$$

where A is the area imaged per pixel, and σ_0 is the resonant scattering cross section, but these prefactors are usually omitted when making plots of relative atom number.

2.5.1 Time-of-Flight

While held in the the magnetic trap, the BEC is typically quite small, with a typical width and length of 10 and 100 μm. Considering that our imaging optics operate at about $f_{\#} \approx 5$, features of the BEC are barely resolved when imaged in-trap. The solution is to suddenly release the BEC from the trap, and the chemical potential of the cloud causes it to expand ballistically in a time-of-flight (TOF). The result is that TOF images show the *momentum* distribution of the condensate after the mean field energy is converted into kinetic energy. More detailed analysis of atomic cloud imaging techniques can be found in [37, 47, 68].

2.5.2 Light Creation

Laser light for slowing, cooling, and imaging is produced by diode lasers on a separate optical table with diode lasers and delivered via optical fibers. Fiber coupling eliminates the need to account for changes in the relative position of the two tables and reduces maintenance time. Light for cooling and imaging on the $F = 2 \rightarrow F' = 3$ cycling transition is produced by a grating stabilized diode laser and tapered amplifier (Toptica TA-100), repumping light on the $F = 1 \rightarrow F' = 1$ transition is created by another grating stabilized diode laser (Toptica DL-100), and both frequencies of slowing light are generated by injection locked diode lasers. Frequency locking for both the cycling and repumping light is maintained by polarization sensitive saturated absorption spectroscopy [52, 81]. Laser beam intensities are controlled with microsecond accuracy using acousto-optic modulators (AOMs). Further details about the optical

setup can be found in Ref. [70].

2.6 Transport

Since the main chamber is crowded with optics, magnets, and various other bulky and sensitive equipment required to create BEC, there is little room for additional apparatus or even optical access. In order to more closely interact with the condensate, we transport the atomic cloud into a separate "science chamber" which may be changed entirely to more efficiently suit the needs of any particular experiment. In order to deliver the atoms to the science chamber, an optical tweezer is used to trap and then transport the cloud.

2.6.1 Optical Potentials

Optical forces may be used to confine atoms in situations where magnetic trapping is unsuitable. Strong field seeking hyperfine states, as well as magnetically sensitive mixtures of hyperfine states may be trapped in optical potentials. The optical dipole potential is given by [2, 9]

$$V_{optical} = \frac{1}{2}\hbar\Delta \ln\left(1 + \frac{I(\vec{r})}{I_{sat}}\frac{(\Gamma/2)^2}{\Delta^2 + (\Gamma/2)^2}\right) \tag{2.8}$$

Where $I(\vec{r})$ and ω are the intensity and frequency of the optical field, $\Delta = \omega - \omega_0$ is the detuning from resonance, I_{sat} is the saturation intensity, and Γ is the width of the transition. Thus atoms may be trapped in the local maxima of red-detuned beams, and in the minima of blue-detuned beams. Neglecting the counter-rotating term in the rotating wave approximation, this potential may be closely approximated by

$$V_{optical}(\vec{r}) = \frac{3\pi c^2}{2\omega_0^3}\frac{\Gamma}{\Delta}I(\vec{r}), \tag{2.9}$$

and the spontaneous photon scattering rate is

$$\Gamma_{spont}(\vec{r}) = \frac{3\pi c^2}{2\hbar\omega_0^3}\frac{\Gamma^2}{\Delta^2}I(\vec{r}). \tag{2.10}$$

Thus by choosing a large enough detuning and providing enough optical power, optical trapping can be used to hold the atoms with negligible heating.

2.6.2 Experimental Setup

A cartoon depicting the optics and mechanics used in the transport process is shown in Fig. 2-7. A collimated beam with $1/e^2 = 40$ mm radius is focused onto the atoms with a $f = 450$ mm lens. An air bearing translation stage (Aerotech ABL2075) controls the axial position of the focussing lens to sub-micron accuracy, and a computer program controls the path of motion. Up to 800 mW of light was used to trap the atoms in order to provide the necessary axial trapping for transport in a reasonable (3 s) time.

2.6.3 Motion Algorithm

The motion of the translation stage was controlled by specifying the transport time t, the distance x, and the maximum acceleration ($a_{max} = \delta x^2/\delta t^2$). A computer program then numerically determined a fixed value for the jerk ($j = \delta x^3/\delta t^3$) which described the desired motion. Typical values were $t = 2$ s and $x = 360$ mm, stipulating $j = 1430$ mm/s^3. The motion was divided into a series of reference points with $\delta t = 4$ ms for computer interpolation of the motion.

2.7 The Science Chamber

The science chamber enabled us to perform several different types of experiments without compromising UHV in the main chamber. Venting the main chamber is considered a magnitude 1.0 disaster in our group, and can take many weeks to recover in a process usually requiring removal of the magnetic trap, MOT optics, and myriad miscellaneous apparatus, coupled with a high temperature (250 C) bakeout which

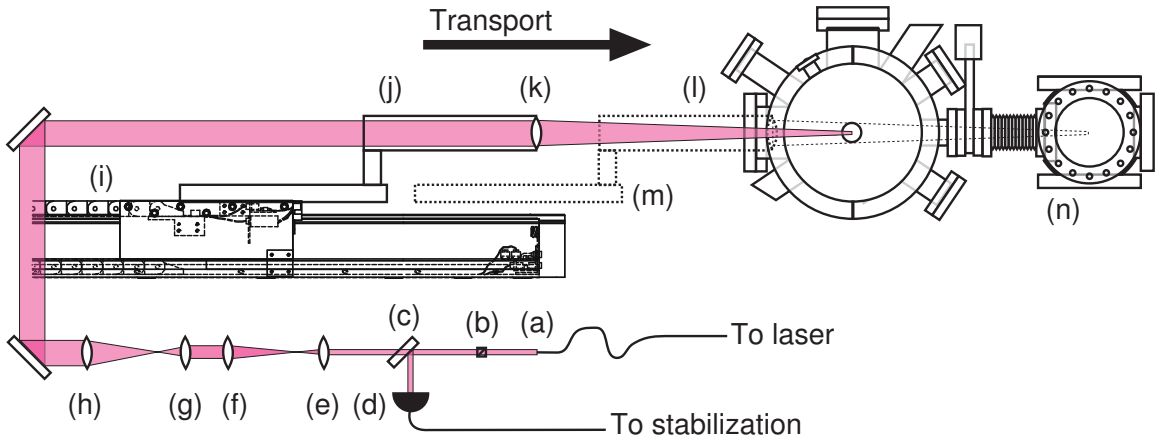

Figure 2-7: Optical transport cartoon. Laser light with $\lambda = 1064$ nm exits the optical fiber (a), then passes through a polarizing beam splitting cube (b) to clean the polarization. A glass wedge (c) picks off a small portion of the light for measurement on a photodiode (d) to stabilize the intensity. Four lenses with focal lengths 35 mm (e), 150 mm (f), 35 mm (g), and 150 mm (h) form two telescopes to expand the collimated beam to a radius of $1/e^2 = 40$ mm before reaching the translation stage (i). A lead filled extension arm and 2 inch diameter lens tube (j) hold a final $f = 450$ mm lens that focuses the beam onto the atomic cloud in the main chamber (l). The translation stage moves the lens holder to the delivery position (m), translating the focus and the atoms 360 mm into the science chamber (n).

may cause leaks. The removal and replacement of the science chamber has been accomplished several times in my time in the lab, allowing experiments to be started in a very short time, where in other laboratories such endeavors may require the complete construction of a dedicated apparatus.

2.7.1 Vacuum Preparation

Before installation on the machine table, each science chamber is usually "pre-baked" at a high temperature (again, 250 C) to reach pressures of $< 10^{-9}$ Torr with a combination of turbo and ion pumps. After a brief venting with argon or nitrogen, the science chamber can be attached to the main chamber and baked again for a much shorter time, typically three or four days. Final bakeouts with temperatures as low at 70 C were even achieved, eventually reaching 10^{-11} Torr with titanium sublimation.

2.7.2 Technical Drawings

Two different science chamber designs are depicted in Appendix E, but the less interesting pump bodies are not shown. One design is for the hard disk platter experiment, which is discussed in Chapter 4. The other design is for a future experiment with optical lattices. This chamber affords greatly increased optical access to the atoms, and should provide for much more mechanically stable beam paths. It is likely that the next work to be done in the rubidium lab after I leave will be done in this chamber, and I entrust it to the care of my labmates.

2.8 Conclusion

Already in its fifth year of operation, the rubidium machine has proven robust and reliable. It has survived explosive venting, magnetic trap partial meltdowns, and other, unspeakable abuses, yet it produces atom clouds with temperatures in the nK regime with better than 5% number stability and makes measurements more accurate than a part in 10^9. I am sure that the students who follow me will push it to even

greater achievements.

Chapter 3

RF Dressing Of a Magnetic Potential

This chapter describes the use of an RF field to manipulate the effective trapping potential in an otherwise static spherical quadrupole magnetic field. The goal was to create a very oblate "pancake" BEC with very low trap frequencies in two directions, and a very high trap frequency in the third for studying BEC in 2D. However, calculations showed that the maximum attainable tight trap frequency, limited by Majorana flops, increases smaller than $\sqrt{B'}$, which limits its usefulness for studying 2D systems. Transfer of BECs into the dressed Zeeman trap with ∼100% efficiency was accomplished using a specialized arbitrary function generator to provide the cleanest possible RF signal. While this experiment did not result in a published work, a summary of the results are provided for others who may wish to investigate this in the future.

3.1 The Dressed Zeeman Trap Overview

First proposed in [83] and demonstrated in [10] and [79], the dressed Zeeman trap, or "eggshell" trap confines atoms to the surface of a sphere centered around a magnetic quandupole minimum. The frequency of the RF and the magnitude of the magnetic field gradient, B', determine the radius of the sphere, and the intensity of the RF

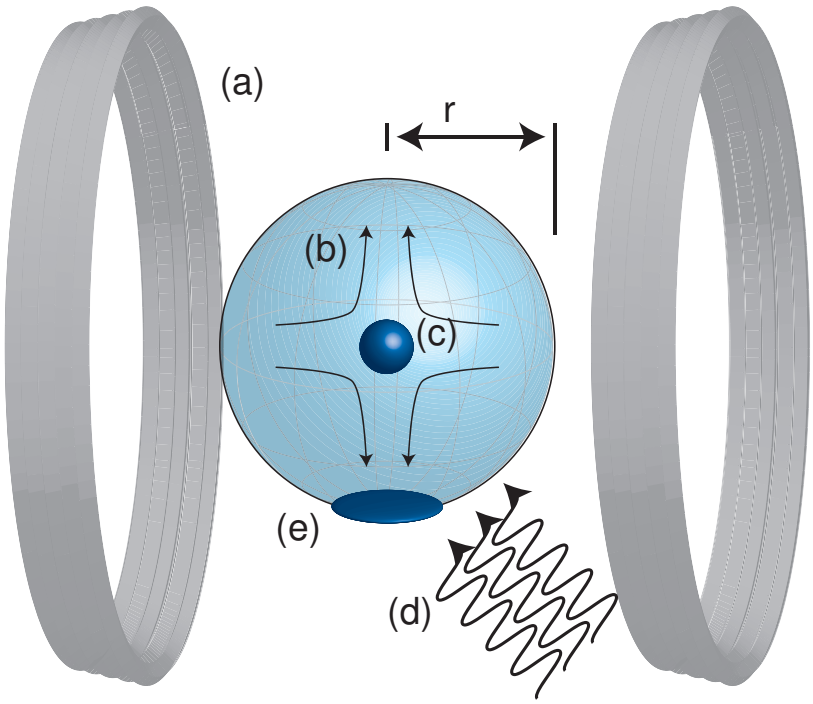

Figure 3-1: Cartoon of the dressed Zeeman trap. Magnetic coils (a) produce a gradient of B (b) that normally traps atoms at point (c). An RF field (d) is applied which dresses the atoms, which are then trapped on a sphere of iso-B (e) of radius r. Gravity pulls the atoms toward the bottom of the sphere.

radiation determines its thickness. For non-symmetric magnetic fields (such as our Iofffe-Pritchard trap), the RF frequency maps a surface of iso-B which defines where the atoms are trapped. Gravity causes the atoms to live at the bottom of this potential, so the atoms are weakly but harmonically trapped in the horizontal directions like a pendulum. Counter-intuitively, reducing the strength of the RF dressing field *increases* the transverse (radial) trap frequency, but this has a severe limitation. If the power is reduced too much, the atoms will quickly undergo Majorana flops at the avoided crossing and will be lost from the trap.

3.1.1 Adiabatic Potentials

In this experiment, an adiabatic potential is created by the interaction of a two-state atomic system in the a magnetic gradient and a RF field. Diagonalizing the Hamiltonian of a two level system in the presence of the coupling field results in a

"dressed state" picture where the two states are subject to an adiabatic potential [75], on which the moving atoms will stay on as long as the coupling field is strong enough to prevent Landau-Zener transitions. For instance, our RF evaporation creates an adiabatic crossing where the RF field is on resonance with the $|1,-1\rangle \rightarrow |1,0\rangle$ and $|1,0\rangle \rightarrow |1,+1\rangle$ transitions. For small magnetic fields (< 10 G), these transitions are degenerate. We then can then map the $|1,-1\rangle$, $|1,0\rangle$, and $|1,+1\rangle$ states onto the dressed states ϕ_+, ϕ_0, and ϕ_-, shown as the top, middle, annd bottom curves in Fig. 3-3, respectively.

3.2 Dressed Potential Calculations

The dressed Zeeman trap is derived from first principles and discussed in great detail in [82]. In this section I will present some of the most important results from that work and discuss their relevance to the experimental process. Taking the case of an alkali atom in the $F = 1$ hyperfine state, for small magnetic field values the Zeeman energy of the magnetic sublevels is linearly dependent on B. RF radiation is introduced which resonantly couples the $|1,-1\rangle$ state to the $|1,0\rangle$ and $|1,+1\rangle$ states [Fig. 3-2]. This field dresses the original atomic states into ϕ_+ and ϕ_-, as shown in figure 3-3, with the form

$$U = mgz \pm \hbar \left[\left(\mu_B \sqrt{B_0^2 + (B'r)^2} - \Delta \right)^2 + \Omega^2 \right]^{1/2} \tag{3.1}$$

where z is the vertical component of the distance r from the magnetic field minimum, g is gravity, μ_B is the Bohr magneton, B_0 is the axial bias field in the Ioffe-Pritchard trap, Δ is the RF frequency, and Ω is the strength (Rabi frequency) of the RF dressing field.

3.2.1 Dressed States

If the RF field is initially turned on with $\Delta > \mu_B B_0$, the atoms are trapped at the center of the lower potential in figure 3-3. If Δ is then decreased, atoms with sufficient

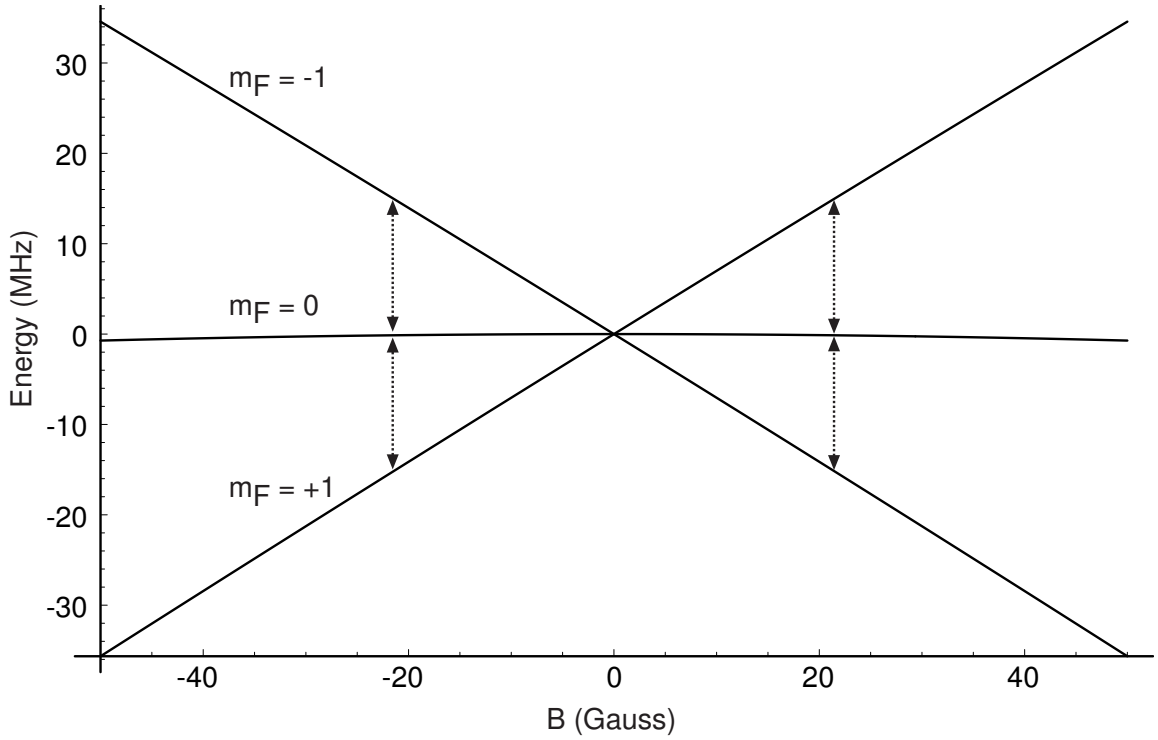

Figure 3-2: Zeeman energy of the $F = 1$ state vs. magnetic field. The solid lines depict the energy dependence of the labeled states on magnetic field, and the dotted lines indicate the RF resonance for an applied field with $\Delta = 30$ MHz.

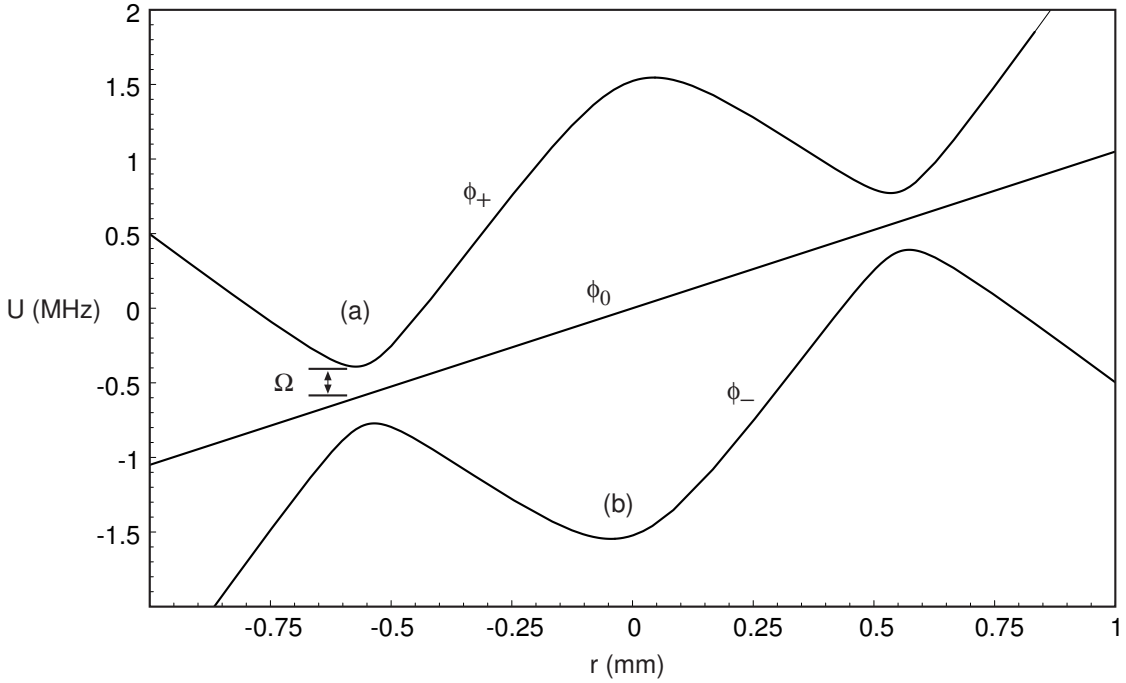

Figure 3-3: Graph of the dressed RF potential. The horizontal axis of the graph is a vertical slice upwards through the center of the trap, and the top line shows the potential for the trapped dressed state. The parameters plotted are for $B' = 50$ G/cm, Ioffe-Pritchard bias $B_{bias} = 1$ G, $\Delta = 2$ MHz, $\Omega = 200$ kHz, and including the effects of gravity. During normal RF evaporation, atoms are confined by the lower potential and trapped at point (b), and ejected from the trap when they reach point (a). In the dressed trap, the atoms are confined by the upper potential and trapped at point (b).

kinetic energy will be removed from the trap - this is exactly the process we use to evaporatively cool the atomic cloud when we create BEC. However, if the RF field is turned on at $\Delta < \mu_B B_0$ and increased to the value greater than $mu_B B_0$, then the atoms will be confined to the upper potential of figure 3-3 and trapped at point (a).

If the field is a symmetric quadrupole, in three dimensions the atoms will be trapped on the surface of a sphere with radius

$$r = \frac{\Delta \mu_B}{B'}. \tag{3.2}$$

Due to the effects of gravity, the atoms will pool on the bottom of the sphere. The trap frequency of the potential minimum, analogous to a Ioffe-Pritchard trap with bias field $B_0 = \Omega/\mu_B$, is then given by

$$\omega_z = \frac{B'\mu_B}{2\pi}\sqrt{\frac{g_F}{\Omega m}} \tag{3.3}$$

where m is the mass and $g_F = 1.0$ (0.5) for atoms in the $m_F = \pm 2(\pm 1)$ state.

At the bottom of the sphere, atoms will be trapped horizontally by a pendulum potential with trap frequency

$$\omega_x = \sqrt{\frac{g}{r}} \tag{3.4}$$

In the case of our I-P magnetic trap, the axial trapping frequency ω_y is approximately constant because the effective radius is very large, and is determined by the axial field curvature. Instead of a sphere, the resulting equipotential contour is oblate.

3.2.2 Limit Of Tight Trapping

From equation 3.3, we see that decreasing the strength of the RF dressing field Ω actually *increases* the trap frequency. However, Ω cannot be reduced to an arbitrarily small value, as Landau-Zener spin flip losses through the avoided crossing will increase with diminishing Ω. From [82] we see that the loss rate γ goes as

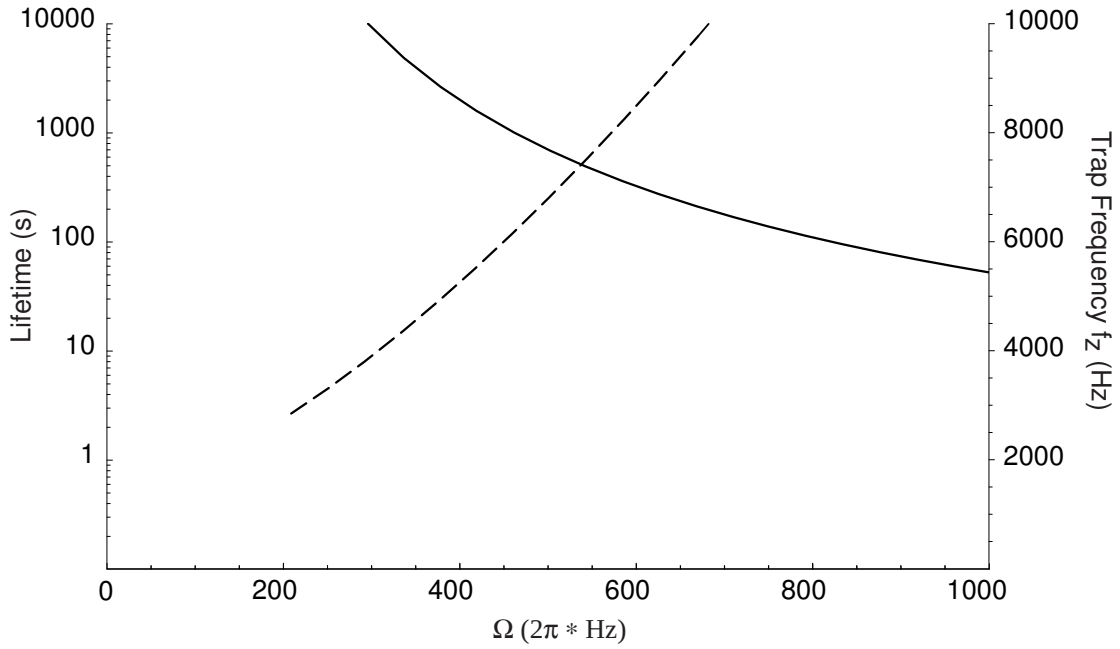

Figure 3-4: Trap frequency and lifetime vs Ω. The left axis and dashed plot indicate the theoretical lifetime vs the amplitude of the dressing field Ω. The right axis and the solid line indicate the transverse trap frequency f_z vs Ω for a fixed field gradient of 114 G/cm, 1.0 mm sphere radius, and atoms in the $|2, +2\rangle$ state.

$$\gamma \sim 2 \exp\left(\frac{-\pi\Omega^{3/2}}{\sqrt{2\Delta}}\right) \tag{3.5}$$

for $\gamma \ll 1$. Mathematically, this loss is a result of off-diagonal terms in the Hamiltonian after diagonalization into the ϕ_+ and ϕ_- states. This particular limitation is dramatically exaggerated in experimental implementations, which will be discussed later. Figure 3.2.2 shows the behavior of the lifetime $(1/\gamma)$ and the trap frequency w_z as a function of Ω.

3.3 Two Dimensional Physics

In order to get to the 2D regime, ω_z must be made large compared to both the horizontal trap frequencies and the self-energy (chemical potential, μ) of the condensate. If μ is small compared to the harmonic oscillator level spacing $\hbar\omega_z$, the vertical degree

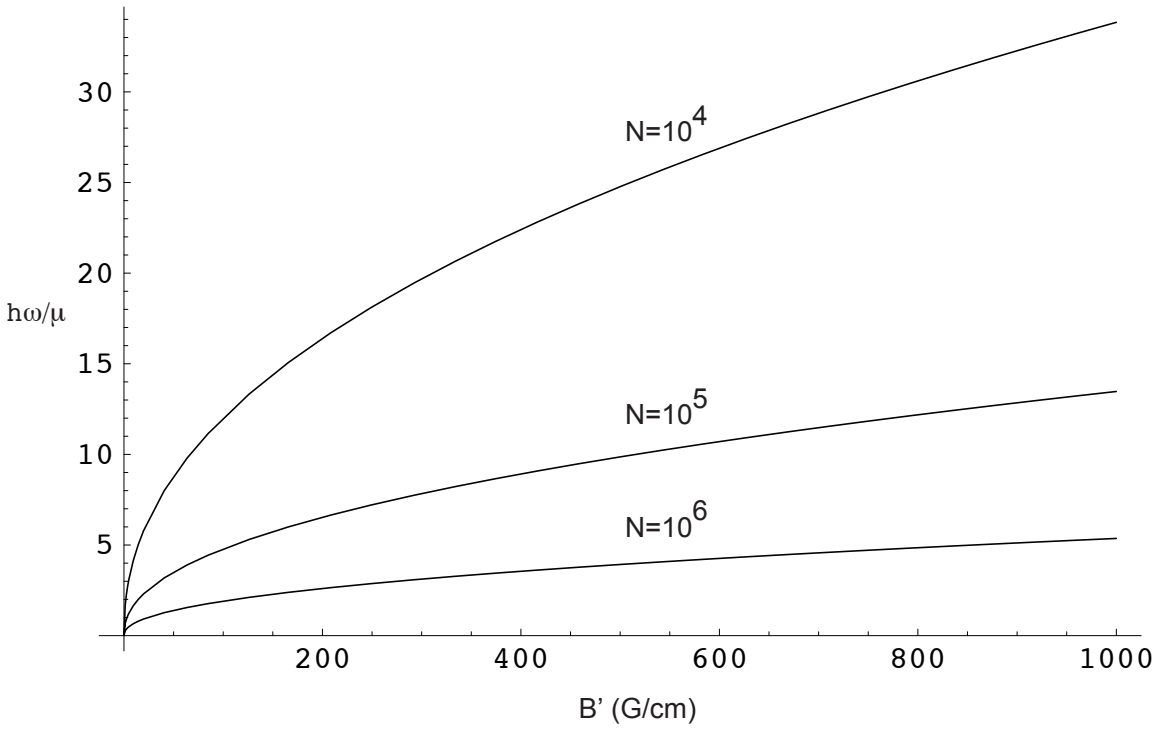

Figure 3-5: Maximum ratio of energy level spacing to chemical potential versus magnetic field gradient. The three curves are for 10,000 atoms (top), 100,000 atoms (middle), and 1,000,000 atoms (bottom), assigning a value for Δ that produces a sphere of $r = 1$ mm. For reference, our decompressed trap produces 52 G/cm and our standard compressed trap produces 114 G/cm. For this calculation, the axial trap frequency was fixed at $\omega_y = 2\pi\times$ 3 Hz.

of freedom will be "frozen out", and the system will begin to take on two-dimensional characteristics. Fig. 3-5 shows the ratio $\hbar\omega$ to μ for various atom numbers.

3.3.1 The Capabilities of the Our Apparatus

Assigning values relevant to our experiment, with $B' = 114$ G/cm, in our current main chamber we could achieve $\hbar\omega > 5\mu$ with N=100,000. That figure is certainly in the 2D regime, but it's a best case scenario. Higher magnetic field gradients, along with better imaging to more efficiently detect smaller atoms numbers could be implemented in a specially designed science chamber. This system suffers from poor scaling also, since $\hbar\omega/\mu$ scales only approximately as $\sqrt{B'}$.

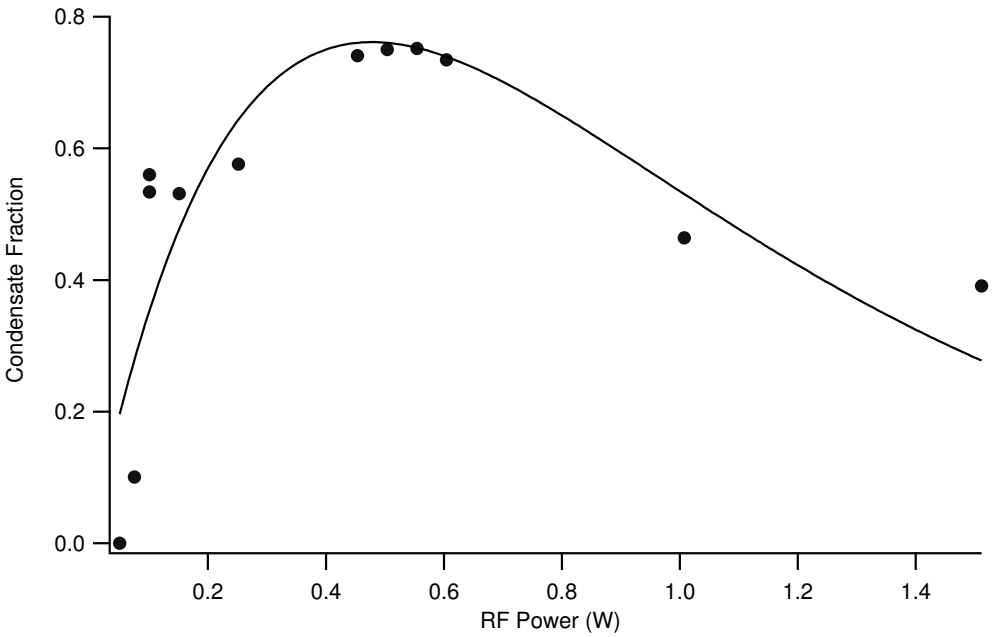

Figure 3-6: Condensate fraction vs RF power. The condensate fraction after transfer into the dressed trap was strongly dependent on Ω. The horizontal axis is the RF power measured just before the vacuum chamber. Too much or too little power resulted in heating from non-adiabatic transfer. The line is a fit to the function $axe^{-x/b}$ to guide the eye, with $a = 4.3 \pm 0.6$ and $b = 0.48 \pm 0.06$. Every change in the trap parameters or RF signal delivery required re-optimization

3.4 Experimental Procedure

3.4.1 BEC Creation and Transfer

Each BEC was created in the standard way for our machine, direct RF evaporation of the atomic cloud in the decompressed magnetic trap in the main chamber. After evaporation to BEC at 1.05 MHz, an RF field was switched on with full power at 0.90 MHz and ramped to 3.49 MHz over 600 ms at a power of 1.31 W. The frequency shape of the ramp was a half-cosine, which was important to achieve good transfer with minimal excitations. If the ramp was too fast or the derivative $\delta\Delta/\delta t$ was too high, large oscillations of the BEC were observed after the ramp. The gradient of the decompressed Iofffe-Pritchard trap B' was measured to be 53 G/cm, and the RF power was measured just before the vacuum chamber.

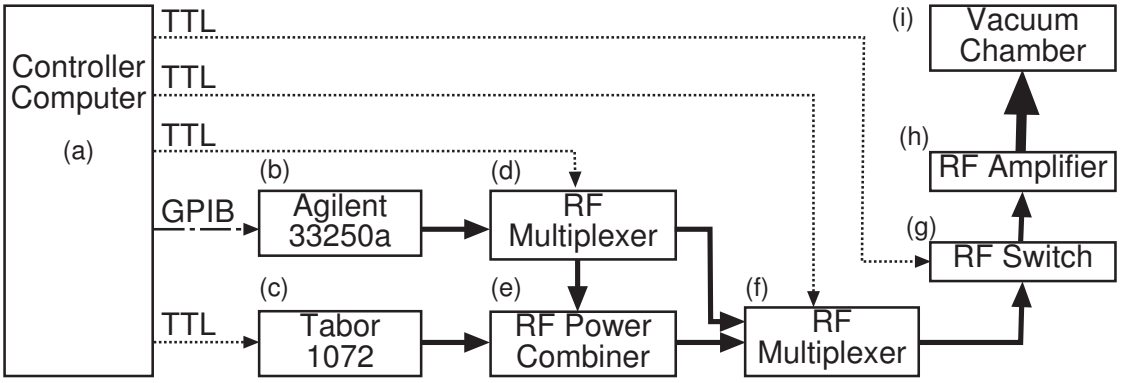

Figure 3-7: RF component setup. Dashed lines indicate TTL logic signals, and solid lines indicate RF signal. The components are as follows: a) Controller computer, b) Agilent 33250a function generator, c) Tabor 1072 DDS arbitrary function generator, d) RF multiplexer, e) RF power splitter/combiner used in the power combining direction, f) RF multiplexer (same as (d)), g) RF switch, h) RF amplifier, and finally h) the vacuum chamber. During evaporation, the RF signal was delivered in the order (b-d-f-g-h-i). During transfer into the dressed trap, the signal was delivered through (c-e-f-g-h-i), and after the sweep the signal was delivered simultaneously by both function generators ([b-d-e]+[c-e]-f-g-h-i).

3.4.2 RF Setup and Control

The setup of the RF components is depicted in figure 3-7. This system allowed for GPIB control of the RF for evaporation, preprogrammed direct digital synthesis (DDS) of the dressing field, and the implementation of an additional RF shield in the dressed state to prevent heating after transfer. The entire sweep and hold sequence was programmed into the Tabor 1072 arbitrary function generator before the experimental sequence using a computer program to generate the required waveforms. The Tabor was then triggered by a TTL signal to begin its sweep, after which the Agilent was set to 2.110 MHz to act as an RF shield and remove thermal atoms. Nearly 100% of the atomic cloud was transferred to the dressed trap in this way, with very little heating.

3.4.3 Imaging

After holding for some time in the dressed trap, the magnetic field and RF fields were switched off and the atoms were allowed to expand ballistically in time of flight

for 33 ms. After this expansion, the atomic cloud was imaged vertically on the $F = 2 \rightarrow F' = 3$ transition with repumping from $F = 1 \rightarrow F' = 2$ along a different axis. Side imaging was useful for verifying transfer into the dressed trap, and as long as Δ was not increased so much that the atoms were lowered completely out of the field of view, a calibration of r vs. Δ quickly provided a precise determination of the gradient produced by the magnetic trap.

3.5 Results

3.5.1 BEC Transfer

BECs containing up to 10^6 atoms were transferred into the dressed RF potential with near unity efficiency, and lifetimes of up to 11 s were observed. The efficiency of the transfer was strongly dependent on Ω, the shape of $\Delta(t)$, and any noise sources on the RF signal. The final value of Δ was varied over a range from 1 - 10 MHz without detriment to the atomic cloud, as long as the shape of $\Delta(t)$ at the point where $\Delta = \mu_B B_0$ was maintained. Linear ramps of Δ resulted in poor transfer and heating. Attempts to transfer atoms from the compressed trap ($B' = 114$ G/cm) were similarly unsuccessful.

3.5.2 Trap Frequencies

The horizontal trap frequencies (ω_x, ω_y) were measured to be $2\pi \times (20, 3.4)$ Hz at $\Delta = 3.49$ MHz. The vertical trap frequency ω_z was measured with parametric heating to be 250 Hz. In an attempt to measure the vertical trap frequency by observing oscillations in time of flight, the atoms in the dressed trap were "kicked" by turning on the MOT coils for 50 μs. The energy delivered by this kick was large enough to drive the atoms to the top of the RF sphere, resulting in ring like structures in TOF expansion (Fig. 3-8).

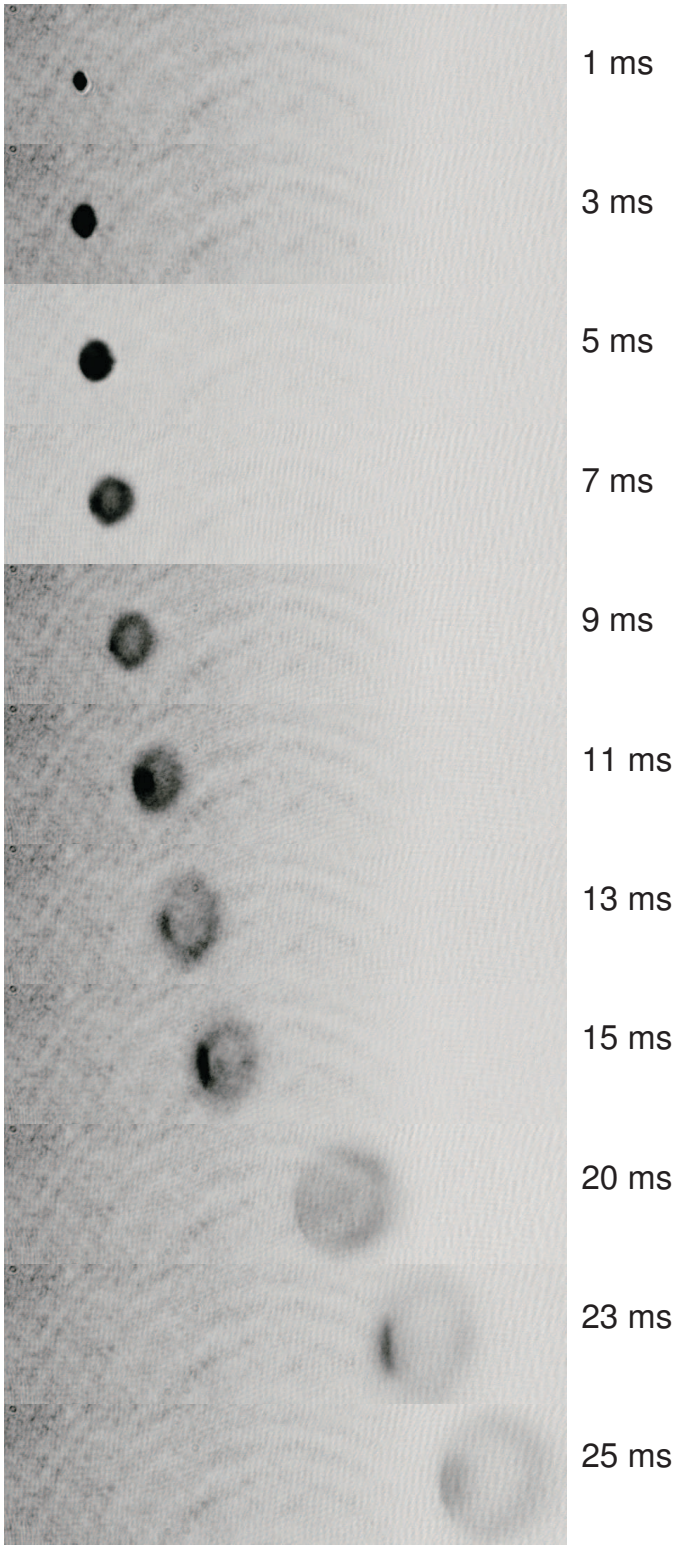

Figure 3-8: Large amplitude oscillations in the dressed Zeeman trap. A magnetic field gradient was applied for 50 μs, delivering kinetic energy to the atomic cloud. The resulting pennywindow axis images are shown here as a function of time-of-flight. Each region of interest is 4 mm $\times$ 1 mm. The densest part of the atomic cloud appears at the top of the bubble in some images because the atoms have a relatively large amount of kinetic energy.

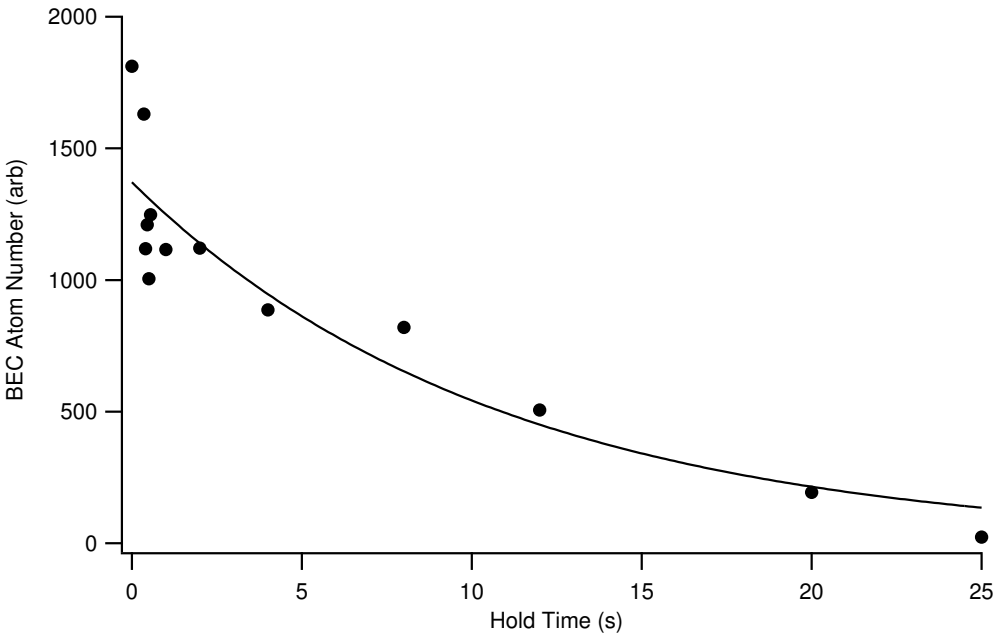

Figure 3-9: Lifetime of BEC in the dressed trap. The graph shows the number of atoms in the BEC (in arbitrary units, after subtraction of the thermal component) as a function of the hold time in the RF trap. The lifetime was determined to be 11 ± 2 s. The parameters used were $B' = 53$ G/cm and $\Delta = 2.0$ MHz.

3.5.3 Lifetime

After transfer into the dressed trap, the lifetime of the BEC was measured to be 11 ± 2 s, shown in Fig. 3-9. Further improvements in the RF control increased the lifetime to 30 s, with BEC observed as long as 60 s (Fig. 3-10).

3.6 Experimental Caveats

The dressed Zeeman trap is very fragile. Almost all of the work on this project was to determine methods to control the system without creating noise in the RF signal. Here I will explain some of the limitations of the system, and attempts we made to overcome them.

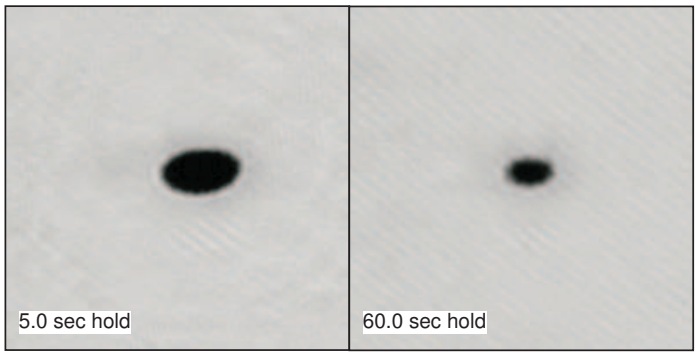

Figure 3-10: Images of BEC in the dressed trap. Top imaging in 33 ms TOF with a 1 mm region of interest shows the condensate 5.0 s and 60.0 s after transfer into the dressed trap. The RF knife prevented the buildup of any visible thermal component.

3.6.1 RF Noise

Well designed magnetic traps benefit from common mode noise rejection, where small current fluctuations in any one power supply relative to another do not usually disturb the atoms. However, this is not the case with the dressed Zeeman trap. Since the RF power Ω corresponds directly to the vertical trap frequency, and the frequency Δ controls the vertical trap position, any noise in either of these values will lead to parametric heating of the atomic cloud. Also, phase noise from signal switching (e.g. a multiplexer) may instantly project trapped atoms into the untrapped state, leading to loss of most of the atoms.

3.6.2 Analog Control

These losses and heating were observed in any attempt to control the RF signal through analog devices. For example, an RF mixer (Mini-Circuits ZP-3H), which can control the power output based on a DC voltage, was inserted into the control system between points (c) and (e) in Fig. 3-7. The mixer was first used in a saturated mode where output power is approximately independent of control voltage, then in an unsaturated mode where the power is linearly proportional to the control voltage. After adjusting the RF power in both cases to provide the same Ω, the lifetime of the atomic cloud was 7 s the saturated mode, but reduced to 900 ms in the unsaturated mode. Attempts to ramp the control from the saturated to unsaturated regimes

during the experiment destroyed the BEC in ∼400 ms. Any attempt to create an analog control of the RF power, including voltage controlled oscillator (VCO) modes with function generators such as the Agilent 33250a or the Stanford Research Systems DS345 met with similar reductions in lifetime.

3.6.3 Digital Frequency Synthesis

After analog control of the RF properties was ruled out, digital methods were tried. Most common (and relatively inexpensive) function generators that accept a trigger to start a ramp will return to the start frequency as soon as the sweep is complete, which is not useful. Mid-range synthesizers such as the Tabor 1072 and the Tektronix AFG3000 are able to precisely control *either* the frequency or the power, but controlling both simultaneously over the experimental time scale required too much memory[1]. Synthesizers able to control both parameters (digital AM and FM control with an arbitrary waveform) cost more than $8,000, so more custom solutions were pursued.

The last attempt to control the dressed Zeeman trap with pure digital synthesis was to program an Analog Devices AD9952 CMOS Direct Digital Synthesizer. The AD9952 is a single chip which synthesizes a sine wave based on real time programming. A prototype board costing only $200 was purchased, and was to be driven by a computer through a high speed digital I/O card. However, the decision was made to instead focus on the development of the optical lattice project [6] and the dressed Zeeman trap was abandoned.

3.7 Conclusion

After transfer into the dressed Zeeman trap, BEC lifetimes up to 30 s were measured, and BEC was observed in the trap for up to 60 s. Transverse trap frequencies as high as 250 Hz were measured. Future experiments implementing full digital control of the

[1]Sales representatives from both Tabor and Tektronix were extremely generous with the time they let me keep their demo units.

RF field could investigate the limits of tight transverse trapping. While competitive two-dimensional trapping regimes may not be attainable due to fundamental, physical limitations, this system may still prove useful in other experiments with its precise control of the trapping potential.

Chapter 4

Atom Trapping With a Thin Magnetic film

4.1 Introduction

4.1.1 Motivation

Micrometer scale magnetic traps for Bose-Einstein condensates have been the focus of much experimental work since their first demonstration [51, 28]. Their potential uses in atom interferometry, precision measurements, and experiment miniaturization have motivated many groups to develop sophisticated techniques for manufacturing and controlling these atom chips [64, 27, 66]. However, since the earliest inceptions of atom chips, current fluctuations and physical imperfections in the chip surface have lead to perturbations in the trapping potential that prohibit the coherent manipulation of atoms close to the surface [42, 45]. Permanent magnets offer a possible solution to several problems inherent to current carrying wire traps. First, the magnets are almost completely decoupled from the rest of the laboratory, minimizing the effects of environmental electrical noise. Second, they do not require current to be sourced or sinked, enabling designs that would be too complicated or impossible to create using electromagnets. Last, extremely high field gradients are possible close to magnetic domain boundaries, whereas traditional atom chip operation is limited

by heat dissipation from small wires. Although a substrate of magnetizable material may be made extremely smooth and uniform, imperfections in the process of etching [44] or writing magnetic structures could lead to some of the same problems as with wire-based designs. It is not yet known which technique will provide the best performance.

4.1.2 Outline

In this chapter I will describe our investigations into atom trapping with a thin magnetic film; specifically that of a hard disk platter written with a periodic pattern. This approach offers some advantages over previous work on neutral atom trapping and BEC creation using permanent magnets [66, 27]. Here we use a thin metallic film with a large remnant magnetization from a commercial product which has already been refined to a high degree and a writing technique more accurate than anything previously demonstrated. Cold ^{87}Rb atoms were first loaded into the magnetic potential formed by the disk and used RF evaporation to produce BEC. By changing the trapping potential, the atoms could be pushed closer to the surface of the disk to probe for imperfections in the potential. Finally, the BEC was dropped onto the disk from a height of 2.7 mm in an attempt to produce a specular reflection of the atomic cloud.

4.2 Surface Magnetization

4.2.1 Sinusoidal Pattern

In order to trap neutral atoms with magnetic fields, a field gradient is required. One way to create such a gradient is to start with a surface comprising the $\hat{x}\hat{z}$ plane, then create on the surface a magnetization of the form

$$\boldsymbol{M} = M_0 \cos(kx)\hat{y}. \tag{4.1}$$

This magnetization describes an alternating patten of up and down magnetic stripes, where M_0 is the magnetization of the material and k is the wavevector of the sinusoidal pattern. This can be replaced with a surface current $\boldsymbol{J}$ by taking the curl

$$\boldsymbol{J} = \nabla \times \boldsymbol{M} = -kM_0 \sin(kx)\,\hat{z} \tag{4.2}$$

Solving with physical boundary conditions [30, 33], the result is a magnetic field above the surface given by

$$\begin{pmatrix} B_x \\ B_y \\ B_z \end{pmatrix} = \frac{1}{2}\mu_0 M_0 \left(1 - e^{-kb}\right) e^{-ky} \begin{pmatrix} \sin(kx) \\ \cos(kx) \\ 0 \end{pmatrix}, \tag{4.3}$$

where b is the thickness of the magnetic material. This field is of uniform magnitude in the $\hat{x}\hat{z}$ plane and decays exponentially away from the surface as

$$\begin{aligned} B(y) &= \tfrac{1}{2}\mu_0 M_0 \left(1 - e^{-kb}\right) e^{-ky} \\ &= B_0 e^{-ky} \end{aligned} \tag{4.4}$$

. In the absence of external magnetic fields, this exponential decay provides an ideal potential for reflecting weak field seeking atoms [30], with gradient

$$B' = -kB_0 e^{-ky}, \tag{4.5}$$

which for a pattern wavelength $\lambda = 100$ μm and surface field $B_0 = 6000$ G provides a gradient of 7000 G/cm at a height of 100 μm above the disk. Even higher field gradients are possible with smaller patterns and closer to the disk.

4.2.2 Two Dimensional Trap

In the presence of gravity, if the surface is oriented horizontally, atoms may be trapped in a two-dimensional potential with vertical trap frequency

$$\omega_z = \sqrt{gk} \tag{4.6}$$

in a gravito-magnetic surface trap [30], where g is the acceleration of gravity. The potential minimum is located above the surface a distance

$$h = \frac{1}{k} \ln\left(\frac{g_F \mu_B B_0 k}{mg}\right), \tag{4.7}$$

where μ_B is the Bohr magneton, m is the atomic mass, and g_F is $\frac{1}{2}$ for the $|1,-1\rangle$ state and 1 for the $|2,1\rangle$ state. For example, a pattern wavelength of 5 μm would produce a trap 10 μm above the surface with $\omega_z = 560$ Hz. A small horizontal confinement could then be added, perhaps with an optical dipole trap, to contain the atoms in all three dimensions.

4.2.3 One Dimensional Trap

The addition of a bias field B_x along $\hat{x}$ (or B_y along $\hat{y}$) produces a series of quadrupole shaped field minima above alternating tracks, depicted in Fig. 4-1. These minima may then be used to trap weak field seeking atoms. Since each one is (to first order) a quadrupole magnetic field minimum, atoms which travel near the field zero may be lost due to Majorana spin flipping. A second bias field B_z along $\hat{z}$ removes this field zero, and atoms may be stably trapped near the surface with radial trap frequency

$$2\pi\omega_r = kB_x\sqrt{\frac{\mu_B g_F m_F}{mB_z}} \tag{4.8}$$

where $\mu_B g_F m_F$ is the Zeeman energy [30, 66].

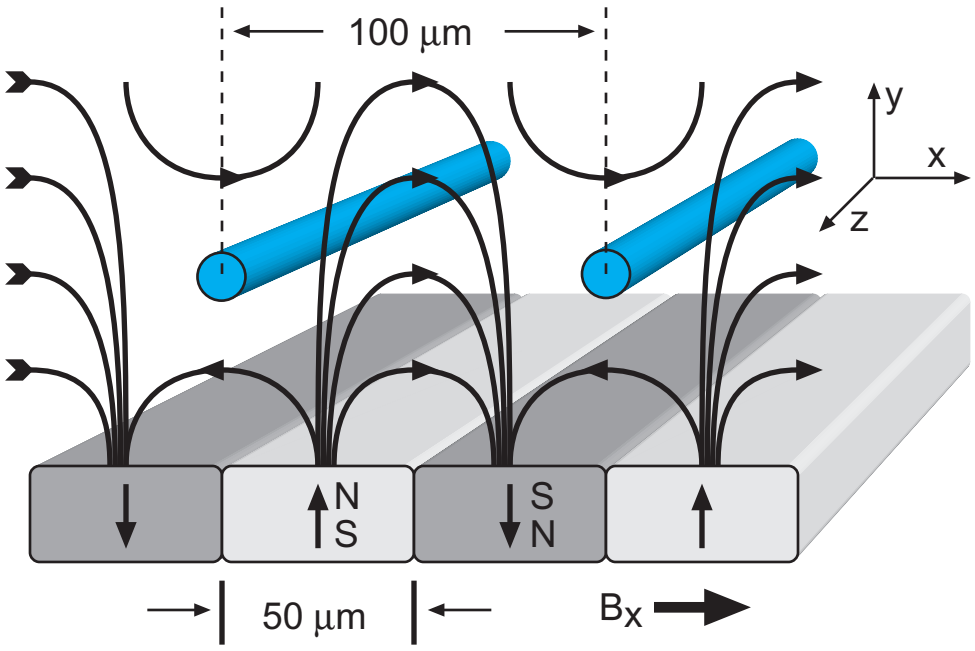

Figure 4-1: Geometry of the magnetic trap formed by a magnetic film. Magnetic field lines resulting from the addition of an externally applied radial ($\hat{x}$) bias field are shown. The tubes represent the locations of the field minima where atoms are trapped. The addition of an axial ($\hat{z}$) bias field of about 1.0 G prevents atom loss from Majorana spin flips.

4.3 Magnetic Media

The use of a magnetic storage medium for atom trapping is certainly not unique to this experiment [66, 27]. Videotape and floppy disks with sinusoidal patterns had previously been used to trap atoms in vacuum[1]. However, the storage density, and thus the minimum achievable magnetic structure size, were limited to >10 μm. Also, since they are formed of flexible materials, physical defects in the surface present a challenge to miniaturization. It seemed that the next logical choice was to move to a substrate that someone else had spent millions of dollars making as perfect as possible: hard disks.

4.3.1 Hard Disks

Commercial hard drives available before 2005 all used "in-plane" magnetization, where the magnetic field vector runs circumferentially around the disk. Information is encoded in an ac method where a change in the sign of the field means "1" and no change in the sign (where one was expected) means "0". Unfortunately, lines of magnetic field only leave the disk in small areas where the magnetization changes sign. This geometry is not useful for trapping atoms, as was unfortunately verified in vacuum.

Fortunately, the commercial push towards higher and higher information densities has very recently led to the development of hard disks using "out-of-plane" magnetization. At the time this experiment was conducted, no commercial out of plane disks were available to end users, as they were under a closely guarded process of development at pretty much every major hard drive manufacturer. I had the good fortune to make contact with Liesl Folks and Min Xiao at Hitachi Global Storage Technologies in San Jose, CA, and Min agreed to provide a few out-of-plane disks written with a specified pattern.

[1] Apparently videotape and floppy disk substrates are UHV compatible, to the pleasant surprise of the experimenters who first used them.

4.3.2 The "Out-Of-Plane" Prototype

The magnetic media used was a prototype hard disk with a radius of 65 mm and a thickness of 0.635 mm. The magnetizable material is a dual layer system with a 20 nm thick magnetic Co-Cr-Pt based oxide layer and a 200 nm thick "magnetically soft underlayer", both of which are also good conductors. The exact components are apparently a trade secret, but the atoms are only affected by the field that comes out of the disk. The substrate is glass, the coercivity is 6.8 kOe and the magnetic remnant is 0.64 memu/cm^2. The easy axis of magnetization of this prototype "out-of-plane" disk is aligned normal to the surface of the disk, as opposed to most modern commercial hard disks which are magnetized in the plane of the surface. This alignment of the magnetic domains produces about 6000 G at the surface.

4.3.3 Vacuum Compatibility

One concern about the disk was that it could not be baked to the high temperatures (150 C) that we normally use to reach UHV. Digital data on similar disks is guaranteed to 80 C, but at 100 C the data starts to degrade rapidly as the magnetic domains randomize. The solution was to pre-bake the entire science chamber apparatus, minus the disk, to 150 C for about a week to reach UHV conditions. The system was briefly opened up to air, the disk was installed, and then the chamber was pumped down again. The chamber was then heated only to 70 C for a few days, and after cooldown the pressure was $< 10^{-10}$ Torr. Apparently, hard disk platters are UHV compatible.

The signal decay rate quoted for this disk by its designers at room temperature was 0.4% per decade, increasing to 0.8% per decade at 70 C. The decay rate is defined as

$$\delta = 100 \times \frac{A(t) - A(t_0)}{A(t_0)} \frac{1}{\log\left(t/t_0\right)} \tag{4.9}$$

where $A(t)$ is the signal amplitude at time t, and $A(t_0)$ is the signal amplitude at t_0. a decay rate of 0.8% per decade is considered stable for data storage, and the only significant randomizing spin flips will occur away from the track boundaries.

4.3.4 Disk Properties

The disk was provided to us pre-written using a Guzik spin stand, which is essentially a hard disk read/write head with absolute positioning capability. This method of writing allows for the creation of truly arbitrary pattern impossible to create with larger scale magnetic writing devices [66] or physical structures [27], and produces smaller and cleaner structures than optical writing techniques [17]. Two patterns were used in this experiment, written on different radial regions of the same disk. The first region had alternating stripes of up and down magnetization with a period of $2\pi/k = \lambda = 100.0$ μm and the second had $\lambda = 1.0$ μm. The media has an almost perfectly square hysteresis loop which precludes a purely sinusoidal magnetization. The pattern was instead written as a square wave, and the higher Fourier harmonics should be negligible at the height where we trap atoms [30]. Figure 4-2 shows a magnetic force microscopy image of the disk after writing[2] which shows a significantly less noisy pattern than magneto-optical thin films written with laser beams [40]. Atomic force microscopy showed a physical roughness of $\sim$3 nm over a region of 50 μm.

4.4 Experimental Procedure

4.4.1 Atom Delivery to the Science Chamber

Cold atoms were delivered to the surface in a two step process. First, cold ^{87}Rb atoms in the $F = 1, m_f = -1$ state were created in the main chamber Ioffe-Pritchard magnetic trap with $T > T_c$ where T_c is the critical temperature for Bose-Einstein condensation (see [72, 63] for more details). Typically, if evaporation to 0.7 MHz produced a pure BEC, we would stop evaporation at 2.0 MHz. The atoms were then transferred to the optical dipole trap by simultaneously switching off the magnetic trap and turning on the optical trap. The thermal cloud was then transported 36 cm to the science chamber. The optical dipole trap was formed by a $\lambda = 1064$ nm laser

[2]The image was produced by Min Xiao at HGST with a Digital Instruments NanoScope.

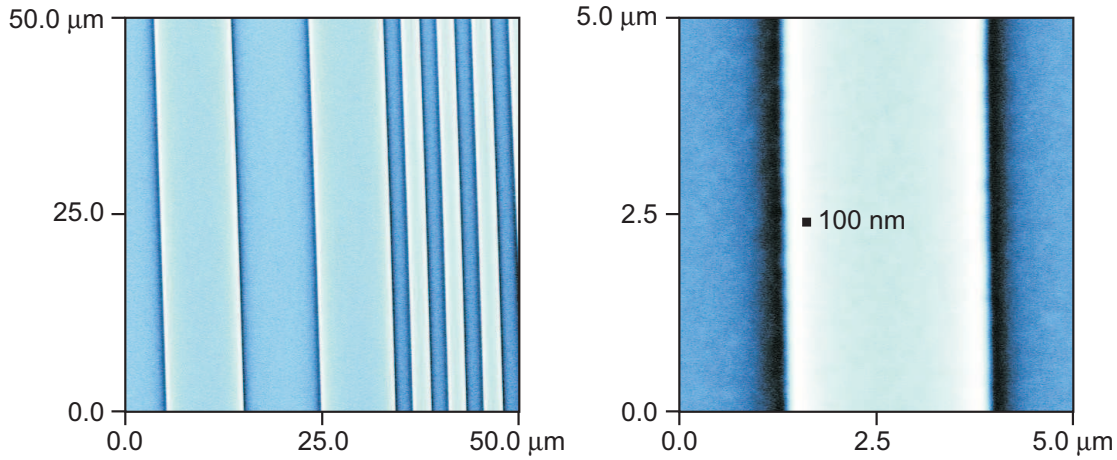

Figure 4-2: Magnetic force microscopy image of a sample disk. The left image is a scan over a boundary region where the pattern wavelength changes from $\lambda = 50$ μm to $\lambda = 5.0$ μm, showing the capability for multiple types of structures on a single disk. The right image is a higher resolution scan over an area with $\lambda = 5.0$ μm, showing the uniformity of the track edges. The characteristic size of the roughness of the domain boundaries is about 30 nm.

focused to a 30 μm $1/e^2$ radius spot, and the focus (with the atoms) was translated into the auxiliary chamber as described in [26]. By transporting atoms just above T_c, the cloud was less sensitive to vibrations, and higher laser powers could be used without causing rapid three-body losses.

4.4.2 Z-Wire Trap

After delivery to the science chamber, the final cooling was accomplished by loading into a Z-wire trap as in [66] and RF evaporating to BEC. The Z-wire trap was formed by a 1.2 mm diameter copper wire with a 5 mm Z center section carrying 10 Amps, shown in Fig. 4-3. 10 G radial bias field was added to create a trap with frequencies $(\omega_x, \omega_y, \omega_z) = 2\pi \times (90, 90, 20)$ Hz located 0.8 mm above the top of the wire. The disk was located above the wire but below the atoms, enabling us to maneuver the atoms arbitrarily close to the surface. Initial attempts to load condensates from the wire trap into a $\lambda = 100$ μm surface trap site were unsuccessful due to a mismatch in the trapping potentials. Gravitational sag in the wire trap caused the atoms to gain $\sim$300 kHz in energy as they fell into the surface potential in a "waterfall" effect as

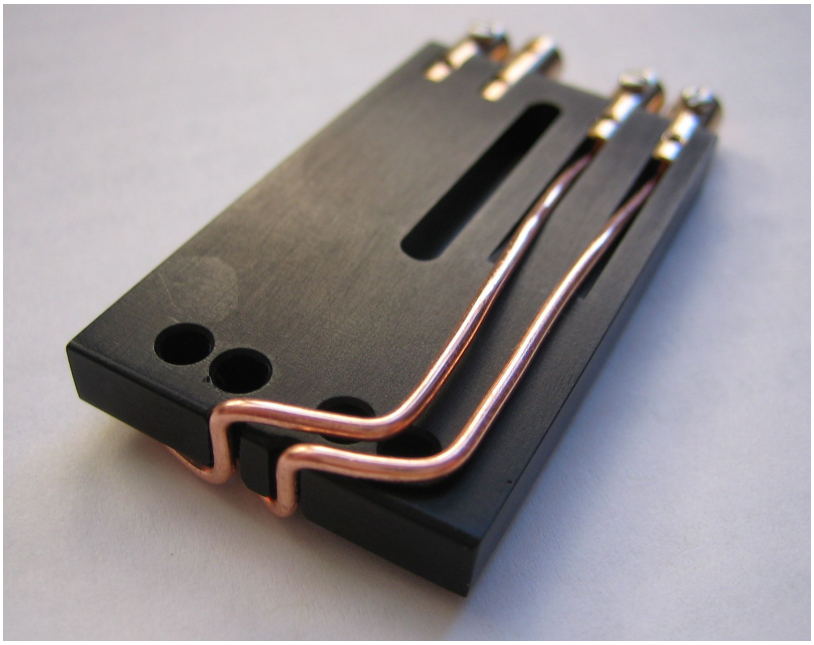

Figure 4-3: Photograph of the Z-wire trap. The Z-wire trap was wound with 1.2 mm diameter bare copper wire. The wires were used to enable trapping on two well-separated parts of the disk, and the unused wire was used as a RF antenna for evaporation. The wire was mounted to an aluminum support that maintained the shape and position of the wire. The support was anodized to prevent electrical shorting, and the combination of aluminum and anodization did not cause enough outgassing to noticeably affect the vacuum. The dimensions of the support are 23 mm $\times$ 47 mm $\times$ 5.0 mm.

the traps merged. Increasing the current in the z-wire could have lessened this effect, but this was limited by heat dissipation rates[3]. The best solution was to load the atoms directly onto the surface from the optical trap.

4.4.3 Surface Loading

The atoms were loaded onto the surface in the $\lambda = 100$ μm region from the optical trap by translating the focus of the optical trap to a position parallel to and 50 μm above the surface. The Z-wire trap was ramped up in 200 ms to provide axial confinement, and a small B_x created radial trapping on the surface. The optical trap was ramped off linearly over 2 seconds, transferring the atoms with almost unity efficiency. The

[3]Running 15 Amps CW outside of the vacuum made the wire way too hot to touch, and would have demagnetized parts of the platter due to heating above the Curie temperature

disk was positioned along $\hat{k}$ (or $\hat{x}$) to maximize the transfer of atoms into a single trap, The narrow width of the optical trap enabled loading of >90% of the atoms into a single surface trap site. If misaligned, or if an especially large thermal cloud was transported, up to three surface traps could be loaded. RF Evaporation over 20 seconds from 1.200 MHz to 0.890 MHz produced a BEC with approximately 50,000 atoms in a trap with $(\omega_x, \omega_y, \omega_z) = (390, 390, 9) \times 2\pi$ Hz and a lifetime of $\sim$ 30 s (Fig. 4-4). Observation of the bimodal density distribution of the cloud in trap was the most reliable method to optimize evaporation, and condensate fractions of >80% were observed.

4.4.4 Surface Imaging

The atomic cloud was detected with on-resonance absorption imaging (Fig. 4-7) on the $F = 2 \rightarrow F' = 3$ transition. The atoms were optically pumped along another axis from the $F = 1$ state to the $F = 2$ state prior to and during the imaging pulse. The platter is a good reflector (>95%) for 780 nm light, so grazing incidence imaging was used to measure the distance from the atoms to the surface (Fig 4-5). In this configuration, probe light reflects off the disk at an angle of only a few degrees above horizontal. Two images of the atoms are formed on the camera: One image from the beam portion which passes through the atoms and then reflects off the disk, and another image from the beam portion which first bounces of the disk and then passes through the atoms. In the limit of a small angle of incidence, the distance between the atoms and the surface is easily calculated as half the distance between the cloud images.

Normal incidence imaging was also used, in which case the imaging light passed through the atoms twice, bouncing off the disk (Fig. 4-6). Since it was difficult to perfectly align the beam to normal incidence, images of atoms held far above the disk (>200 μm) sometimes showed a double image where the two clouds were not separable. Those images were difficult to analyze. The lack of physical structures on the surface resulted in good image quality, even compared to normal, direct imaging. The top and side imaging beam paths were used interchangeably as pump and probe.

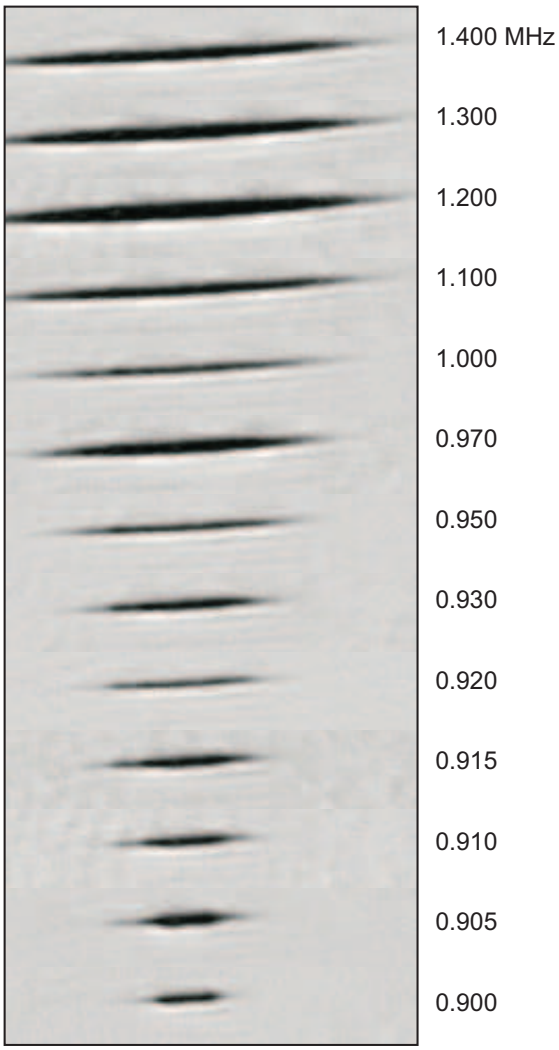

Figure 4-4: Evaporation to BEC on the disk. This series of normal incidence images shows the transition from a thermal cloud to a BEC as the RF knife is lowered. Since releasing the atoms for ballistic expansion in time-of-flight was impossible, the bimodal appearance of the trapped cloud was used as a key signature for BEC. The width of the image is 1.2 mm.

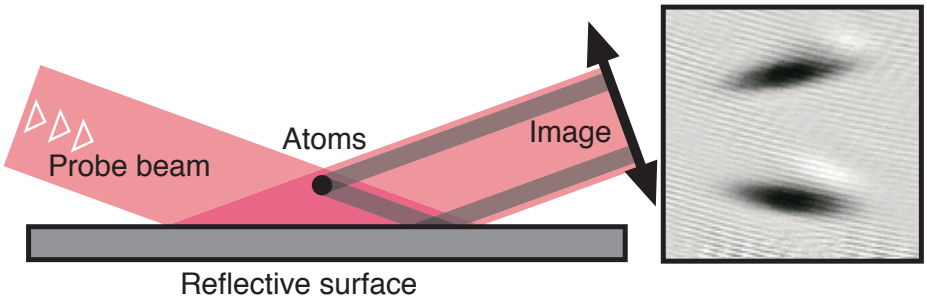

Figure 4-5: Hard disk platter side imaging. Probe light reflects off the surface of the disk at a grazing incidence and creates an absorption image at the camera.

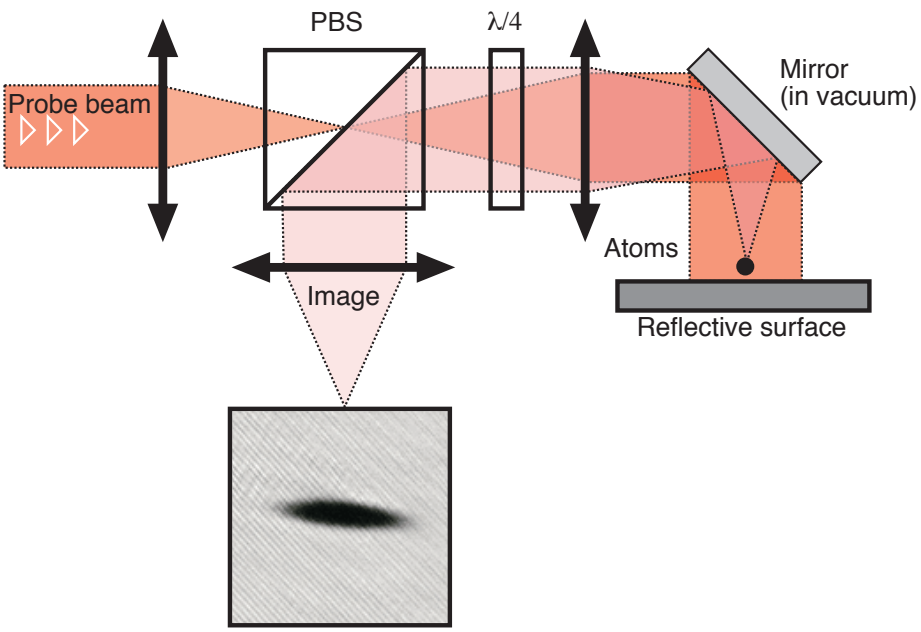

Figure 4-6: Hard disk platter top imaging. Circularly polarized imaging light reflects off the surface of the disk at normal incidence. The returning light is separated from the probe light with a polarization beam splitting cube. The mirror above the disk is fixed in vacuum.

Attempts to release the atoms from the trap and observe ballistic expansion in time of flight were hindered by the geometry of the system and the static nature of the magnetic surface, so all of the imaging was done in-trap.

4.5 Surface Trap Results

4.5.1 Trap Frequencies

The axial trap frequency in the surface trap was measured by imaging oscillations of the atomic cloud, and radial trap frequencies were measured by parametric heating [Fig. 4-8]. Parametric heating of the atomic cloud was driven by small current oscillations in the secondary Z-wire, and observed by measuring atom loss. The Z-wire trap was left on at all times to provide axial trapping. Ramping up the current in external electromagnets increased B_x, and ω_r as high as $2\pi \times 5$ kHz was measured. Using a disk with $\lambda = 10.0$ μm, we have measured ω_r as high as $2\pi \times 16$ kHz. High transverse trap frequencies are desired for studies of 1D systems [38], but atom heating and loss

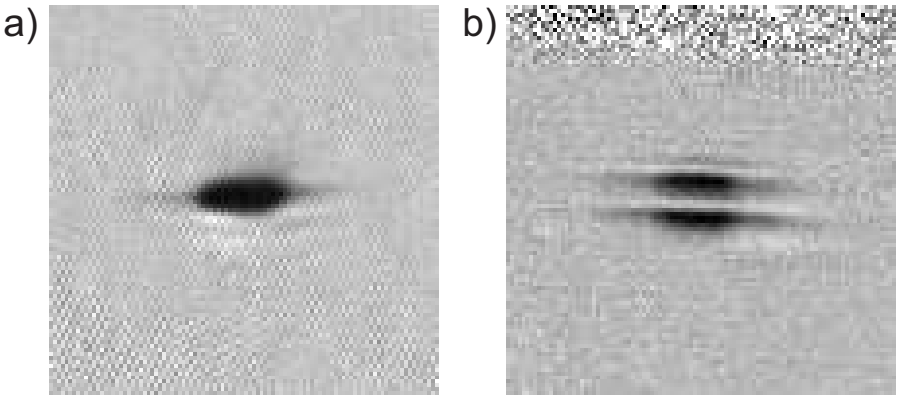

Figure 4-7: Absorption image of the BEC in trap near the surface. a) Top imaging. The field of view is 0.58 mm × 0.58 mm. b) Side imaging. The field of view is 0.56 mm × 0.56 mm. The double image comes from the reflection of the imaging beam in the platter surface. The trap frequencies were $2\pi\times$(400, 400, 10) Hz. The configuration of the experiment prevented ballistic expansion, but the bimodal distribution in trap is still clear.

at higher trap frequencies prevented such studies here.

4.5.2 Lifetime

While trapped 40 μm above the surface, the BEC had a lifetime of ∼30 s. Previous experiments with atomic clouds magnetically trapped near conducting surfaces showed atom loss resulting from spin flips driven by Johnson noise [35, 45, 61]. This noise is a result of thermal eddy currents in the metallic surface which drive magnetic transitions into the untrapped state. In the regime where the thickness of the metallic film is much less than the skin depth of the resonant radiation, the decay rate is

$$\Gamma_{F,m} = \frac{C_{F,m}^2 C_0}{d\,(1+d/t)\,(1+2d/w)} \tag{4.10}$$

where t and w are the thickness and width of the surface, and d is the distance between the atom and the surface. $C_0 = 88\ \mathrm{s}^{-1}\ \mu\mathrm{m} \times (T/300\ \mathrm{K})(\rho_{Cu}/\rho)$ where T is the temperature of the metal, ρ is the resistivity of the surface, and $\rho_{Cu} = 1.7 \times 10^{-8}\ \Omega$ m is the resistivity of copper. $C_{F,m}^2 = |\langle F, m-1|S_-|F,m\rangle|^2$ is the strength of the spin changing transition where S_- is the spin lowering (or raising) operator [45]. In the case for atoms in the $|1,-1\rangle$ state over a surface with $w \gg t$

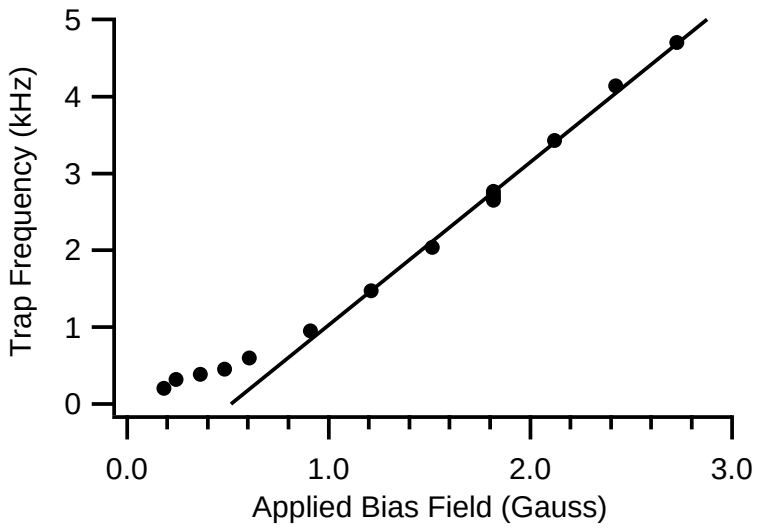

Figure 4-8: Radial trap frequency vs applied radial magnetic field. Atoms were loaded into a single trap site on the surface and evaporated to BEC. The trap frequencies were measured with parametric heating, but above 5 kHz other heating effects made it difficult to resolve reliably. The deviation from linearity at low applied fields is most likely due to a small, off-axis, residual bias field.

and $w \gg d$, this reduces to

$$\Gamma_{1,-1} = \frac{C_{1,-1}^2 C_0}{d\,(1 + d/t)} \tag{4.11}$$

Assuming $\rho = \rho_{Cu}$, and taking the rest of our experimental parameters $t = 200$ nm, $d = 40$ μm, and $C_{1,-1}^2 = 1/8$, we calculate a spin flip rate of only 0.1 s^{-1}. Combining this loss process with losses from collisions with background gasses (Γ_{bg}) results in a net lifetime of

$$\tau = \frac{1}{\Gamma_{bg}} + \frac{1}{\Gamma_{1,-1}} \tag{4.12}$$

Any spin flip loss was below the level of our 1-body losses at a vacuum pressure of $\sim 5 \times 10^{-11}$ Torr.

4.5.3 Magnetic Potential Imperfections

The BEC was also used to probe imperfections in the trapping potential. After evaporation, the axial trapping frequency was reduced from 10 Hz to ∼1 Hz to allow the

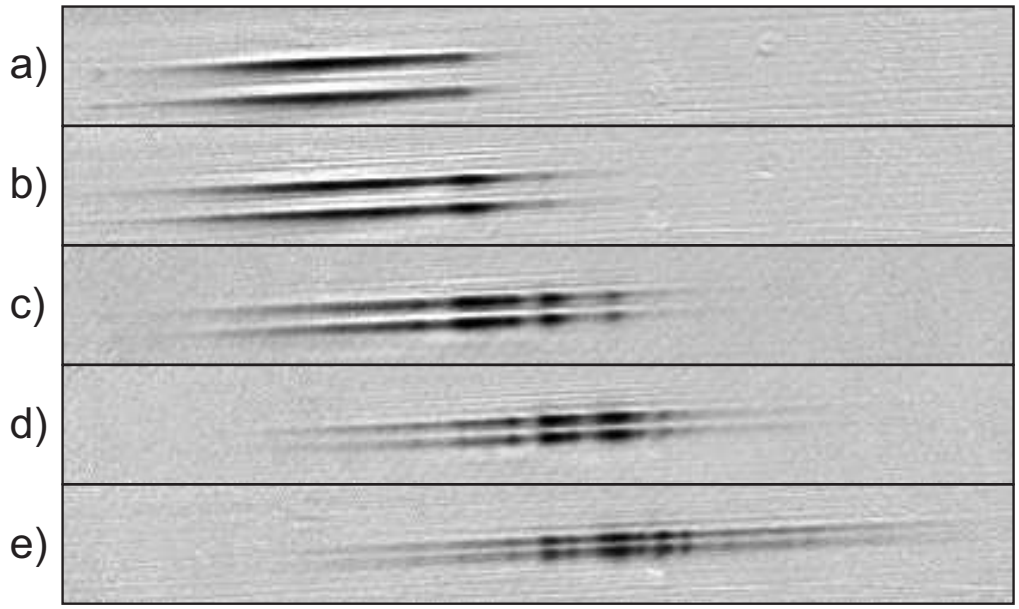

Figure 4-9: Breakup of the atomic cloud as the atoms approached the surface. The thermal cloud was evaporated to $T \approx T_c$, then the axial trapping frequency was reduced to from 10 Hz to 1 Hz to allow the atoms to expand in one dimension. The axial bias field was then increased to push the atoms closer to the surface, and the atoms were imaged in trap. The grazing incidence imaging used here produces a double image of the atoms from the primary and secondary reflections of the imaging beam off the disk. The field of view is 0.29 mm $\times$ 2.3 mm, and each frame is an average of five distinct images to reduce noise for clarity. At distances smaller than 40 μm, significant breakup was observed. Height for the images shown: a) 35 μm b) 29 μm c) 25 μm d) 22 μm e) 19 μm.

cloud to expand slightly in one dimension to increase the sensitivity and the measurement area, and the radial bias field (B_r) was increased to push the atoms closer to the surface. At distances closer than 40 μm, breakup of the atomic cloud was observed (Fig. 4-9), and the strength and spatial frequency of the perturbations increased as the atoms neared the surface, similar to [42, 7]. The magnitude and size scale of these imperfections can be attributed to the sputtering process used to create the film. Magnetic grain nucleation occurs randomly, resulting in small angular misalignments of the axes of anisotropy of individual magneto-crystalline domains (typically a few degrees), the individual magnetic grains can vary in size by about 25% of their $\sim$7 nm diameter, and the magnetic moments have a distribution of magnitudes. All of these phenomena create imperfections in atomic trapping potentials.

While the presence of these perturbations does not necessarily preclude the creation of neutral atom waveguides using this type of substrate, it does limit its usefulness. High trapping frequencies and single transverse mode confinement require close proximity to the surface and will suffer from the observed imperfections. However, for use as a high reliability, low noise, and low cost waveguide at distances >50 μm, commercial metallic, magnetic thin films are ideal.

4.6 Magnetic Mirror

The magnetized surface was also examined for its usefulness as an atom mirror, as in [58, 65, 44]. In order to minimize residual and time dependent magnetic fields (from magnetic trap turnoff), all optical trapping was first used to create a BEC. The optical dipole trap provided only weak axial confinement, so a second, 200 mW laser beam with $\lambda = 1064$ nm and 200 μm waist was added in a crossed configuration, and allowed more efficient evaporation. To evaporate to BEC the power was reduced over 2.0 s. An axial bias field $B_z = 1.2$ G was maintained throughout the experiment, and B_x and B_y were minimized to <20 mG.

The region of the disk used as a magnetic mirror was written with $\lambda = 1.0$ μm. This value was chosen to be large compared to the magnetic writing precision, but small compared to the extent of the atomic cloud, and hopefully small compared to the deBroglie wavelength of the atoms. The BEC was released from the crossed ODT 2.7 mm above the disk. The atoms fell under gravity for 23.5 ms and then reflected off the magnetic potential. Up to three bounces off the surface were observed (Fig. 4-10). The atomic cloud was imaged (in separate experiments) from both the top and side after various times of flight. Side imaging showed that the reflection from the disk did not significantly affect the axial or vertical velocity distributions of the atomic cloud. Top imaging, however, showed significant spreading along the vector of the magnetic pattern after reflection, analogous to bouncing off a rough mirror [55]. The magnitude of this dispersion was minimized by fine tuning B_x and B_y, but was impossible to eliminate in our apparatus. Before bouncing off the disk, the $\hat{x}$ width of the cloud

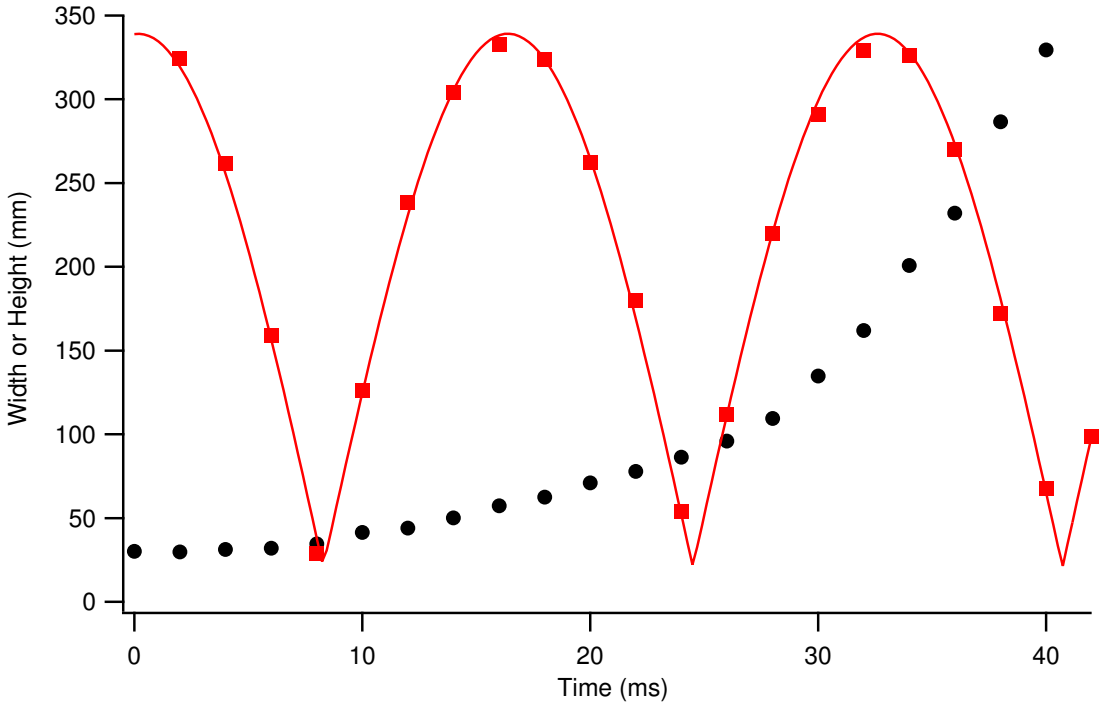

Figure 4-10: Width and position of the bouncing BEC. After release from the crossed ODT trap above the region of the disk with $\lambda = 1.0\mu$m, the BEC was imaged after various times. Side imaging showed the height of the BEC above the disk as it bounced (squares), and top imaging showed the width of the atomic cloud (fit to a Gaussian) as it expanded (circles). At times <8 ms, the expansion is purely due to the chemical potential of the atoms. Between 8 and 24 ms, the expansion rate of the cloud is increased due to dispersive effects. After the second bounce at ∼24 ms, the expansion rate increased dramatically. The line is a fit to $y_0 + A\,|\cos(2\pi x/\tau + \phi)|$ with $y_0 = 21 \pm 3$ μm, $A = 318 \pm 4$ μm, $\tau = 32.44 \pm .08$ ms, and $\phi = -0.03 \pm .01$ rad.

expanded by 1 mm/s, and after bouncing the $\hat{x}$ width increased by 34 mm/s. The reflection was not performed on the region with $\lambda = 100.0$ μm. Experiments using a different disk with $\lambda = 10.0$ μm showed similar effects.

4.6.1 Analysis of Dispersive Reflection

The magnetic properties of the hard disk surface are one possible source of the observed expansion after reflection. While the theory presented earlier (Eq. 4.1) applies to a sinusoidally magnetized surface, the square hysteresis loop and directional anisotropy of digital recording media prevent recording of a pure sine wave, instead forming a square wave approximation of that sine, as discussed in [30]. While the

higher harmonics resulting from this approximation do not necessarily adversely effect BEC trapping, they create a corrugation of the planar equipotential that prevented the specular reflection of a macroscopic atomic cloud. Another contribution to the roughness of the reflection potential is the existence of small, stray magnetic fields. Any nonzero component of $\boldsymbol{B}$ in the $\hat{x}\hat{y}$ plane creates a regular corrugation of the potential in the plane, further inhibiting specular reflection.

4.7 Hard Disk Platter Conclusion

In conclusion, we have demonstrated BEC production on the surface of a hard disk platter. Small scale imperfections in the magnetization caused condensate fragmentation close to the surface, prohibiting its use as a neutral atom waveguide. The disk was also used as an atom mirror, and specular reflection was observed on two axes. Microtraps based on permanent magnets, and in particular magnetic metallic thin films, may become an alternative to atom chips using current-carrying wires if the fabrication can be further improved, e.g. by using molecular beam epitaxy, and the writing process improved by using write heads optimized for recording DC structures on media with B field perpendicular to the surface.

4.7.1 Special Thanks

I would like to especially thank Min Xiao at HGST for writing several disks for us and providing the MFM images, this work would not have been undertaken without her assistance. She provided three disks which we put into vacuum, and each one took many hours for her to prepare.

Chapter 5

The Mott Insulator Atomic Clock

5.1 Introduction

5.1.1 Abstract

We implemented a proof-of-principle atomic clock using a ^{87}Rb Bose-Einstein condensate confined in an 3D optical lattice. Several typical sources of systematic error were eliminated by preparing the atoms in the Mott Insulator (MI) phase before measurement. The suppression of tunneling in the MI phase permitted longer measurements than possible with other optical confinement techniques, as well as elimination of the density shift due to the discretized density resulting from integer filling factors. The hyperfine transition of ^{87}Rb was measured with a FWHM linewidth of 1.2 Hz and an uncertainty of 0.2 Hz out of 6.8 GHz.

5.2 Atomic Clocks

Precision frequency and time measurements provide a fundamental reference for the basis of nearly every physical measurement. Modern measurements have improved the accuracy of atomic clocks to the 10^{-15} level [49, 16, 54, 14], and recent experiments with optical transitions in trapped, neutral atoms promise precision at the 10^{-18} level [73]. In fact, as the most accurate measurement *of any kind*, atomic clocks are

being used to study the time dependence of fundamental constants such as α. Great care must be taken to protect the atomic clock system from perturbations from the environment. Since forces used to trap the atoms may perturb the system, fountain clocks which measure resonance frequencies with the atoms in free-fall have been the standard. However, the interrogation time, and thus the bandwidth, is limited by gravity and the size of the system. Recent experiments have made progress with measuring trapped neutral atoms and ions, as the tools necessary to trap without perturbation have been developed. As these trapped atom clocks reach new records of precision, a new problem emerges; interactions within the atomic cloud begin to affect the measurement.

5.2.1 Motivation

Unwanted perturbations to an atomic clock system can come from external sources, such as external trapping for cold atoms or stray electromagnetic fields in the laboratory, or from internal sources, such as the atomic cold-collision shift [19, 54, 67] or dipole-dipole interactions [19, 60]. Although systems can be shielded from external perturbations through clever engineering, it is more difficult to control the effect of interactions, as they are "built in" to the atoms. Simultaneously interrogating a large number of atoms N can increase the signal to noise ratio by $\sqrt{N}$, but increasing the atom number typically comes at a cost of increased density, leading to greater uncertainty due to interactions. For example, the microwave hyperfine transition of cold ^{87}Rb at a typical density of 10^{13} cm^{-3} will be perturbed by the "clock" shift at a level of 2 Hz. One way to minimize such collisions is to hold each atom apart from the others in an optical lattice.

5.2.2 This Experiment

In this work we implement an atomic clock by measuring a microwave hyperfine transition in a ^{87}Rb Bose-Einstein condensate (BEC) confined in a 3D optical lattice. Atomic clocks using neutral atoms in an optical lattice have been demonstrated previ-

ously [73, 3, 46], but here we eliminate a key source of systematic error by increasing the depth of the lattice potential to confine the atoms in the Mott insulator (MI) regime. In the MI phase, tunneling is suppressed due to the inter-site interaction energy barriers, reducing the lattice depth required to minimize interactions. This reduced lattice depth avoids complications such as higher order light shifts [43]. As recently shown [6], the microwave spectrum of the MI shows discrete peaks corresponding to the integer filling factor of individual lattice sites. This discretization of the density shift eliminates density dependent errors in the measurement of the transition frequency. Systematic shifts due to trapping laser intensity may also be extrapolated to zero intensity by varying the laser power over a wide range within the MI regime.

5.3 Lattice Theory

5.3.1 The Bose-Hubbard Hamiltonian

Bosons held in a 3D optical lattice with repulsive interactions are described by the Bose-Hubbard Hamiltonian [20, 34]

$$\hat{H} = -J \sum_{\langle i,j \rangle} \hat{a}_i^\dagger \hat{a}_j + \frac{1}{2} U \sum_i \hat{n}_i(\hat{n}_i - 1) + \sum_i (\epsilon_i - \mu)\hat{n}_i, \tag{5.1}$$

where J is the tunneling term between nearest neighbors, $\hat{n}_i = \hat{a}_i^\dagger \hat{a}_i$ is the number of atoms in the i^{th} lattice site, U is the repulsive onsite interaction, $\epsilon_i = V_{ext}(r_i)$ is the energy due to the external confinement, and μ is the chemical potential. The onsite interaction is expressed as $U = (4\pi\hbar^2 a/m) \int |w(x)|^4 d^3x$, where a is the s-wave scattering length, m is the atomic mass, and $w(x)$ is the single particle Wannier function. The first term in the Hamiltonian tends to de-localize atoms over the lattice due to tunneling, while the second term tends to localize atoms to lattice sites due to repulsive atom-atom interactions. The ratio J/U is thus the primary descriptor of the behavior of the atoms. For small lattice depths, the ratio J/U is large and the

system behaves as a superfluid.

5.3.2 The Mott Insulator

As the lattice depth is increased, J/U increases, the localizing effects of the interaction begin to dominate, and the system undergoes quantum phase transition to a MI phase. The MI phase is characterized by Fock states, where atoms are localized to individual lattice sites with integer occupation number. With the spherically symmetric external confinement

$$\epsilon_i = V(r_i) = \frac{1}{2} m\omega_{trap}^2 r_i^2, \tag{5.2}$$

where r_i is the distance to the lattice site i from the center of the trap, and the chemical potential of the condensate in the Thomas-Fermi approximation

$$\mu = \left(\frac{15}{16} \frac{(\lambda/2)^3 \, m^{3/2} N \omega_{trap}^3 U}{\pi\sqrt{2}} \right)^{2/5}, \tag{5.3}$$

the peak density in a given lattice site is then

$$\rho(r_i) = \frac{1}{U} \left(\mu - \frac{1}{2} m\omega_{trap}^2 r_i^2 \right). \text{ [24]} \tag{5.4}$$

In the MI phase, this describes a series of concentric shells, each with uniform occupation

$$n = \lfloor \frac{\mu - \epsilon_i}{U} \rfloor \tag{5.5}$$

where $\lfloor x \rfloor$ is the largest integer less than or equal to x. It is this discrete filling which we utilize to eliminate the density shift of our atomic clock.

5.3.3 Density Shifts

The density dependent shift in ^{87}Rb is determined by the difference in the scattering lengths a_{11} and a_{21}, where $a_{21}(a_{11})$ is the scattering length between an atom in the $F = 1, m_F = -1$ state and one in the $F = 2, m_F = +1$ ($F = 1, m_F = -1$) state. The

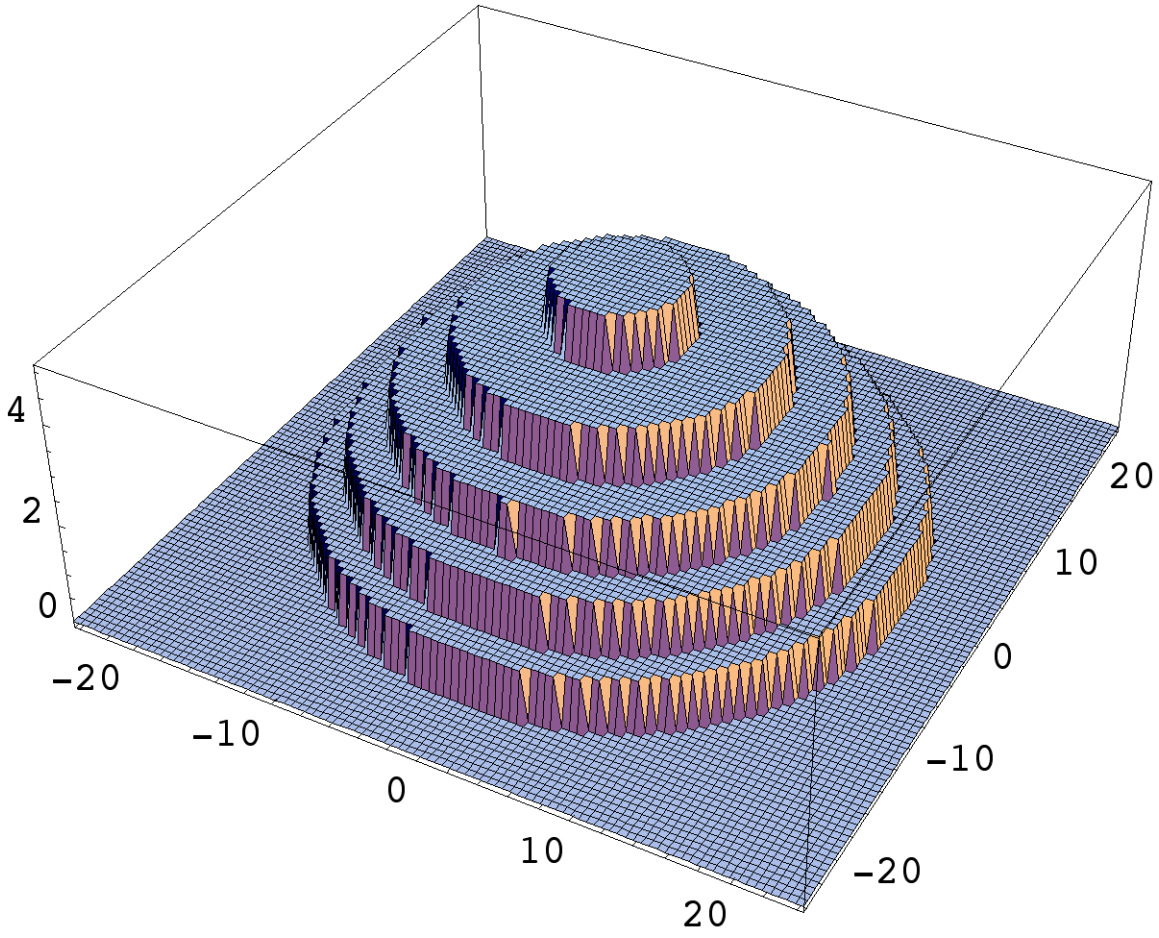

Figure 5-1: Theoretical "wedding cake" density profile. This figure shows a single slice through the center of the MI for our experimental parameters with $N = 4 \times 10^5$ and a lattice depth of 35 E_{rec}. The horizontal axes are in μm and the vertical axis is the filling factor. Each grid square represents approximately one lattice site.

difference in the scattering lengths results in a mean field energy shift

$$\Delta E = \frac{h^2}{\pi m \rho}(a_{21} - a_{11}) \tag{5.6}$$

will then resolve to discrete frequency shifts for integer lattice filling factors, where ρ is the atomic density. The resulting microwave spectrum for a BEC in the MI regime is a series of peaks, and the frequency difference between neighboring MI shells is then

$$\delta\nu = \frac{U}{h}\frac{(a_{21} - a_{11})}{a_{11}}. \tag{5.7}$$

5.4 Experimental Procedure

5.4.1 BEC Creation

For our experiments, the BEC was created using forced radio-frequency evaporation of a ^{87}Rb atomic cloud in the $|F, m_F\rangle = |1, -1\rangle$ state, as described previously in [71]. The trapping potential was formed by the combination of a Ioffe-Pritchard magnetic trap and a retro-reflected, cross polarized optical dipole trap. The optical trap was oriented perpendicular to the weak axis of the magnetic trap to provide a more spherical geometry for better mode matching to the optical lattice [6]. BECs containing $\sim 1.5 \times 10^6$ atoms with no discernible thermal component were held for 5 seconds with a constant RF knife, reducing shot-to-shot atom number fluctuations to below 5%. For most measurements, a fast RF sweep through the RF resonance was used to reduce the atom number by ∼75%.

5.4.2 The Optical Lattice

A 3D optical lattice was then adiabatically ramped on using an exponential increase with a 40 ms time constant. Two lattice axes were formed by increasing the intensity in fully retro-reflected beams, while the third axis was formed by rotating the polarization of the retro-reflected optical dipole trap using a liquid crystal waveplate

(Fig. 5.4.2). The lattice beams were all derived from the same laser with $\lambda = 1064$ nm, and were detuned from each other by acousto-optic modulators. The beams also all had roughly equivalent $1/e^2$ beams waist radii of 150 μm, focused on the atoms. The lattice depth was increased up to 35 E_{rec} where $E_{rec} = \hbar^2 k^2/(2m)$ and $k = 2\pi/\lambda$ is the wavevector of the lattice[1]. After ramping up the lattice, the atoms were held for 50 ms before measurement to compensate for transient nematic effects in the liquid crystal polarization rotator. The resulting MI structure was calculated to contain approximately 7×10^4 atoms in the $n = 1$ shell.

5.4.3 MI State Creation

As the lattice is ramped up, the ac Stark shift and the density shift begin to broaden and move the microwave resonance to lower frequencies. As the lattice depth is increased, the tunneling rate decreases until it is completely suppressed at depths greater than approximately 15 E_{rec} due to the transition to the MI phase. Discrete peaks begin to appear, corresponding to cold collision density shifts resulting from integer filling factors within lattice sites. The observation of discrete peaks is direct evidence for the suppression of tunneling by interactions when the MI transition is reached. Tunneling of atoms between sites of different occupation number during the microwave pulse would smear out the discrete peaks and eventually lead to peaks reflecting the clock shift at an averaged density. We estimate the tunneling time in the absence of interactions using a double-well model to be $h/4Jnz$, where z is the number of next neighbors. For $n = 1$, the tunneling time is $\sim$5 ms at 20 E_{rec}, 13 ms at 25 E_{rec} and 60 ms at 35 E_{rec}. A very deep lattice would localize atoms even for a thermal or non-interacting gas. However, for our lattice depths no discrete spectrum was observed when the cloud was heated during the ramp up by misalignment of the lattice beams. Our spectra were taken under conditions where the condensate fraction after ramp down of the lattice was greater than 80%.

[1]This corresponds to a peak intensity in each beam of $\sim$240 mW/cm^2 for ^{87}Rb with $\lambda = 1064$ nm.

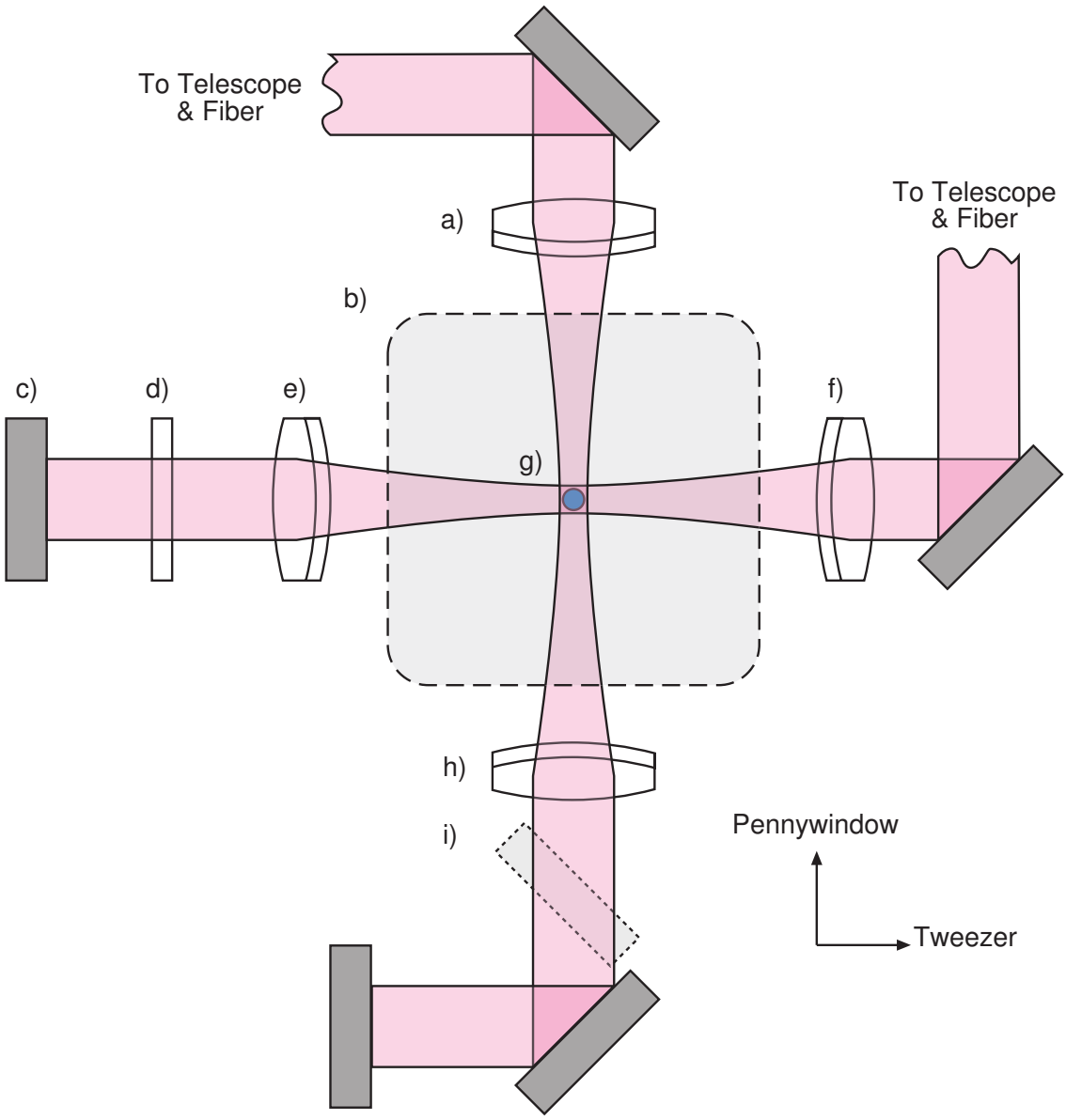

Figure 5-2: Setup of the optical lattice. The light is delivered to the machine table via optical fibers for each axis, then the beams are expended with telescopes before the optical setup depicted in the cartoon. a) 300 mm lens. b) Boundary of vacuum chamber. c) Retro mirror. d) Liquid crystal waveplate. e) 500 mm lens. f) 400 mm lens. g) Atomic cloud. h) 200 mm lens. i) Motorized flipper mirror for MOT axis utilization. The vertical axis, which coincides with the imaging axis, is not pictured. The waveplate is used to adjust the polarization of the reflected tweezer axis beam to zero contrast during evaporation and maximum contrast during the lattice rampup.

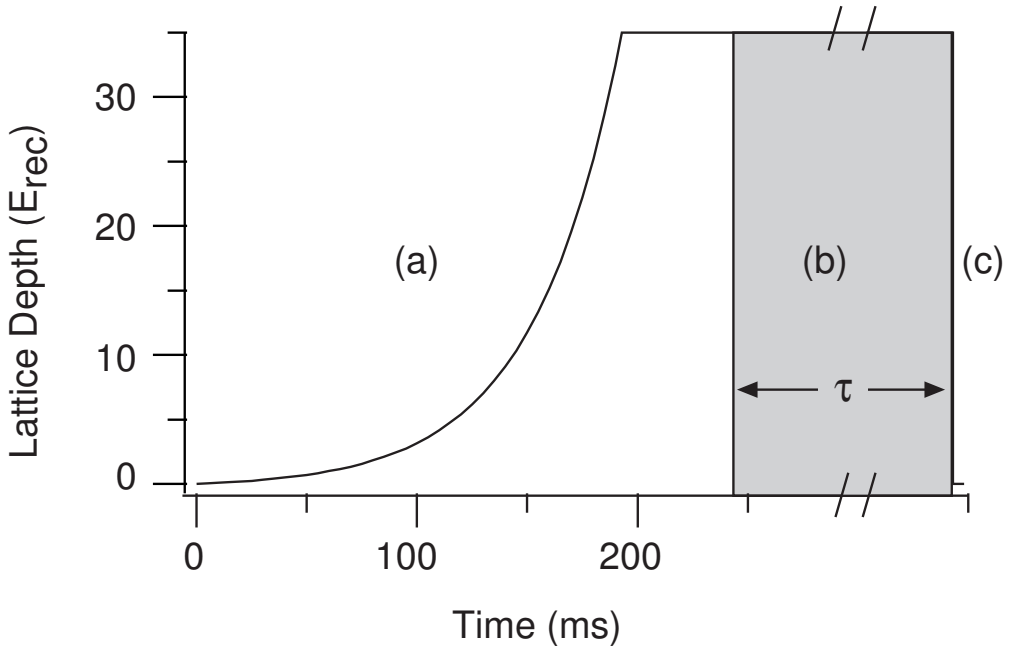

Figure 5-3: Diagram of the lattice depth vs time. (a) The lattice is ramped up to $U = 35E_{rec}$ in 193 ms, then held for 50 ms. The shape of the ramp is an exponential with a time constant of $\tau_{ramp} = 40$ ms. (b) The two photon pulse is applied for time τ, then (c) the atoms are released from the trap and imaged in 3 ms time of flight.

5.4.4 Detection

A single two-photon pulse resonant with the $|1, -1\rangle \rightarrow |2, 1\rangle$ transition was applied to the atoms in the lattice for some time τ, as depicted in Fig. 5.4.2. The pulse consisted of a microwave photon at 6.33 GHz and a RF photon at ≈1.6781 MHz. The microwave synthesizer was an Agilent E8257D running off its internal timebase. The RF synthesizer was an Agilent 33250a, and was synchronized to the 10 MHz timebase of the microwave synthesizer. Magnetic field dependent line shifting and broadening was avoided by working at a bias field of ∼3.23 Gauss, where the two states experience the same first order Zeeman shift. The effect of the magnetic field on the resonance frequency is shown in Fig. 5.4.4. The power of the pulse was adjusted to produce a π pulse for each hold time τ. Immediately after the pulse, the confining potentials were switched off and the atomic cloud was allowed to expand for 3 ms to reduce the column density. Atoms in the $|2, 1\rangle$ state were detected with absorption imaging using light resonant with the $F = 2 \rightarrow F' = 3$ transition.

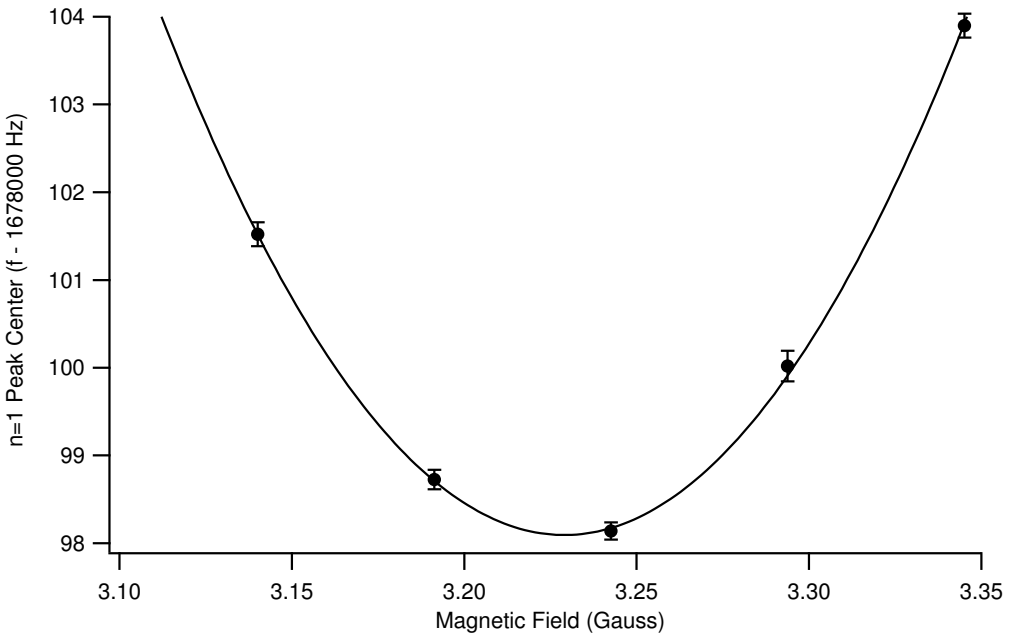

Figure 5-4: Resonance of the $n = 1$ peak vs magnetic field. The line is a fit to the parabolic field minimum. Determination of the resonance minimum to a level of 10 mG provided an uncertainty of 0.1 Hz in the frequency.

5.5 Results

5.5.1 Pulse Bandwidth Measurement

By using long measurement pulses, we narrowed the bandwidth of the scan and increased the resolution the $n = 1$ and $n = 2$ peaks from that reported in our previous work [6] (Fig. 5.5.1). Using a double Gaussian fit to the number of $F = 2$ atoms detected versus the RF frequency of the form $y = y_o + A_1 e^{-((x-x_1)/\sigma_1)^2} + A_2 e^{-((x-x_2)/\sigma_2)^2}$, the $n = 1$ peak was more than $10\sigma_2$ removed from the $n = 2$ peak. This indicated that any frequency shift from higher densities to the singly occupied sites was removed at a level better than 10^{-5}. Shifts from superfluid layers are assumed to be negligible for our experimental parameters [15], leaving only the $n > 2$ MI states to be considered as perturbations to the $n = 1$ sites. Thus by using the MI phase to separate density shifts into carrier and sideband peaks, we were able avoid density dependent shifts that affect other atomic clock experiments. By increasing the duration of the microwave pulse, and thus narrowing the bandwidth, we were

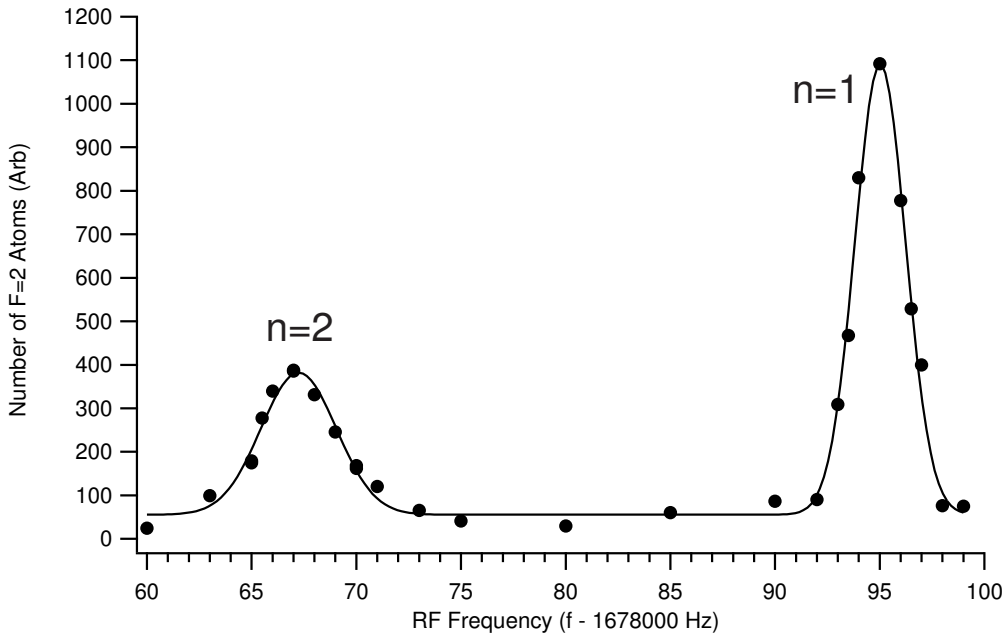

Figure 5-5: Microwave scan of atoms in the lattice. The $n = 2$ peak is centered at 1,678,067.2 $\pm$ 0.1 Hz with a FWHM of 4.2 $\pm$ 0.8 Hz, and the $n = 1$ peak is centered at 1,678,095.03 $\pm$ 0.03 Hz with a FWHM of 2.85 $\pm$ 0.08 Hz. The fit is a double Gaussian, and shows that the $n = 2$ peak is move than five linewidths removed from the $n = 1$ peak, eliminating the density shift. The lattice depth was a 35 E_{rec}, and the measurement time was 300 ms.

able to measure successively smaller linewidths of the singly occupied sites down to 1.0(2) Hz FWHM (Fig. 5.5.1). Measurement times longer than 1200 ms did not further decrease the observed width.

5.5.2 AC Stark Shift Cancellation

Since the $F = 1$ and $F = 2$ states have different complex polarizabilities, the interaction with the lattice light field will produce a frequency shift in the microwave resonance that is dependent on the lattice depth. In order to correct for this frequency shift induced by the ac Stark effect, the location of the $n = 1$ peak was measured for a variety of lattice depths in the MI regime. Since the ac Stark shift scales linearly with laser power, measuring the resonance as a function of lattice depth allowed us to quantify this effect. After a linear fit to the data (Fig. 5.5.3), extrapolation to a depth of 0 E_{rec} revealed the resonance frequency without any linear laser intensity

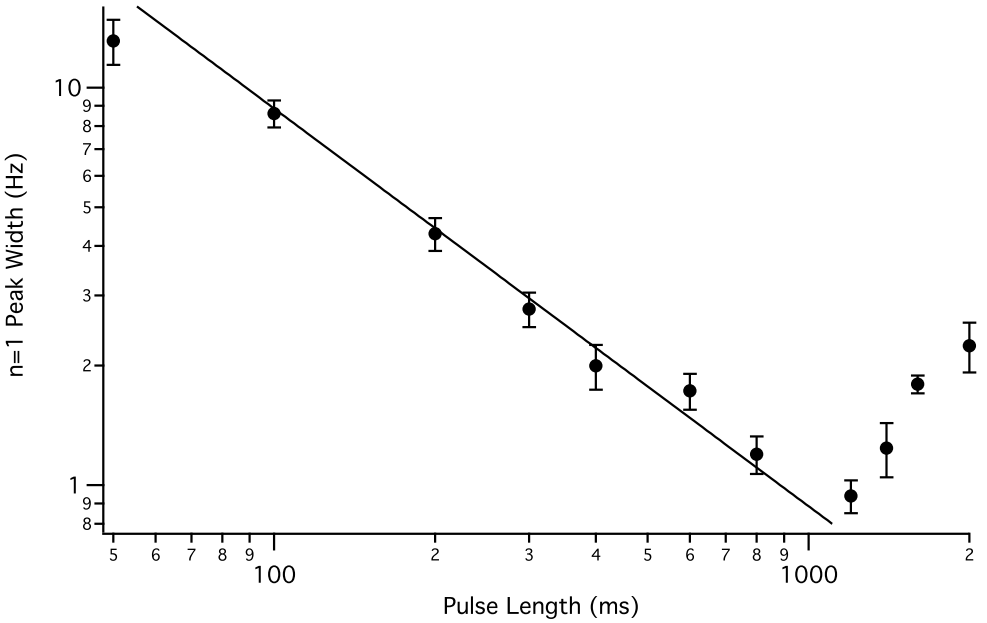

Figure 5-6: Width of the $n = 1$ peak vs. two photon pulse length. After careful lattice alignment and bias field calibration, the width of the single occupation density peak was measured as a function of the interrogation pulse length. The two photon intensity was adjusted to provide a π pulse at each hold time. The line represents the theoretical bandwidth of the pulse. Pulses longer than 1200 ms resulted in larger peak widths due to technical noise.

dependent shifts. This extrapolation increased the uncertainty of the measurement by about a factor of two over that of a typical single frequency measurement. The minimum lattice depth required to clearly resolve the $n = 1$ peak was 20 E_{rec}, and a maximum depth of 40 E_{rec} was used.

5.5.3 Absolute Frequency Measurement

After extrapolation, the $|1, -1\rangle \rightarrow |2, +1\rangle$ hyperfine transition frequency was measured to be 6,834,678,015.20(18) Hz (statistical). After applying a 4497.3 Hz correction predicted from the Breit-Rabi formula for the finite magnetic field [69], this is 98.4 Hz from the accepted value of 6,834,682,610.90434(3) Hz [59], but the focus of this work was only to control systematic errors resulting from inter-atomic interactions, not to make a high accuracy measurement. This discrepancy is explained in the analysis section as a result of drift of our microwave frequency source.

The relatively long experimental cycle time is another limiting factor in the ultimate precision. It takes approximately 10 data points to make an accurate determination of the line center, and each data point (BEC) takes up to 90 seconds to produce in our machine. 15 minutes is a long time in a laboratory environment with elevators, other experiments nearby, and even the subway possibly affecting each measurement [11]. Experiments designed to produce cold atoms clouds much more frequently would be better suited to make precision clock measurements.

5.6 Analysis

5.6.1 Pulse Bandwidth Limit

The primary determinant of the peak width was the bandwidth of the two-photon pulse. In the case of a bandwidth limited pulse, the lineshape should be a sinc squared with a FWHM of $0.8859/\tau$. This is shown as the solid line in Fig. 5.5.1, which agrees well with the data for $\tau < 1$ s. For times longer than 1 s, several sources of inhomogeneous broadening begin to affect the lineshape.

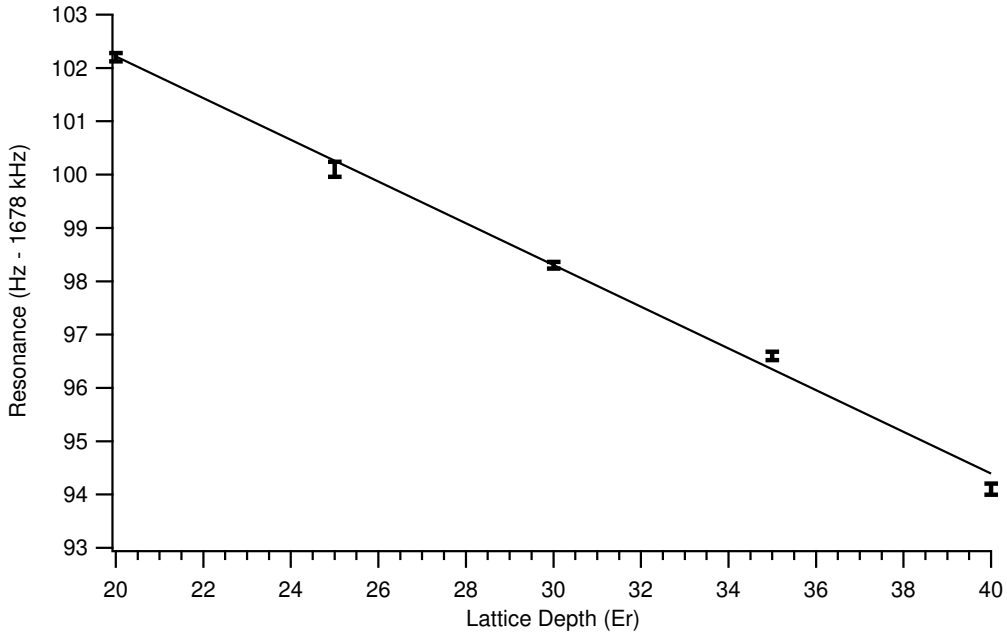

Figure 5-7: Center frequency of the $n = 1$ peak vs. lattice depth. The center of the single occupation peak was measured as a function of lattice depth in order to extrapolate to zero laser intensity. The line is a linear fit which gives a zero intercept of 110.04 $\pm$ 0.18 Hz, indicating an ac Stark shift free frequency of 6,834,678,110.04 $\pm$ 0.18 Hz. The error bars have a typical value of $\pm$0.10 Hz.

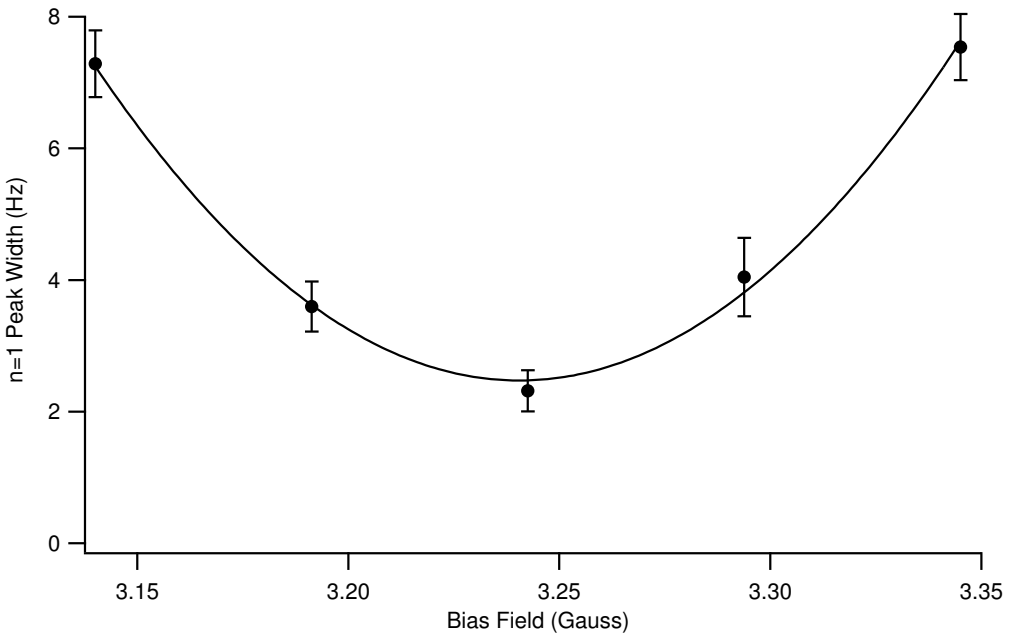

Figure 5-8: FWHM of the $n = 1$ peak vs magnetic field. Control of the magnetic field at a level of <20 mG was necessary to minimize inhomogeneous magnetic field broadening, and $\tau = 800$ ms was used for this data. The line is a parabolic fit to guide the eye.

5.6.2 Inhomogeneous Magnetic Field Broadening

The largest source of inhomogeneous broadening in our experiment is due to a magnetic field gradient across the atomic cloud. Our magnetic trap is operating at the low limit of holding the atoms against gravity, and thus we assume that the entire cloud lives in a constant vertical magnetic field gradient of 15 G/cm. Taking a $n = 1$ shell radius of 19 μm, we calculate a field variation of 58 mG vertically across the entire cloud, implying a broadening of the hyperfine transition of $\sim$0.36 Hz due to the inhomogeneous magnetic field. The effect of the magnetic bias field on the peak width is shown in Fig.5.6.2. Since the magnetic field broadening depends on the size of the atomic cloud, a large atom number could lead to larger linewidths. Within the statistical uncertainty of the fits, the width of the $n = 1$ peak was not found to be significantly sensitive to atom number in the range $10^5 < N < 10^6$.

5.6.3 Differential ac Stark Shift

Another source of inhomogeneous broadening is the differential ac Stark shift. If the clock measurement samples atoms which are trapped in regions of different laser intensity, the resonance will be broadened. However, the shell structure of the MI phase will tend to minimize effects from the differential ac Stark shift as all of the atoms in the measured shell live in approximately the same laser intensity. If the atomic cloud is small compared to the diameter of the lattice beams, this effect will also be small. Assuming that the measured atoms consist of a shell with radius equal to the Thomas-Fermi radius of the BEC, we calculate that the differential ac Stark shift across the shell results in a broadening of $<$0.2 Hz.

This broadening scales linearly with the inverse of the beam diameters, so narrow beams used for all optical trapping would adversely affect the measurement. For example, 20 μm waist beams would lead to a differential ac Stark shift broadened peak width of $\sim$2 Hz, dominating other sources of broadening currently observed. This broadening, as well as the total ac Stark shift may be reduced by the use of a "magic" wavelength lattice. By carefully choosing λ so that the two interrogated levels are shifted equally by the trapping laser, the ac Stark shift may be reduced by several orders of magnitude [73]. In the absence of a magic wavelength, a blue-detuned lattice laser could be used, trapping the atoms in regions of minimum laser intensity [5].

5.6.4 Particle-Hole Pair Broadening

One possible source of homogeneous broadening is the existence of particle-hole pairs within the $n = 1$ number state[22]. If we rewrite the Hamiltonian in the MI phase with the tunneling term as a perturbation to the interaction term, to first order we have [23]

$$|\Psi^{(1)}\rangle \approx |\Psi\rangle_{\mathrm{MI}} + \frac{J}{U}\sum_{\langle i,j\rangle}\hat{a}_i^\dagger\hat{a}_j|\Psi\rangle_{\mathrm{MI}}. \tag{5.8}$$

The tunneling term of the Hamiltonian acts as a perturbation on the otherwise uniform array of Fock states in the MI phase, adding a small superposition of $n = 0$

and $n = 2$ noise to the $n = 1$ signal. This manifests itself in our measurement as a small shift of the $n = 1$ peak towards $n = 2$ due to the slightly increased average density. At a lattice depth of 20 E_{rec}, a 3.5% mixture could generate a shift as large as 1.0 Hz. However, this effect scales as J/U, and for a lattice depth of 35 E_{rec}, the 0.2% mixture generates a shift of 0.05 Hz and would be further reduced for larger lattice depths. The measurement of center frequency versus lattice depth in Fig. 5.5.3 does not indicate any nonlinear effects at lower lattice depths, suggesting that particle-hole pair broadening plays a smaller role than the theory describes.

5.6.5 Induced Dipole-Dipole Interactions

Another systematic shift which depends on interactions is the induced dipole-dipole shift [8, 36], where the measurement electromagnetic field drives dipole oscillations in the atoms that affect neighboring lattice sites. Since the measurement wavelength ($\lambda_{\mu w} \approx$50 mm) is very long compared to the lattice spacing ($d = 523$ nm), there will be a dipole-dipole interaction in the near field regime. This interaction is given by [5]

$$V_{dd} = \frac{s\Gamma}{k_{meas}^3 d^3} \tag{5.9}$$

where s is the saturation parameter, Γ is the linewidth of the transition, k_{meas} is the wavenumber of the measurement field, and $d = \lambda_{lattice}/2$ is the spacing between atoms. However, the very narrow natural linewidth of the $|1, -1\rangle \rightarrow |2, 0\rangle$ transition ($\sim 10^{-8}$ Hz), as well as the relatively large single photon detuning (420 Hz) imply an interaction energy shift of < 0.02 Hz. Experiments using measurements in the optical regime will benefit from a reduced interaction since the energy shift scales as $(\lambda_{meas}/d)^3$ [36], and careful selection of the lattice geometry can even further suppress this effect [8].

5.6.6 Microwave Frequency Source

The main source of systematic error in this experiment was the microwave frequency source. Our synthesizer was not linked to any external reference clock, such as GPS,

and the specified drift rate of 4.5 ppb per day corresponded to 31 Hz per day at 6.8 GHz. Indeed, frequency jumps as large as 20 Hz over a two day period were observed when temperature stability in the lab was not maintained. Future experiments would certainly implement better master oscillator stabilization.

5.7 Two Photon Pulses

Using a two-pulse Ramsey technique was investigated, but phase jitter due to synthesizer frequency noise made accurate fitting of the resulting signal difficult. The use of a double pulse method is limited only by the fact that each of the two pulses must have a bandwidth narrow enough to not address any atoms in sites with occupation greater than one, and could improve the accuracy of future experiments. However, as the bandwidth of the pulse is increased, sites with higher than unity occupation will begin to affect the signal, and precision will be lost.

In one experiment, very short (5 ms) pulses were used. The bandwidth of these pulses was large enough (>150 Hz) to address all the atoms in the lattice. If the time between the pulses was varied (instead of the frequency), the resulting fringe pattern consisted of a beat note between the atoms in the $n = 1$, 2, and 3 sites.

5.8 Conclusion

In conclusion, we have implemented an atomic clock with an atomic cloud trapped in the MI phase of a 3D optical lattice. While our demonstration is not competitive with current, state-of-the-art atomic clocks, the density discretization technique shown here could be used to increase the precision of optical frequency Ca, Yb, or Sr clocks currently under development [49, 76, 77, 80, 31, 32].

Chapter 6

Conclusion

Looking back on my work here I feel satisfied that I tackled three extremely different projects and had at least some success with each. The hard disk platter project took well over a year, with many trials and tribulations. It was very much my baby from start to end, and while I take pride in what I was able to accomplish with it, I can only wish that the disk itself had been more cooperative. While it is indeed a significant improvement over many other atom chip implementations, it certainly wasn't the next-generation leap I had been hoping for.

The dressed Zeeman trap was almost a fling in comparison. Trying to accomplish the proof-of-principle project for almost zero dollars was a wonderful exercise in begging, borrowing, and stealing. I was in the middle of writing a computer program to control the synthesizer chip for the next phase of the experiment when we had some discussions as a group and decided that the possible scientific payoff wasn't great enough to delay the optical lattice project any longer. I still feel that it was the right decision, but it was definitely a fun project while it lasted, and achieving mid-term results almost an order of magnitude better than reported anywhere else didn't hurt.

The optical lattice clock was a great note on which to end the show. The machine was never really stable enough until after about 2 A.M., so I had plenty of time alone to meditate with the machine and contemplate my existence in the dark. It was also a full-bodied chance to make a precision measurement - well, at least precision compared to my other, even *more* proof of principle experiments.

An entirely new crew of students now runs the machine: Jongchul Mun, Patrick Medley, David Hucul, and soon post-doc David Weld. Hopefully not too many components will turn into mysterious black boxes, and I hope my contributions have been lasting ones.

Appendix A

Zeeman Slower Program

This appendix contains the source code for the program I used to design the Zeeman slower. The constants in the header must be modified to suit any particular new applications, and can be compiled in any ANSI C environment. It outputs several files, two of which are of particular importance. The file "field7.dat" describes the desired and theoretically created magnetic field profiles, and can be imported into Excel or any other spreadsheet program using a tab delimited format. The file "windings.dat" is text file which contains a drawing of the proposed slower cross section. This drawing is for use during the winding of the solenoid, and was used to produce the Zeeman slower used on our machine.

```
#include<math.h>
#include<stdio.h>
#include<stdlib.h>

/********** MATH CONSTANTS ***********/
#define PI 3.14159265358979
#define MU0 12.5663706144     /*  = 4xPI  gauss * mm / A */
#define CPI 2.54              /* cm per inch */

/* all lengths in mm */
/******** COIL PARAMETERS ************/
#define INSIDE_RADIUS 19.7    /* The radius of the innermost coil */
#define COIL_SPACING 3.5      /* The thickness of one loop */
#define MAX_SPACING 21.0      /* 5 turns in between windings maximum */
#define SPACING_INC 0.5       /* in units of wire diameters */
#define MAX_TURNS 345         /* Maxmimum current loops to use in simulation */
#define MAX_SOLENOIDS 45      /* Maxmimum solenoids to use in simulation */
#define CURRENT_1 5.0         /* Current (Amps) in solenoid 1 */
#define CURRENT_2 10.0
#define CURRENT_3 30.0
#define RATIO_1 0.98          /* Field taper percentage (empirical) */
#define RATIO_2 0.98
#define RATIO_3 0.98
#define LOW_C 15              /* Last loop of low current section (in memory)*/
#define MED_C 30              /* Last loop of medium current section (in memory)*/
#define HIGH_C 45             /* Last loop of high current section (in memory)*/
#define LOW_P 0.45            /* Percentage length of low current section (empirical) */
#define MED_P 0.3             /* Percentage length of medium current section */
#define SLOWER_START 150      /* Starting position of the slower in mm from the MOT center */
#define SLOWER_LENGTH 920     /* Length in mm of the total slower */
#define MAX_LENGTH 1200       /* Length in mm of physical simulation */
#define FIT_BUFFER 25         /* Sample range where the sim watches the B field from 1 coil */
```

```
/************************************/
/******** FIELD PARAMETERS **********/
/************************************/
#define Z_ZERO 200            /* Starting point of the B field that matters in the sim */
#define Z_ONE 1070            /* Ending point of the B field that matters */
#define B_BIAS 0.0            /* Amount of bias field to add (not used) */

/************************************/
/******** EXPERIMENTAL PARAMETERS ****/
/************************************/
#define A_MAX 0.6                                   /* acceleration safety factor */
#define FINAL_VELOCITY 20.0                         /* m/s */
#define ACCELERATION 112122.                        /* meters / sec^2 from photon recoil*/
#define BOHR_MAGNETON 1400000.0                     /* hertz per gauss */
#define WAVELENGTH 0.000000780                      /* meters */
#define GAUSSMS 1.0 / (BOHR_MAGNETON * WAVELENGTH)/* gauss per meter per second */
#define EPSILON 0.000001                            /* some small value */

/*****************************************************************/
/****************** FUNCTIONS ************************************/
/*****************************************************************/
void initialize(void);

void make_field(float *field);
void make_array_field(float *field);
void copy_field(float *target, float *source);
void fit_solenoids(void);
int  fit_solenoid(int a, float ratio);

void  add_dz_section(int radius, int pos, float spacing, float current, float *field);
void make_true_field(void);

float eval_accel(float *field);
float accel(int z, float *field);
float eval_b(float *field);
float getmax(int start, int end, float *field);
float getmin(int start, int end, float *field);
float min_delta_b(int start, int end, float *high, float *low);
float b_ratio(int start, int end, float *high, float *low, float bias);

void save_solenoids(char *filename);
void save_field(char *filename, float *field);
void save_solution(char *filename);
void draw_solenoid(char *filename);

float rndnum(void);

typedef struct {
     float current;
     float spacing[MAX_LENGTH];
     int layer;
     int start_z;
     int max_length;
     int length;
     } solenoid_type;

/*****************************************************************/
/****************** GLOBAL VARIABLES *****************************/
/*****************************************************************/
solenoid_type solenoid[MAX_SOLENOIDS];

float field[MAX_LENGTH];          /* The working copy of the B field */
float truefield[MAX_LENGTH];      /* The B field generated from scratch */
float desired[MAX_LENGTH];        /* The theoretical, desired field */
float bzero;
float winding[MAX_TURNS][MAX_SOLENOIDS+1];

int main() {

     initialize();                /* make desired field and define solenoid currents */
     fit_solenoids();
     save_solution("field7.dat");
     save_solenoids("solenoids.dat");
     save_field("field.dat",field);    /* Saves desired and actual fields, and error. */
     draw_solenoid("windings.dat");    /* Drawn solenoid winding pattern. */
}

/**************  FIT ALL SOLENOIDS TO THE FIELD  *****************/
void fit_solenoids(void) {

     int a;
     int b;
     int pause;
     int check;
     int lastlayer;

     check = 1;

     /*** FIT LOW CURRENT SOLENOIDS ***/
     for(a=0;a<LOW_C && check == 1;a++)  {
          solenoid[a].start_z = SLOWER_LENGTH * (1 - LOW_P) + SLOWER_START;
```

```
            solenoid[a].max_length = SLOWER_LENGTH * LOW_P;
            solenoid[a].layer = a;
            solenoid[a].current = CURRENT_1;
            solenoid[a].length = 0;
            check = fit_solenoid(a,RATIO_1);
            if(check) printf("Solenoid %d: Length: %d\n",a+1,solenoid[a].length);
            if(check == 2) printf("\tHigh End Trimmed.\n");
      }
      check = 1;

      /*** FIT MEDIUM CURRENT SOLENOIDS ***/
      for(a=LOW_C;a<MED_C && check == 1;a++) {
            solenoid[a].start_z = SLOWER_LENGTH * (1-(LOW_P+MED_P)) + SLOWER_START;
            solenoid[a].max_length = SLOWER_LENGTH * MED_P;
            solenoid[a].layer = a-LOW_C;
            solenoid[a].current = CURRENT_2;
            solenoid[a].length = 0;
            check = fit_solenoid(a,RATIO_2);
            if(check) printf("Solenoid %d: Length: %d\n",a+1,solenoid[a].length);
            if(check == 2) printf("\tHigh End Trimmed.\n");
      }
      check = 1;

      /*** FIT HIGH CURRENT SOLENOIDS ***/
      for(a=MED_C;a<MAX_SOLENOIDS && check == 1;a++) {
            solenoid[a].start_z = SLOWER_START;
            solenoid[a].max_length = SLOWER_LENGTH * (1-(MED_P+LOW_P));
            solenoid[a].layer = a-MED_C;
            solenoid[a].current = CURRENT_3;
            solenoid[a].length = 0;
            check = fit_solenoid(a,RATIO_3);
            if(check) printf("Solenoid %d: Length: %d\n",a+1,solenoid[a].length);
            if(check == 2) printf("\tHigh End Trimmed.\n");
      }
}

/*********************************************************************/
/*  FIT AN INDIVIDUAL SOLENOID TO THE DESIRED FIELD WITHIN GIVEN LIMITS */
/*********************************************************************/
int fit_solenoid(int a, float ratio) {

      int layer;
      int z;
      int modified;
      int buffer;
      int under_buffer;
      int pos;
      int beginning;

      float temp[MAX_LENGTH];
      float spacing;
      float current;
      float bratio;
      float limit;
      float crit_ratio;
      float radius;
      float bias;
      float delta[MAX_LENGTH];
      float temp_field[MAX_LENGTH];

      modified = 0;
      spacing = COIL_SPACING;
      current = solenoid[a].current;
      crit_ratio = 0.0;
      radius = solenoid[a].layer * COIL_SPACING + INSIDE_RADIUS;

      for(z=0;z<MAX_LENGTH;z++)  {
            temp_field[z] = 0.0;
            delta[z] = desired[z] - field[z];
      }

      for(z=0;(spacing < MAX_SPACING) && (z < solenoid[a].max_length);z++) {

            pos = solenoid[a].start_z+z;

            if(z < FIT_BUFFER)  {
                  if(a >= MED_C) {
                        buffer = FIT_BUFFER*2 - z;          /* try to fit max field */
                        under_buffer = FIT_BUFFER;
                  }
                  else
                        buffer = FIT_BUFFER;
                        under_buffer = FIT_BUFFER;
                        beginning = 1;
                  }
            else {
                  buffer = FIT_BUFFER;
                  under_buffer = FIT_BUFFER;
                  beginning = 0;
            }

            if(z + buffer > solenoid[a].max_length)     {
```

```
                buffer = solenoid[a].max_length - z;
            }

            bratio = b_ratio(pos-under_buffer, pos+buffer, delta, temp_field, 0.0);

            if((beginning) && (bratio >= 0.3) && (a < MED_C)) {
                modified = 2;
                break;
            }

            if(bratio >= 1.0) break;

            if(bratio > crit_ratio) {
                spacing = COIL_SPACING / pow(1.0-bratio, 0.5);
                crit_ratio = bratio;
            }

            if(spacing > MAX_SPACING) spacing = MAX_SPACING;

            add_dz_section(radius, solenoid[a].start_z + z, spacing, current, field);
            add_dz_section(radius, solenoid[a].start_z + z, spacing, current, temp_field);

            solenoid[a].spacing[z] = spacing;
            modified = 1;
        }

        if((modified) && (z >= 10)) {
            solenoid[a].length = z;
            for(;z<MAX_LENGTH;z++)
                solenoid[a].spacing[z] = 0.0;
            return(modified);
        }

        printf("(Some Solenoids Unused!)\n");
        solenoid[a].length = 0;
        solenoid[a].current = 0.0;
        return(0);
}


/*************************************************************************/
/* ADD THE FIELD FROM A TINY SOLENOID SECTION */
/*************************************************************************/
void add_dz_section(int radius, int pos, float spacing, float current, float *field) {

        int z;
        float junk;
        float rsq;
        float twospacing;

        rsq = radius * radius;
        junk = MU0 * current * rsq;
        twospacing = 2 * spacing;

        for(z=0;z<MAX_LENGTH;z++)
            field[z] += junk / (twospacing * pow(rsq + pow(z-pos,2),1.5));
}

/*************  MAKE THE WHOLE FIELD FROM SCRATCH  ***********************/
void make_true_field(void) {

        int a;
        int z;
        int pos;

        float radius;

        printf("Remaking field...\n");

        for(a=0;a<MAX_LENGTH;a++)
            truefield[a] = 0.0;

        for(a=0;a<MAX_SOLENOIDS;a++)
            if(solenoid[a].current > 0.0) {
                printf("\tAdding solenoid %d...\n",a+1);
                radius = solenoid[a].layer * COIL_SPACING + INSIDE_RADIUS;
                for(z=0;z<solenoid[a].length;z++)
                    if((solenoid[a].spacing > 0) && (solenoid[a].spacing[z] <= MAX_SPACING))
                        add_dz_section(radius, solenoid[a].start_z+z,
                                solenoid[a].spacing[z], solenoid[a].current, truefield);
            }
        printf("...done.\n");
}

/**********  FIND MAXIMUM RATIO BETWEEN DESIRED AND ACTUAL FIELDS  ************/
float b_ratio(int start, int end, float *high, float *low, float bias) {

        int z;
        float temp;
        float max;

        if(start < 0) start = 0;
```

```
      if(end > MAX_LENGTH) end = MAX_LENGTH;
      max = 0.0;

      for(z=start;z<end;z++) {
            if((high[z] - bias) == 0) continue;
            temp = (low[z]-bias) / (high[z]-bias);
            if(temp > max) max = temp;
      }
      return(max);
}

/********  FIND MAXIMUM DIFFERENCE BETWEEN DESIRED AND ACTUAL FIELDS  **********/
float min_delta_b(int start, int end, float *high, float *low) {

      int z;
      float temp;
      float min;

      if(start < 0) start = 0;
      if(end > MAX_LENGTH) end = MAX_LENGTH;
      min = 0.0;

      for(z=start;z<end;z++) {
            temp = high[z] - low[z];
            if(temp < min) min = temp;
      }
      if(min > 0) min = 0;
      return(min);
}

/********  GET MAXIMUM FIELD IN RANGE  ****************************/
float getmax(int start, int end, float *field) {

      int z;
      float temp;

      if(start < 0) start = 0;
      if(end > MAX_LENGTH) end = MAX_LENGTH;

      temp = field[start];
      for(z=start;z<end;z++)
            if(field[z] > temp) temp = field[z];
      return(temp);
}

/********  GET MINIMUM FIELD IN RANGE  ****************************/
float getmin(int start, int end, float *field) {

      int z;
      float temp;

      if(start < 0) start = 0;
      if(end > MAX_LENGTH) end = MAX_LENGTH;

      temp = field[start];
      for(z=start;z<end;z++)
            if(field[z] < temp) temp = field[z];
      return(temp);
}

/***********  EVALUATE THE CURRENT FIELD  ************************/
/* This function returns the Chi^2 error sum between the desired and actual fields. */
float eval_b(float *field)  {

      int z;
      float errorsq = 0.0;

      for(z=SLOWER_START;z<Z_ONE;z++)
            errorsq += pow(field[z]-desired[z],2)/100;
      return(errorsq);
}

/***********  EVALUATE THE ACCELERATION FIT  *******************/
float eval_accel(float *field) {

      float accl;
      int z;
      float temp;

      accl = 0;
      for(z=Z_ZERO;z<Z_ONE;z++)  {
            temp = accel(z,field);
            if(temp > ACCELERATION * A_MAX)
                  accl += pow(temp - ACCELERATION * A_MAX,2)/10000;
      }
      return(accl);
}

/*******  CALCULATE THE ACCELERATION AT ONE POINT  ************************/
float accel(int z,float *field) {
      return(1000.0 * WAVELENGTH * BOHR_MAGNETON * (field[z]-field[z+1]) * (bzero - field[z]));
}
```

```
/***************  COPY THE FIELD  ***********************************/
void copy_field(float *a, float *b)  {

     int i;

     for(i=0;i<MAX_LENGTH;i++)
          a[i] = b[i];
}

/******************  MAKE A RANDOM NUMBER 0 - 1  *************************/
float rndnum(void) {
     float r = RAND_MAX;
     return(rand() / r);
}

/*****************  INITIALIZE VARIABLES  *********************************/
void initialize(void) {

     int a;
     int b;

     /*********** MAKE DESIRED FIELD ****************************************/
     bzero = B_BIAS + GAUSSMS * sqrt(pow(FINAL_VELOCITY,2) +
             2 * ACCELERATION * A_MAX* (Z_ONE-Z_ZERO) / 1000);

     for(a=0;a<Z_ZERO;a++)
          desired[a] = bzero - GAUSSMS * abs(FINAL_VELOCITY);
     for(;a<Z_ONE;a++)
          desired[a] = bzero - GAUSSMS * sqrt(pow(FINAL_VELOCITY,2) +
                       2 * ACCELERATION * A_MAX * (a-Z_ZERO) / 1000);
     for(;a<MAX_LENGTH;a++)
          desired[a] = B_BIAS;
     /*****************************************************************/

     for(a=0;a<MAX_LENGTH;a++) {           /* initialize initial field */
          field[a] = 0.0;
          truefield[a] = 0.0;
     }

     for(a=0;a<MAX_SOLENOIDS;a++) {       /* fill solenoid data with defaults */
          solenoid[a].length = 0;
          solenoid[a].current = 0.0;
          for(b=0;b<MAX_LENGTH;b++)
               solenoid[a].spacing[b] = COIL_SPACING;
     }
}

/**************  SAVE SOLENOID CONFIGURATION  ************************/
void save_solenoids(char *filename) {

     int a;
     int b;
     int inc;

     FILE *outfile;

     outfile = fopen(filename,"w");
     fprintf(outfile,"%d\t%d\n",MAX_SOLENOIDS,MAX_LENGTH);
     for(a=0;a<MAX_SOLENOIDS;a++)  {
          inc = 9;
          fprintf(outfile,"%d\t%3.0f\t",solenoid[a].length, solenoid[a].current);
          for(b=0;b<solenoid[a].length;b++) {
               inc++;
               if(inc >= 10) {
                    fprintf(outfile,"%4.1f\t",solenoid[a].spacing[b]);
                    inc -= 10;
               }
          }
          fprintf(outfile,"\n");
     }
     fclose(outfile);
}

/**************  SAVE ANY FIELD  ***********************************/
void save_field(char *filename, float *temp_field) {

     int a;
     FILE *outfile;

     outfile = fopen(filename,"w");
     fprintf(outfile,"%d\t%8.2f\n",MAX_LENGTH,bzero);
     for(a=0;a<MAX_LENGTH;a++)
          fprintf(outfile,"%f\n",temp_field[a]);
     fclose(outfile);
}

/***************  SAVE THE GENERAL SOLUTION  **********************/
void save_solution(char *filename) {

     int a;
     FILE *outfile;
```

```
      outfile = fopen(filename,"w");
      fprintf(outfile,"z\tfield\tdesired\tdeltab\ttruefield\tacceleration\teval_accel\n");
      for(a=0;a<MAX_LENGTH;a++)
            fprintf(outfile,"%d\t%f\t%f\t%f\t%f\t%f\n",
                  a,field[a],desired[a],truefield[a],field[a]-desired[a],
                  accel(a,field),ACCELERATION);

      fclose(outfile);

      save_field("desired_field.dat",desired);
}

/**************  DRAW THE SOLENOID STRUCTURE ******************************/
void draw_solenoid(char *filename) {

      int a;
      int z;
      float curr;
      float pos;
      float inc;

      FILE *outfile;

      outfile = fopen(filename, "w");
      curr = CURRENT_1;
      fprintf(outfile,"%5.2f\n",solenoid[0].current);

      for(a=0;a<MAX_SOLENOIDS;a++)  {
            if(solenoid[a].current > 0.0)  {
                  pos = 1.0 / solenoid[a].spacing[0];
                  inc = 0;
                  if(curr != solenoid[a].current) {
                        fprintf(outfile,"C%5.2f\n",solenoid[a].current);
                        curr = solenoid[a].current;
                  }

                  fprintf(outfile,"O");
                  for(z=0;z<solenoid[a].length;z++)  {
                        pos += 1.0 / solenoid[a].spacing[z];
                        if(inc >= COIL_SPACING) {
                              inc -= COIL_SPACING;
                              if(pos >= 1.0) {
                                    fprintf(outfile,"O");
                                    pos--;
                              }
                              else  {
                                    fprintf(outfile," ");
                              }
                        }
                        inc++;
                  }
                  fprintf(outfile,"\n");
            }
      }
      fclose(outfile);
}
```

Appendix B

The Onset of Matter-Wave Amplification in a Superradiant Bose-Einstein Condensate

This appendix contains a reprint of Ref. [62]: Dominik Schneble, Yoshio Torii, Micah Boyd, Erik W. Streed, David E. Pritchard, and Wolfgang Ketterle, *The Onset of Matter-Wave Amplification in a Superradiant Bose-Einstein Condensate*, Science **300**, 475 (2003). While not discussed in detail in this thesis, this was one of the first experiments performed on the the rubidium BEC machine.

The Onset of Matter-Wave Amplification in a Superradiant Bose-Einstein Condensate

Dominik Schneble,* Yoshio Torii,† Micah Boyd, Erik W. Streed, David E. Pritchard, Wolfgang Ketterle

The interaction of short and strong laser pulses with an atomic Bose-Einstein condensate is found to generate patterns of recoiling atoms that are different from those seen in previous light-scattering experiments. This phenomenon can only be explained by optical stimulation, showing that the previous description of superradiance as atomic stimulation is incomplete and that matter-wave amplification in Bose-Einstein condensates is suppressed at short times. Our experiments clarify the nature of bosonic stimulation in the four-wave mixing of light and atoms.

Superradiance is the collective emission of light from an ensemble of excited atoms and involves the spontaneous buildup of coherence in a macroscopic ensemble of atoms. Dicke, in his seminal work (*1*), showed that the spontaneous emission of photons from an ensemble of N localized atoms is enhanced by a factor of N over the single-atom emission rate when the atoms are in a cooperative state with all the transition moments in phase. If, however, the atomic ensemble extends over more than the wavelength of the radiation, the situation becomes more complex. Superradiant emission is then only possible along certain directions where a phase-matching condition is fulfilled. Furthermore, there are now two physically distinct pictures of the collective emission process in which the distinction between spontaneous emission and stimulated emission is blurred (*2*). In the viewpoint introduced by Dicke, the entire extended ensemble interacts with empty modes of the electromagnetic field, and all photons are emitted spontaneously, albeit in a cooperative way. In the other picture, some atoms emit spontaneously, and this radiation stimulates other atoms to emit in phase. The equivalence of these two pictures emphasizes that, if a system emits many photons cooperatively, a strict distinction between spontaneous and stimulated emission is no longer possible. The phenomenon of superradiance thus deepens and clarifies our understanding of the interaction of matter and light.

Because of their coherent nature, Bose-Einstein condensates readily exhibit collective superradiant behavior. Controversy regarding the role of quantum statistics in superradiance was resolved in (*3*, *4*) in which it was shown that processes attributed to bosonic stimulation can also be expected in superradiant Fermi systems. An important application of superradiance has been the coherent amplification of matter waves (*5*, *6*). We study superradiance in the short-pulse limit and show that amplification is attenuated at short times, leading to a more profound understanding of matter-wave amplification.

When a Bose-Einstein condensate is illuminated by a single laser beam (pump beam), light can be scattered into an empty mode. The condensate at rest, "dressed" by the pump beam, corresponds to the excited electronic state in the usual superradiance. Spontaneous emission is now replaced by a spontaneous Rayleigh scattering process that leads to a recoiling atom. This atom interferes with the atoms at rest and creates a periodic density modulation that, in turn, leads to an increase of the scattering rate, thus amplifying itself. Because the square of the density modulation is proportional to the number of recoiling atoms, one can describe this process as matter-wave amplification due to bosonic stimulation by atoms (*5*–*7*). Here, superradiance corresponds to the diffraction of the pump beam from a matter-wave grating in the condensate volume. In an elongated condensate, the gain is strongest when the photons leave the condensate along its long axis in the so-called endfire mode (*1*), whereas the atoms recoil at an angle of 45° with respect to the axis and emerge as a distinct atomic cloud (forward peak) with a momentum component parallel to the pump beam. The theoretical literature on superradiant scattering in condensates (*5*, *7*–*12*) corroborates this description, but here we show that it is incomplete.

Our new experimental results suggest an alternative picture for superradiance in which the endfire beam and the pump beam form an optical standing wave and diffract atoms in a stimulated scattering process between momentum states. The ambiguity between spontaneous and stimulated emission now reappears as the ambiguity of whether light is diffracted from a matter-wave grating or whether atoms are diffracted from a light grating. In the latter picture, the forward peaks in superradiance correspond to Bragg diffraction of atoms (*13*, *14*). In the present work, we observed the diffraction of atoms into additional states with momentum components antiparallel to the pump beam (backward peaks). This is possible in the regime of short pulses in which several recoil states are quasi-degenerate [Kapitza-Dirac diffraction (*15*, *16*)]. The backward peaks result from the reabsorption of spontaneously scattered photons and stimulated emission back into the pump beam. This off-resonant process, which cannot be described by the Dicke picture of collective spontaneous emission, both limits the growth of the endfire mode and suppresses matter-wave amplification by destructive interference.

The experiments discussed here were performed with a ^{87}Rb condensate in the $|F = 1, m_F = -1\rangle$ hyperfine ground state, where F and m_F are the quantum numbers for the total spin and its z component, respectively. We collected 10^{10} atoms in a magneto-optical trap from a slow atomic beam with a flux of 10^{11} s^{-1}. The atoms were cooled further in dark optical molasses and evaporatively cooled in a cloverleaf-type Ioffe-Pritchard magnetic trap. The trapped, almost-pure condensates contained about two million atoms and had Thomas-Fermi radii of 100 μm and 7.5 μm along the axial and radial directions, respectively. To induce superradiant scattering, we illuminated the condensate with an off-resonant pump laser beam (center intensity of 63 m W cm^{-2} and e^{-2} radius of 1.6 mm) for a variable pulse duration τ. The linearly polarized beam was incident horizontally along a radial direction with its electric field vector perpendicular to the axial direction (compare Figs. 1 and 2A). Immediately after applying the laser pulse, the atomic momentum distribution was analyzed by switching off the magnetic trap and imaging the atomic ensemble after 30 ms of ballistic expansion. Absorption images were obtained with the use of a vertical probe beam after the atoms had been optically pumped into the $F = 2$ ground state (Fig. 1). In case A for short pulses, the Rayleigh scattering rate Γ_{sc} was chosen to be comparable to the single-photon recoil frequency $\omega_r = 2.4 \times 10^4$ s^{-1} so that a large fraction of condensate atoms were scattered on a time scale that was short compared to the recoil time $\omega_r^{-1} = 42$ μs. In this case, we observed a nearly symmetric, X-shaped pattern. For comparison, when the detuning was chosen to be one order of magnitude larger (case B), the pattern evolved on

Massachusetts Institute of Technology–Harvard Center for Ultracold Atoms, Research Laboratory of Electronics and Department of Physics, Massachusetts Institute of Technology, Cambridge, MA 02139, USA.

*To whom correspondence should be addressed. E-mail: schneble@mit.edu

†Present address: Department of Physics, University of Tokyo, 3-8-1 Komaba, Meguro-Ku, Tokyo, Japan.

a time scale that was one order of magnitude above the recoil time, and the familiar superradiant scattering fan appeared, as in (*8*).

The scattering processes that give rise to the observed symmetric pattern are illustrated in Fig. 2A. In lowest order, forward peaks [label (1)] are generated when a pump photon with momentum $\hbar\mathbf{k}$ is scattered off a condensate atom (zero momentum), thereby producing a scattered photon with momentum $\hbar(\mathbf{k} - \mathbf{q})$ and a recoiling atom with momentum $\hbar\mathbf{q}$, $q = \sqrt{2}\,k$. In contrast, backward peaks [label (2)] are produced when a previously scattered photon is scattered back into the pump mode, thereby transferring a condensate atom into a recoiling atom with momentum $-\hbar\mathbf{q}$. Whereas in the first case energy is conserved, the energy mismatch in the latter case is twice the recoil energy, $\Delta E = 4\hbar\omega_r$. Therefore this process can only take place as long as the energy uncertainty $\hbar/\tau > \Delta E$, that is, for pulse lengths τ up to ~10 μs. At an early stage, when the endfire modes do not yet dominate completely, one can clearly recognize the dipole pattern of spontaneous photon emission (Fig. 2B) as a halo of recoiling atoms with radius $\hbar k$ on the right-hand side of the condensate. In addition, one also observes another halo on the left-hand side. This halo results from stimulated scattering of the spontaneously emitted photons back into the pump laser beam.

It is important to notice the slight left-right asymmetry of the X-shaped scattering pattern of Fig. 1A. There exist two endfire modes, q_+ and q_-, propagating in opposite directions due to the axial symmetry of the condensate, and therefore both the backward and forward peaks are grouped in pairs. However, the separation of the backward peaks in the axial direction is larger than that of the forward peaks. This suggests that the scattering processes for each of the two endfire modes occur near the edges of the condensate (Fig. 2C) (*17*).

This observation allows one to distinguish the two simple pictures in which light is diffracted from atoms or atoms are diffracted from light. The fact that the scattering process is strongest near the edges of the condensate suggests that atoms are diffracted from an optical standing wave formed by the pump and endfire modes: The intensity of the endfire modes and thus the intensity of the standing wave are highest near the edges of the condensate. Conversely, if the scattering processes could simply be described by diffraction of light from a matter-wave grating, one would expect the recoiling atoms to originate in the center where the atomic density and the diffraction efficiency of the grating are highest. This is indeed the case in the long-pulse limit where the Thomas-Fermi profile of the condensate shows depletion in the center (inset of Fig. 1B).

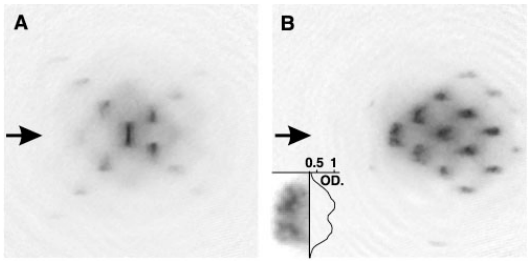

Fig. 1. Superradiant scattering of a laser beam (arrow) from a Bose-Einstein condensate in the short-pulse (**A**) and long-pulse (**B**) limit. Absorption images of the atomic density distribution were taken after 30 ms of ballistic expansion. In case A, Δ was −420 MHz and τ was 6 μs. In case B, Δ was −4400 MHz and τ was 800 μs. The inset in (B) is a magnification of the region around the condensate showing depletion of its center; for better visibility the contrast has been enhanced by a factor of 1.5. Also shown is a profile of the average optical density in the center region. The field of view of both images is 2.0 mm by 2.0 mm, and that of the inset is 120 μm by 270 μm.

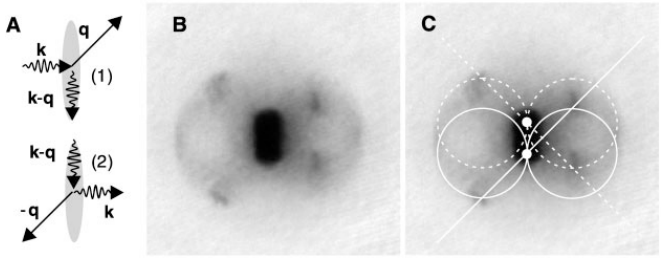

Fig. 2. Scattering processes (**A**) and scattering pattern (**B**) for a short (τ = 3 μs) light pulse. The circles and lines in (**C**) illustrate the origin of the dipole emission halos and the Kapitza-Dirac diffraction orders.

A more detailed analysis of the observed recoil patterns confirms the picture of optical diffraction. For short times $\omega_r\tau \ll 1$, one can neglect the frequency difference between the pump light ($+y$ direction) and the endfire modes ($\pm z$ direction), and their interference leads to a modulated light intensity

$$I_{\mathrm{mod}} = 2E_kE_{k-q_+}\cos k(y+z) + 2E_kE_{k-q_-}\cos k(y-z) + E_{k-q_+}E_{k-q_-}\cos 2kz \quad (1)$$

where E_{k-q+} and E_{k-q-} are the field amplitudes of the two endfire modes with wavevectors $k - q_+$ and $k - q_-$, respectively, and E_k is the amplitude of the pump beam. The first and second terms give rise to diffraction of atoms into momenta $\hbar q_n = n\sqrt{2}\,\hbar k$ along axes tilted at ±45° with respect to the long axis, with populations (*15*)

$$P_n = J_n^2(\Omega_{2R}\tau),\ n = 0, \pm1, \pm2, \ldots \quad (2)$$

Here the J_n are Bessel functions of the first kind; $\Omega_{2R} = \omega_{R,k}\,\omega_{R,k-q_i}/2\Delta$ is the two-photon Rabi frequency, given by the Rabi frequencies $\omega_{R,k}$ and $\omega_{R,k-q_i}$ ($i = +, -$) of the laser beam and the two endfire modes; and Δ is the detuning of the beams. Scattering processes that involve more than one endfire mode (such as those induced by the third term in Eq. 1) can be neglected as long as the endfire mode intensities are smaller than the intensity of the pump mode.

With the use of this model, we can determine the intensity of the individual endfire modes. Above 5 μs, the population in the minus-second-order peak exceeds 50% of that in the minus-first-order peak. At 6 μs, the ratio is 63%, which implies a two-photon Rabi frequency $\Omega_{2R} = 3.9 \times 10^5\ \mathrm{s}^{-1}$ corresponding to an endfire-mode intensity of 0.8 m W cm^{-2}. This intensity is more than two orders of magnitude larger than the intensity of spontaneous Rayleigh scattering into this mode (*18*).

A comparison of an extracted pattern to a calculated Kapitza-Dirac pattern is given in Fig. 3B. There is good general agreement; however, a major discrepancy exists for the zeroth order, that is, for the condensate itself. The depletion of the condensate is far less than predicted by the model. This is easily explained by the fact that the scattering processes take place mainly near the edges, leaving many condensate atoms in the central region. The model assumes an external endfire laser beam, whereas the endfire mode is produced in the condensate volume itself. Another discrepancy appears at longer times when τ approaches the two-photon recoil time: The resonant first-order peak $p_1 = \sqrt{2}\,\hbar k$ becomes dominant. The emergence of this asymmetry is a clear signature for the transition from the Kapitza-Dirac to the Bragg regime, that is, for the onset of energy conservation.

Before discussing the interplay between optical and atomic stimulation in our short-pulse experiment, we want to emphasize the qualitative equivalence of these two pictures in the long-pulse limit. The superradiant gain has been successfully interpreted as matter-wave stimulation (*7*, *8*), that is, as the diffraction of photons from a self-amplifying matter-wave grating. However, by extrapolating the observed short-time behavior to longer times, a purely optical interpretation of superradiance emerges: The endfire modes and the pump beam form a standing light wave from which the atoms can diffract. For $\omega_r\tau \gg 1$, the stimulated backscattering of endfire mode photons into the pump beam is energetically suppressed, the endfire mode grows exponentially in time, and so does the diffraction efficiency of the standing light wave. In this interpretation, superradiance in the long-pulse limit is nothing but (self-stimulated) Bragg scattering.

The equivalence of the two descriptions in the long-pulse limit can be obtained in a more quantitative way by considering the rate for Bragg scattering from the standing light wave formed by the pump beam and an endfire mode (neglecting propagation effects) (*7*):

$$W_B = N\Omega_{2R}^2/\Gamma_2 \qquad (3)$$

Here N is the number of atoms in the condensate, and Γ_2 is the width of the Bragg resonance (*19*). The Rabi frequency of the pump beam can be expressed through its Rayleigh scattering rate Γ_{sc} as $\omega_{R,k} = 2\Delta(\Gamma_{sc}/\Gamma)^{1/2}$, where Γ is the natural linewidth. The number of photons scattered in the coherence time $1/\Gamma_2$ is identical to the number of recoiling atoms N_q inside the condensate volume. This gives the Rabi frequency of the endfire mode as $\omega_{R,k-q} = \Gamma[N_q\Gamma_2\hbar\omega/(2I_sA)]^{1/2}$, where $I_s = \pi\hbar\omega\Gamma/3\lambda^2$ is the saturation intensity and A is the cross-sectional area of the condensate (λ is the wavelength, and ω is the frequency of the transition). The result

$$W_B = \Gamma_{SC}\frac{3}{2\pi}\frac{\lambda^2}{A}NN_q \equiv GN_q \qquad (4)$$

is, up to a numerical factor, identical to the result for the superradiant gain coefficient G obtained in (*8*), in which the interference term NN_q was interpreted as the modulation depth of the matter-wave grating from which the pump photons diffract.

This equivalence between optical and atomic stimulation was not properly recognized in earlier treatments (*7*, *8*) that were based on the argument that the number of photons in the condensate volume was smaller than one. However, as already pointed out in (*7*), the relevant photons (and recoiling atoms) are all those produced within the coherence time $1/\Gamma_2$. Although for the atoms the relevant mode volume is given by the condensate itself, it is much bigger for the scattered photons because the coherence length of the endfire mode greatly exceeds the length of the condensate. The fact that photons and recoiling atoms are produced in pairs implies that their effective numbers are equal and that atomic stimulation in one picture can be replaced by optical stimulation in another picture.

We now apply these concepts to the short-pulse limit. At early times τ, the scattering pattern is symmetric, and therefore the creation of endfire-mode photons (positive orders or forward peaks) is as probable as their absorption (negative orders or backward peaks), resulting in a fully suppressed superradiant gain. Spontaneous Rayleigh scattering is only amplified at longer times when the pattern develops an asymmetry. We describe this by attributing a Lorentzian lineshape with a linewidth $\Gamma \propto 1/\tau$ to the first and minus-first order (neglecting coherences). The former is resonant, and the latter is detuned by the two-photon recoil shift $\delta = \Delta E/\hbar$. This model predicts a suppression of the gain by a factor of $(2\delta/\Gamma)^{-2} \propto (\delta\tau)^{-2}$. With the use of a coherent model based on driven two-level systems, we find a suppression by a factor of $12(\delta\tau)^{-2}$, which has the same quadratic time dependence. The suppression of the gain at short times can also be understood in a purely atomic picture. An optical standing wave creates a phase grating in the atomic cloud, which transforms into a density grating only after the inverse recoil frequency, that is, the time it takes the atoms to move half a wavelength. For a given number of recoiling atoms, the atomic gain is initially zero and grows as $(\delta\tau)^2$, in agreement with the picture of optical amplification. It is the matter wave grating that gets amplified, rather than the number of recoiling atoms itself: The density grating created by the population N_q destructively interferes with the population N_{-q} in the backward peak, and the gain is reduced.

Although all three models are qualitative, they consistently predict a suppression of the gain by around two orders of magnitude for pulse lengths around 1 μs. For the typical condensate geometry in (*8*) and the present experiment, the ratio of G as defined in Eq. 4 to Γ_{sc} is about 4×10^3. At $\tau \approx 1$ μs, we expect an (attenuated) gain coefficient $G \sim 10^6\ s^{-1}$ for $\Gamma_{sc} \approx \omega_r$. The observed magnitude for the endfire-mode intensity is consistent with such a low gain. The attenuation is also evident when the scattering rate for the first order, $N_q \sim 10^{10}\ s^{-1}$, is compared to the global Rayleigh scattering rate of the pump beam. In the short-pulse limit, it is of the same order, whereas in the long-pulse limit an enhancement of one order of magnitude was observed (*8*).

This new physical picture of superradiance at short times can be applied to the atom amplifier (*5*, *6*) where a condensate illuminated by a pump beam is seeded with $N_q(0)$ recoiling atoms, resulting in a density grating. This grating diffracts the pump light into the endfire mode. At early times, the density modulation is not amplified because the number of atoms added to mode q is accompanied by an equal number in mode $-q$, and the two additional matter-wave gratings interfere destructively. Therefore, the gain equation is $\dot{N}_q(t) = GN_q(0)$, which implies linear growth. Exponential growth only starts after the inverse recoil frequency, when the atoms in mode $-q$ have disappeared because of energy conservation.

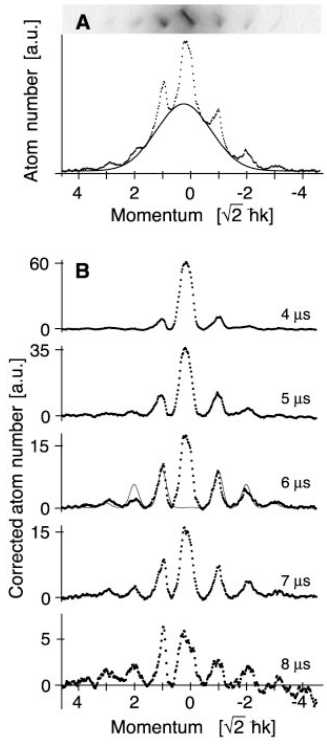

Fig. 3. Comparison of superradiant scattering in the short-pulse regime with Kapitza-Dirac diffraction. (**A**) The atom numbers in the image of Fig. 1A were integrated over a thin strip that contains the condensate and the diffraction orders. The strip is oriented along the direction from the bottom right to the top left of the image in Fig. 1A. The solid curve is a Gaussian representing the broad background of incoherently scattered and residual thermal atoms. a.u., arbitrary units. (**B**) Diffraction patterns for pulse durations τ between 4 and 8 μs. These patterns were obtained by subtracting the background from images similar to those in Fig. 1A. At 6 μs, the corresponding Kapitza-Dirac pattern for a standing light wave formed by two crossed laser beams with a Ω_{2R} of $3.9 \times 10^5\ s^{-1}$ is shown as a solid line. The widths of the peaks (approximated by Gaussians) were chosen to fit the minus-first-order peak.

In conclusion, by exploring the short-pulse limit of superradiant Rayleigh scattering, we have observed a previously unknown phenomenon in the scattering of a single laser beam by atoms: self-stimulated Kapitza-Dirac diffraction. The symmetry of the diffraction pattern implies a reduced gain for both atom and light amplification at early times. This realizes a novel regime of superradiance in which the atomic system has three almost equally spaced levels with all of the initial population in the middle one. This system has allowed us to illustrate important concepts of stimulation and superradiance. In the Dicke picture, all photons are emitted spontaneously and simply leave the system. However, we directly observed stimulation by and absorption of these photons in the form of Kapitza-Dirac scattering, and therefore the Dicke picture is incomplete for the short-pulse regime. None of the theoretical descriptions of superradiance in Bose-Einstein condensate (*5*, *7*–*12*) included transitions to momentum states that appear as negative orders in Kapitza-Dirac scattering.

Extrapolating our observations of Kapitza-Dirac scattering to longer pulses establishes the equivalence of self-stimulated Bragg diffraction and matter-wave amplification. There is a widespread opinion that bosonic stimulation is a purely quantum-statistical effect based on symmetry, whereas (*3*, *4*) showed that bosonically enhanced scattering can always be traced back to enhanced fluctuations. Here we have directly shown how photons mediate an effective interaction between the atoms that, after elimination of the photon field, results in bosonic stimulation of atoms. However, at early times, the "stimulating effect" of the population in mode q interferes destructively with the effect of atoms in mode $-q$ and the basic concept of bosonic stimulation by atoms fails, whereas a simple picture of optical stimulation provides the correct answer (*20*).

References and Notes

1. R. H. Dicke, *Phys. Rev.* **93**, 99 (1954).
2. M. Gross, S. Haroche, *Phys. Rep.* **93**, 301 (1982).
3. W. Ketterle, S. Inouye, *Phys. Rev. Lett.* **86**, 4203 (2001).
4. M. G. Moore, P. Meystre, *Phys. Rev. Lett.* **86**, 4199 (2001).
5. S. Inouye *et al.*, *Nature* **402**, 641 (1999).
6. M. Kozuma *et al.*, *Science* **286**, 2309 (1999).
7. W. Ketterle, S. Inouye, in *Bose-Einstein Condensates and Atom Lasers*, A. Aspect, J. Dalibard, Eds., vol. IV of *Comptes Rendus de l'Académie des Sciences Paris* (Elsevier, Paris, 2001), pp. 339–380.
8. S. Inouye *et al.*, *Science* **285**, 571 (1999).
9. M. G. Moore, P. Meystre, *Phys. Rev. Lett.* **83**, 5202 (1999).
10. Ö. E. Müstecaplioglu, L. You, *Phys. Rev. A* **62**, 063615 (2000).
11. N. Piovella, R. Bonifacio, B. W. J. McNeil, G. R. M. Robb, *Opt. Commun.* **187**, 165 (2001).
12. E. D. Trifonov, *J. Exp. Theor. Phys.* **93**, 969 (2001) [translation from E. D. Trifonov, *Zh. Eksp. Teor. Fiz.* **120**, 1117 (2001)].
13. P. J. Martin, B. G. Oldaker, A. H. Miklich, D. E. Pritchard, *Phys. Rev. Lett.* **60**, 515 (1988).
14. M. Kozuma *et al.*, *Phys. Rev. Lett.* **82**, 871 (1999).
15. P. L. Gould, G. A. Ruff, D. E. Pritchard, *Phys. Rev. Lett.* **56**, 827 (1986).
16. Y. B. Ovchinnikov *et al.*, *Phys. Rev. Lett.* **83**, 284 (1999).
17. For the 30-ms time of flight, the condensate expands by only 10% in the axial direction, as compared to more than a factor of 15 in the radial direction.
18. The fractional solid angle subtended by the condensate is $\Omega \sim (d^2/L^2)/4\pi$, where d is its diameter and L its length. The contribution of spontaneous Rayleigh scattering to the endfire mode intensity thus is on the order of $\Omega \times (N\Gamma_{sc}\hbar\omega) \times 1/d^2 = 2.5 \times 10^{-3}$ m W cm^{-2}.
19. J. Stenger *et al.*, *Phys. Rev. Lett.* **82**, 4569 (1999).

20. We would like to thank G. Campbell, A. Leanhardt, and J. Steinhauer for a critical reading of the manuscript and P. Meystre and S. Inouye for discussions. This work was supported by NSF.

7 February 2003; accepted 18 March 2003
Published online 27 March 2003;
10.1126/science.1083171
Include this information when citing this paper.

Mantle Fault Zone Beneath Kilauea Volcano, Hawaii

Cecily J. Wolfe,[1]* Paul G. Okubo,[2] Peter M. Shearer[3]

Relocations and focal mechanism analyses of deep earthquakes (≥13 kilometers) at Kilauea volcano demonstrate that seismicity is focused on an active fault zone at 30-kilometer depth, with seaward slip on a low-angle plane, and other smaller, distinct fault zones. The earthquakes we have analyzed predominantly reflect tectonic faulting in the brittle lithosphere rather than magma movement associated with volcanic activity. The tectonic earthquakes may be induced on preexisting faults by stresses of magmatic origin, although background stresses from volcano loading and lithospheric flexure may also contribute.

Earthquake characteristics at the active Kilauea volcano have long been used to construct models of this shield volcano and to constrain the structure of its magmatic system (*1*–*4*). Based on hypocenters in the catalog of the U.S. Geological Survey Hawaiian Volcano Observatory (HVO) seismic network, it has been suggested that the earthquakes at Kilauea outline a pipe-like magma conduit that extends through the lithosphere to depths as great as 60 km (*1*–*4*), thereby delineating the magma pathway from its source to the surface. However, the accuracy of routinely determined hypocenters is limited by factors including the network geometry, the available arrival time picks, picking errors, and the presence of three-dimensional velocity heterogeneity. Thus, relocations of earthquakes, using relative location methods, which reduce the effects of velocity heterogeneity, combined with precise cross-correlation measurements, have produced more accurate locations (*5*–*11*) and delineated fault structures. Here, we present relocations of deep earthquakes, focusing on distinguishing magmatic versus tectonic events to understand how the growing volcano affects the crust and upper mantle.

[1]Hawaii Institute of Geophysics and Planetology, University of Hawaii at Manoa, Honolulu, HI 96822, USA. [2]Hawaiian Volcano Observatory, U.S. Geological Survey, Hawaii National Park, HI 96718, USA. [3]Scripps Institution of Oceanography, University of California at San Diego, La Jolla, CA 92093–0225, USA.

*To whom correspondence should be addressed. E-mail: wolfe@hawaii.edu

Our data consist of waveforms from 1988 to 1998 in the catalog of routinely located deep earthquakes recorded by the HVO seismic network, amounting to 14,604 events spread across and around Hawaii. The voluminous Pu′u ′O′o-Kupaianaha eruption of Kilauea, which began in 1983 and still continues, was occurring throughout the study period. The seismic events at Kilauea can be classified into three types, (i) high-frequency earthquakes that indicate shear faulting, and (ii) long-period (LP) earthquakes and (iii) tremor (*12*, *13*) that likely reflect resonance in fluid-filled conduits. The data set contains 2376 LP events, with 90% above 20-km depth, and 135 tremor events, with 90% below 30-km depth (*14*).

Precise arrival time differences for earthquake pairs were obtained using waveform cross correlation with parameters appropriate for high-frequency earthquakes (*15*), and these data were able to relocate 7034 hypocenters, or 48% of the analyzed events. This calculation is a minimum estimate of the number of similar events, because pairs will not correlate highly if the signal-to-noise ratio is low: small magnitude events that are displaced far from stations, such as small, deeper earthquakes, are more difficult to constrain. Families of highly correlated earthquakes occur when there are closely spaced clusters with similar focal mechanisms, as at fault zones. Hence, our relocated clusters identify fault zones in the lithosphere beneath Hawaii.

The subset of 2522 earthquakes relocated in the vicinity of Kilauea is shown in Figs. 1 and 2, and fig. S1 displays the total set of 7034

Appendix C

Atom trapping with a magnetic thin film

This appendix contains a reprint of the hard disk platter paper, based on work described in Chapter 4. It was submitted to Physical Review A, and is currently under referee review.

Atom trapping with a thin magnetic film

Micah Boyd, Erik W. Streed, Patrick Medley, Gretchen K. Campbell, Jongchul Mun, Wolfgang Ketterle, David E. Pritchard*
MIT-Harvard Center for Ultracold Atoms, Research Laboratory of Electronics and Department of Physics, Massachusetts Institute of Technology, Cambridge, MA 02139, USA
(Dated: October 16, 2006)

We have created a ^{87}Rb Bose-Einstein condensate in a magnetic trapping potential produced by a hard disk platter written with a periodic pattern. Cold atoms were loaded from an optical dipole trap and then cooled to BEC on the surface with radiofrequency evaporation. Fragmentation of the atomic cloud due to imperfections in the magnetic structure was observed at distances closer than 40 μm from the surface. Attempts to use the disk as an atom mirror showed dispersive effects after reflection.

PACS numbers: 03.75.Be, 03.75.Lm, 75.50.Ss, 75.70.-i

Micrometer scale magnetic traps for Bose-Einstein condensates have been the focus of much experimental work since their first demonstration [1, 2]. Their potential uses in atom interferometry, precision measurements, and experiment miniaturization have motivated many groups to develop sophisticated techniques for manufacturing and controlling these atom chips [3–5]. However, since the earliest inceptions of atom chips, physical imperfections in the chip surface have lead to perturbations in the trapping potential that prohibit the coherent manipulation of atoms close to the surface[6, 7]. Permanent magnets offer a possible solution to several problems inherent to current carrying wire traps. First, the magnets are almost completely decoupled from the rest of the laboratory, minimizing the effects of environmental electrical noise. Second, they do not require current to be sourced or sinked, enabling designs that would be too complicated or impossible to create using electromagnets. Last, extremely high field gradients are possible close to magnetic domain boundaries, whereas traditional atom chip operation is limited by heat dissipation from small wires. Although a substrate of magnetizable material may be made extremely smooth and uniform, imperfections in the process of etching [8, 9] or writing magnetic structures could lead to some of the same problems as with wire-based designs. It is not yet known which technique will provide the best performance.

In this paper we investigate atom trapping with a thin magnetic film; specifically that of a hard disk platter written with a periodic pattern. This approach offers some advantages over previous work on neutral atom trapping and BEC creation using permanent magnets [4, 5, 10]. Here we use a thin metallic film with a large remnant magnetization from a commercial product which has already been refined to a high degree and a writing technique more accurate than anything previously demonstrated. Cold ^{87}Rb atoms were first loaded into the magnetic potential formed by the disk and used RF evaporation to produce BEC. By changing the trapping potential, the atoms could be pushed closer to the surface of the disk to probe for imperfections in the potential. Finally, the BEC was dropped onto the disk from a height of 2.7 mm in an attempt to produce a specular reflection of the atomic cloud.

The form of the written magnetization on the disk is of critical importance. A surface magnetization of the form

$$\boldsymbol{M(x)} = M_0 \cos(kx)\hat{y}, \tag{1}$$

where M_0 is the magnetization of the material and k is the wavevector of the sinusoidal pattern produces a magnetic field above the surface

$$(B_x, B_y, B_z) = B_0 e^{-ky} \left(-\cos(kx), sin(kx), 0\right), \tag{2}$$

which is of uniform coplanar magnitude and decays exponentially away from the surface [11]. This is an ideal potential for reflecting weak field seeking atoms.

The addition of a bias field B_x along $\hat{x}$ (or B_y along $\hat{y}$) produces a series of quadrupole shaped field minima above alternating tracks, depicted in Fig. 1. A second bias field B_z along $\hat{z}$ removes the magnetic field zero and weak field seeking atoms may be trapped near the surface with radial trap frequency

$$2\omega_r = kB_x\sqrt{\frac{\mu_B g_F m_F}{mB_z}} \tag{3}$$

where m is the atomic mass, and $\mu_B g_F m_F$ is the Zeeman energy [5, 11].

The magnetic media used in this work was a prototype hard disk with a radius of 65 mm and a thickness of 0.635 mm. The substrate is glass, and the magnetizable material is a dual layer system with a 23 nm thick magnetic Co-Cr-Pt based oxide layer and a 200 nm thick "magnetically soft underlayer", both of which are also good conductors and provide a total magnetization of 470 emu/cm^3 and a coercivity of $\sim$6000 Oe according to the manufacturer. The easy axis of magnetization of this prototype "out-of-plane" disk is aligned normal to the surface of the disk, as opposed to most modern commercial hard disks which are magnetized in the plane of the surface. The disk is also covered in a $\sim$1 nm layer of perfluoropolyether lubricant (Z-Tetraol). When written with pattern of $\lambda = 100$ μm (1 μm), the magnetic field at the surface is approximately 75 G (4200 G).

The disk was provided to us pre-written using a Guzik spin stand, which is essentially a hard disk read/write head with absolute positioning capability. This method of writing allows for the creation of truly arbitrary pattern impossible to

*URL: http://cua.mit.edu/ketterle_group/

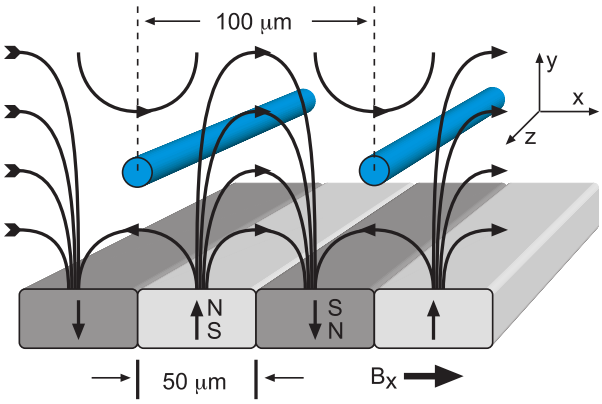

FIG. 1: Geometry of the magnetic trap formed by a magnetic film. Magnetic field lines resulting from the addition of a radial ($\hat{x}$) bias field to the magnetized surface. The tubes represent the locations of the field minima where atoms are trapped. The addition of an axial bias field of about 1.0 G along $\hat{z}$prevents atoms loss from Majorana spin flips.

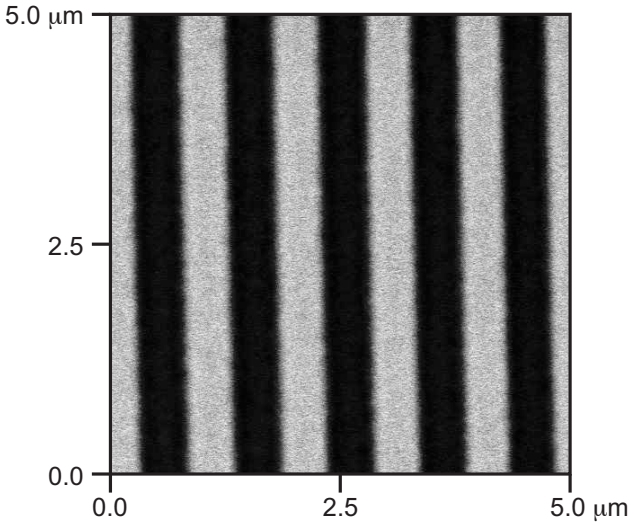

FIG. 2: Magnetic force microscopy image of the disk used in this experiment. This scan is over the region with λ = 1.0 μm. The track edges are of the same uniformity in the λ = 100.0 μm region. The characteristic size of the roughness of the domain boundaries is about 30 nm.

create with larger scale magnetic writing devices [5] or physical structures [4], and produces smaller and cleaner structures than optical writing techniques [12]. Two patterns were used in this experiment, written on different radial regions of the same disk. The first region had alternating stripes of up and down magnetization with a period of $2\pi/k = \lambda$ = 100.0 μm and the second had λ = 1.0 μm. The media has a very square hysteresis loop which precludes a purely sinusoidal magnetization. The pattern is instead written as a square wave, and the higher Fourier harmonics should be negligible at the height where we trap atoms [11]. Figure 2 shows a magnetic force microscopy image of the disk after writing which shows a significantly less noisy pattern than magneto-optical thin films written with laser beams [13]. Atomic force microscopy showed a physical roughness of $\sim$3 nm over a region of 50 μm.

One concern about the disk was that it could not be baked to the high temperatures (200 C) that we normally use to reach UHV. Digital data on similar disks is guaranteed to 80 C, but at 100 C the data starts to degrade rapidly as the superparamagnetic effect causes the magnetic domains to randomly reorient. The solution was to pre-bake the entire science chamber apparatus, without the disk, to 150 C for about a week to reach UHV conditions. The system was briefly opened up to air, the disk was installed, and then the chamber was pumped down again. The chamber was then heated only to 70 C for a few days, and after cooldown the pressure was $< 10^{-10}$ Torr. The recording signal decay rate quoted for this disk by its manufacturer was 0.4% per decade at room temperature, increasing to 0.8% per decade at 70 C. The effect of domain randomization would be most pronounced in the center of the written stripes, but minimal at the stripe edges where the configuration is more stable.

In our experiment, cold atoms were delivered to the surface in a two step process. First, cold ^{87}Rb atoms in the $F = 1, m_f = -1$ state were created in a Ioffe-Pritchard magnetic trap with $T \gtrsim T_c$ where T_c is the critical temperature for Bose-Einstein condensation. The atoms were then transferred to an optical dipole trap and transported 36 cm to a separate auxiliary chamber (see [14] for more details). The optical dipole trap was formed by a λ = 1064 nm laser focused to a 30 μm $1/e^2$ radius spot, and the focus (with the atoms) was translated into the auxiliary chamber as described in [15]. By transporting atoms just above T_c, the cloud was less sensitive to vibrations, and higher laser powers could be used without causing rapid three-body losses.

The atoms were loaded onto the surface from the optical trap by translating the focus of the optical trap to a position parallel to and 50 μm above the region with λ = 100 μm. A Z-shaped wire below the disk provided axial confinement, and a small B_x created radial trapping on the surface. The optical trap was ramped off over 2 seconds, transferring the atoms with almost unity efficiency. The optical trap enabled loading of >90% of the atoms into a single surface trap site. RF Evaporation over 20 seconds from 1.200 MHz to 0.890 MHz produced a BEC with approximately 50,000 atoms in a trap with $(\omega_x, \omega_y, \omega_z) = (390, 390, 9) \times 2\pi$ Hz. The spatial distribution was clearly bimodal, and condensate fractions of >80% were observed.

The atomic cloud was detected with on-resonance absorption imaging (Fig. 3). The platter is a good reflector (>95%) for 780 nm light, so grazing incidence imaging was used to measure the distance from the atoms to the surface. Normal incidence imaging was also used, in which case the imaging light passed through the atoms twice, bouncing off the disk. The lack of physical structures on the surface resulted in good image quality.

The axial trap frequency in the surface trap was measured by imaging oscillations of the atomic cloud, and radial trap frequencies were measured by parametric heating [Fig. 4].

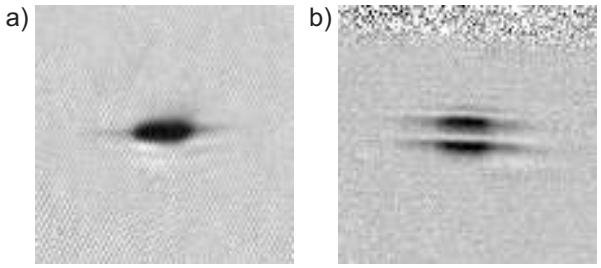

FIG. 3: Absorption image of the BEC in trap near the surface. a) Top imaging. The field of view is 0.58 mm × 0.58 mm. b) Side imaging. The field of view is 0.56 mm × 0.56 mm. The double image comes from the reflection of the imaging beam in the platter surface. The trap frequencies were $2\pi\times$(400, 400, 10) Hz. The configuration of the experiment prevented ballistic expansion, but the bimodal distribution in trap is still clear.

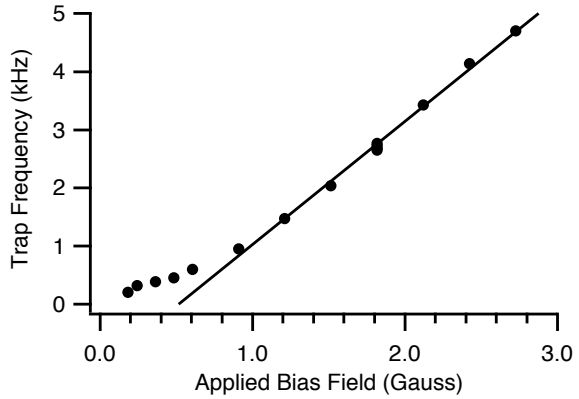

FIG. 4: Radial trap frequency vs applied radial magnetic field. Atoms were loaded into a single trap site on the surface and evaporated to BEC. The trap frequencies were measured with parametric heating, but above 5 kHz other heating effects made it difficult to resolve reliably. The deviation from linearity at low applied fields is most likely due to a small, off-axis, residual bias field.

Attempts to release the atoms from the trap and observe ballistic expansion in time of flight were hindered by the geometry of the system and the static nature of the magnetic surface, so all of the imaging was done in-trap. The Z-wire trap was left on at all times to provide axial trapping, but its effect on the radial trapping was negligible. Ramping up the current in external electromagnets increased B_x, and ω_r as high as $2\pi \times 5$ kHz was measured. Using a disk with λ = 10.0 μm, we have measured ω_r as high as 2π × 16 kHz. High transverse trap frequencies are desired for studies of 1D systems [16], but atom heating and loss at higher trap frequencies prevented such studies here.

While trapped 40 μm above the surface, the BEC had a lifetime of ∼30 s. Previous experiments with atomic clouds magnetically trapped near conducting surfaces showed atom loss resulting from spin flips driven by Johnson noise [7, 17, 18]. For this experiment however, the conducting layer was extremely thin (200 nm), and the atoms were relatively far from the surface. These two parameters reduced any spin flip loss below the level of our 1-body losses at a vacuum pressure of $\sim 5 \times 10^{-11}$ Torr.

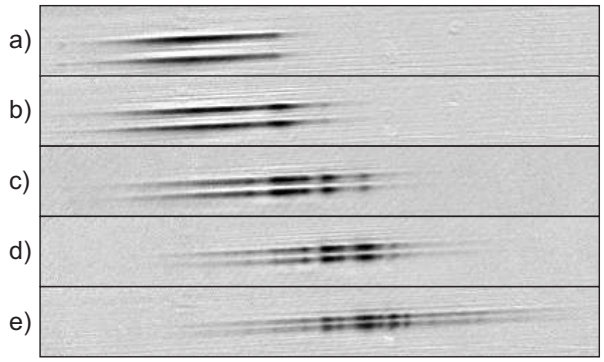

FIG. 5: Breakup of the atomic cloud as the atoms approached the surface. The thermal cloud was evaporated to $T \approx T_c$, then the axial trapping frequency was reduced to from 10 Hz to 1 Hz to allow the atoms to expand in one dimension. The axial bias field was then increased to push the atoms closer to the surface, and the atoms were imaged in trap. The grazing incidence imaging used here produces a double image of the atoms from the primary and secondary reflections of the imaging beam off the disk. The field of view is 0.29 mm × 2.3 mm, and each frame is an average of five distinct images to reduce noise for clarity. At distances smaller than 40 μm, significant breakup was observed. Height for the images shown: a) 35 μm b) 29 μm c) 25 μm d) 22 μm e) 19 μm.

The BEC was also used to probe imperfections in the trapping potential. After evaporation, the axial trapping frequency was reduced from 10 Hz to ∼1 Hz to allow the cloud to expand slightly in one dimension to increase the sensitivity and the measurement area, and the radial bias field (B_r) was increased to push the atoms closer to the surface. At distances closer than 40 μm, breakup of the atomic cloud was observed [Fig. 5], and the strength and spatial frequency of the perturbations increased as the atoms neared the surface, similar to [6, 19]. The magnitude and size scale of these imperfections can be attributed to the sputtering process used to create the film. Magnetic grain nucleation occurs randomly, resulting in small angular misalignments of the axes of anisotropy of individual magneto-crystalline domains (typically a few degrees), the individual magnetic grains can vary in size by about 25% of their ∼7 nm diameter, and the magnetic moments have a distribution of magnitudes. Finally, the recording head used to write the magnetic pattern can introduce unwanted magnetizations from edge effects. All of these phenomena create imperfections in atomic trapping potentials.

While the presence of these perturbations does not necessarily preclude the creation of neutral atom waveguides using this type of substrate, it does limit its usefulness. High trapping frequencies and single transverse mode confinement require close proximity to the surface and will suffer from the observed imperfections. However, for use as a high reliability, low noise, and low cost waveguide at distances >50 μm, commercial metallic, magnetic thin films are ideal.

The magnetized surface was also examined for its usefulness as an atom mirror as first proposed in [20] and demonstrated in [8, 21–23]. In order to minimize residual and time

dependent magnetic fields (from magnetic trap turnoff), all optical trapping was first used to create a BEC. The optical dipole trap provided only weak axial confinement, so a second, 200 mW laser beam with λ = 1064 nm and 200 μm waist was added in a crossed configuration, and allowed more efficient evaporation. To evaporate to BEC the power was reduced over 2.0 s. An axial bias field B_z = 1.2 G was maintained throughout the experiment, and B_x and B_y were minimized to <20 mG.

The region of the disk used as a magnetic mirror was written with λ = 1.0 μm. This value was chosen to be large compared to the magnetic writing precision, but small compared to the extent of the atomic cloud. The BEC was released from the crossed ODT 2.7 mm above the disk. The atoms fell under gravity for 23.5 ms and then reflected off the magnetic potential. The atomic cloud was imaged (in separate runs) from both the top and side after various times of flight. Side imaging showed that the reflection from the disk did not significantly effect the axial or vertical velocity distributions of the atomic cloud. Top imaging, however, showed significant spreading along the vector of the magnetic pattern after reflection, analogous to bouncing off a rough mirror [24]. The magnitude of this dispersion was minimized by fine tuning B_x and B_y, but was impossible to eliminate in our apparatus. Before bouncing off the disk, the $\hat{x}$ width of the cloud expanded by 1 mm/s, and after bouncing the $\hat{x}$ width increased by 34 mm/s. The reflection was not performed on the region with λ = 100.0 μm, but experiments using a different disk with λ = 10.0 μm showed similar effects.

The magnetic properties of the hard disk surface are one possible source of the observed expansion after reflection. While the theory presented earlier (Eq. 1) applies to a sinusoidally magnetized surface, the square hysteresis loop and directional anisotropy of digital recording media prevent recording of a pure sine wave, instead forming a square wave approximation of that sine, as discussed in [11]. While the higher harmonics resulting from this approximation do not necessarily adversely effect BEC trapping, they create a corrugation of the planar equipotential that may prevent the specular reflection of a macroscopic atomic cloud. However, field perturbations from harmonics or order n are of magnitude $B_0(1 - e^{-nkb})e^{-nky}$, and the effect of this corrugation at the reflection height ($\sim$ 4 μm) should be negligible ($<$ 1 mrad). Another contribution to the roughness of the reflection potential is the existence of small, stray magnetic fields. Any nonzero component of B in the $\hat{x}\hat{y}$ plane creates a regular corrugation in the plane, further inhibiting specular reflection. While the bias field in the B_x and B_y planes was minimized at the atoms, magnetic field gradients from external sources, such as a nearby ion pump, were not compensated. However, an overestimate of the residual magnetic field gradient still underestimates the amount of dispersion observed after reflection. The primary cause of the dispersion is thus unknown. Diffraction peaks that might result from reflection off such a corrugated surface were not observed.

In conclusion, we have demonstrated BEC production on the surface of a hard disk platter. Small scale imperfections in the magnetization caused condensate fragmentation close to the surface, prohibiting its use as a neutral atom waveguide. The disk was also used as an atom mirror, and specular reflection was observed on two axes. These results are a substantial improvement over that for early wire based experiments, and the possibility for more complex structures enables trap geometries impossible for electromagnets. Microtraps based on permanent magnets, and in particular magnetic metallic thin films, may become an alternative to atom chips using current-carrying wires if the fabrication can be further improved, e.g. by using molecular beam epitaxy, and the writing process improved by using write heads optimized for recording DC structures on perpendicular media.

The authors would like to thank Aaron Leanhardt for experimental assistance, Tom Pasquini for a critical reading of the manuscript, and Min Xiao at Hitachi Global Storage Technologies for writing several disks for us and providing the MFM images, this work would not have been undertaken without her assistance.

[1] H. Ott, J. Fortagh, G. Schlotterbeck, A. Grossmann, and C. Zimmermann, Phys. Rev. Lett. **87**, 230401 (2001).
[2] W. Hänsel, P. H. annd T. W. Hänsch, and J. Reichel, Nature **413**, 498 (2001).
[3] Y. Shin, C. Sanner, G. B. Jo, T. A. Pasquini, M. Saba, W. Ketterle, D. E. Pritchard, M. Vengalattore, and M. Prentiss, Phys. Rev. A **72**, 021604(R) (2005).
[4] B. V. Hall, S. Whitlock, F. Scharnberg, P. Hannaford, and A. Sidorov, J. Phys. B: At. Mol. Opt. Phys. **39**, 27 (2006).
[5] C. D. J. Sinclair, E. A. Curtis, I. L. Garcia, J. A. Retter, B. V. Hall, S. Eriksson, B. E. Sauer, and E. A. Hinds, Phys. Rev. A **72**, 031603(R) (2005).
[6] A. E. Leanhardt, Y. Shin, A. P. Chikkatur, D. Kielpinski, W. Ketterle, and D. E. Pritchard, Phys. Rev. Lett **90**, 100404 (2003).
[7] Y. J. Lin, I. Teper, C. Chin, and V. Vuletić, Phys. Rev. Lett. **92**, 050404 (2004).
[8] B. Lev, Y. Lassailly, C. Lee, A. Scherer, and H. Mabuchi, Appl. Phys. Lett. **83**, 395 (2003).
[9] J. Wang, S. Whitlock, F. Scharnberg, D. Gough, A. Sidorov, R. McLean, and P. Hannaford, Journal of Physics D: Applied Physics **38**, 4015 (2005).
[10] S. Wu, E. J. Su, and M. Prentiss, cond-mat/0406482 (2006).
[11] E. A. Hinds and I. G. Hughes, J. Phys. D **32**, R119 (1999).
[12] S. Eriksson, F. Ramirez-Martinez, E. A. Curtis, B. E. Sauer, P. W. Nutter, E. W. Hill, and E. A. Hinds, Appl. Phys. B: Lasers and Optics **79**, 811 (2004).
[13] D. C. Lau, R. J. McLean, A. I. Sidorov, D. S. Gough, J. Koperski, W. J. Rowlands, B. A. Sexton, G. I. Opat, and P. Hannaford, J. Opt. B: Quantum Semiclass. Opt. **1**, 371 (1999).
[14] E. W. Streed, A. P. Chikkatur, T. L. Gustavson, M. Boyd, Y. Torii, D. Schneble, G. K. Campbell, D. E. Pritchard, and W. Ketterle, Rev. Sci. Instr. **77**, 023106 (2006).
[15] T. L. Gustavson, A. P. Chikkatur, A. E. Leanhardt, A. Görlitz, S. Gupta, D. E. Pritchard, and W. Ketterle, Phys. Rev. Lett **88**, 020401 (2001).

[16] J. I. Kim, J. Schmiedmayer, and P. Schmelcher, Phys. Rev. A **72**, 042711 (2005).
[17] M. P. A. Jones, C. J. Vale, D. Sahagun, B. V. Hall, and E. A. Hinds, Phys. Rev. Lett **91**, 080401 (2003).
[18] S. Scheel, P. K. Rekdal, P. L. Knight, and E. A. Hinds, Phys. Rev. A **72**, 042901 (2005).
[19] D. Cassettari, B. Hessma, R. Folman, T. Maier, and J. Schmiedmayer, Phys. Rev. Lett. **85**, 5483 (2000).
[20] G. I. Opat, S. J. Wark, and A. Cimmino, AppL. Phys. B **54**, 396 (1992).
[21] T. M. Roach, H. Abele, M. G. Boshier, H. L. Grossman, K. P. Zetie, and E. A. Hinds, Phys. Rev. Lett. **75**, 629 (1995).
[22] A. I. Sidorov, R. J. McLean, W. J. Rowlands, D. C. L. annd J. E. Murphy annd M. Walkiewicz, G. I. Opat, and P. Hannaford, Quantum Semiclass. Opt. **8**, 713 (1996).
[23] A. I. Sidorov, R. J. McLean, F. Scharnberg, D. S. Gough, T. J. Davis, B. J. Sexton, G. I. Opat, and P. Hannaford, Acta Physica Polonica B **33**, 2137 (2002).
[24] H. Perrin, Y. Colombe, B. Mercier, V. Lorent, and C. Henkel, Journal of Physics: Conference Series **19**, 151 (2005).

Appendix D

A Mott insulator atomic clock

This appendix contains the most recent draft of the Mott insulator atomic clock paper, based on work described in Chapter 5. It is still being revised, and will be submitted to Physical Review A upon completion. It was my last experimental work at MIT.

A Mott Insulator Atomic Clock

Rb Lab*
MIT-Harvard Center for Ultracold Atoms, Research Laboratory of Electronics and Department of Physics, Massachusetts Institute of Technology, Cambridge, MA 02139, USA
(Dated: September 13, 2006)

We have implemented a proof-of-principle atomic clock using a ^{87}Rb Bose-Einstein condensate confined in an 3D optical lattice. Several typical sources of systematic error were eliminated by preparing the atoms in the Mott insulator (MI) phase before measurement. The suppression of tunneling in the MI phase permitted longer measurements than possible with other optical confinement techniques for the same optical power, as well as elimination of the density shift due to the discretized filling factor. The hyperfine transition of ^{87}Rb was measured with a FWHM linewidth of 1.2 Hz and an uncertainty of 0.2 Hz out of 6.8 GHz.

PACS numbers:

Precision frequency and time measurements provide a fundamental reference for the basis of nearly every physical measurement. Modern measurements have improved the accuracy of atomic clocks to the 10^{-15} level [1–5], and recent experiments with optical transitions in trapped, neutral atoms promise precision at the 10^{-18} level [6]. As the properties of clock atoms are measured more precisely, care must be taken to prevent the environment, and in some cases the atoms themselves, from affecting the measurement.

Unwanted perturbations to an atomic clock system can come from external sources, such as external trapping for cold atoms or stray electromagnetic fields in the laboratory, or from internal sources, such as the atomic cold-collision shift [1, 7, 8] or dipole-dipole interactions [7, 9]. Although systems can be shielded from external perturbations, it is more difficult to control the effect of interactions. Simultaneously interrogating a large number of atoms N can increase the signal to noise ratio by $\sqrt{N}$, but increasing the atom number typically comes at a cost of increased density, leading to greater uncertainty due to interactions. For example, the microwave hyperfine transition of cold ^{87}Rb at a typical density of 10^{13} cm^{-3} will be perturbed by the "clock" shift at a level of 2 Hz. One way to minimize such collisions is to hold the atoms in an optical lattice.

In this work we implement an atomic clock by measuring a microwave hyperfine transition in a ^{87}Rb Bose-Einstein condensate (BEC) confined in a 3D optical lattice. Atomic clocks using neutral atoms in an optical lattice have been demonstrated previously [6, 10, 11], but here we eliminate a key source of systematic error by increasing the depth of the lattice potential to confine the atoms in the Mott insulator (MI) regime. In the MI phase, tunneling is suppressed due to the onsite interaction energy, reducing the lattice depth required to minimize interactions. This reduced lattice depth avoids complications such as higher order light shifts [12]. As recently shown [13], the microwave spectrum of the MI with ^{87}Rb shows discrete peaks corresponding to the integer filling factor of individual lattice sites. This discretization of the density shift eliminates density dependent errors in the measurement of the transition frequency, and should also not be limited by phase separation or collisions [14]. Systematic shifts due to trapping laser intensity may also be extrapolated to zero intensity by varying the laser power over a wide range within the MI regime.

Bosons held in a 3D optical lattice with repulsive interactions are described by the Bose-Hubbard Hamiltonian [15, 16]

$$\hat{H} = -J \sum_{\langle i,j \rangle} \hat{a}_i^\dagger \hat{a}_j + \frac{1}{2} U \sum_i \hat{n}_i(\hat{n}_i - 1) + \sum_i (\epsilon_i - \mu)\hat{n}_i, \quad (1)$$

where J is the tunneling term between nearest neighbors, $\hat{n}_i = \hat{a}_i^\dagger \hat{a}_i$ is the number of atoms in the i^{th} lattice site, U is the repulsive onsite interaction, $\epsilon_i = V_{ext}(r_i)$ is the energy due to the external confinement, and μ is the chemical potential. The onsite interaction is expressed as $U = (4\pi\hbar^2 a/m) \int |w(x)|^4 d^3x$, where a is the s-wave scattering length, m is the atomic mass, and $w(x)$ is the single particle Wannier function. The first term in the Hamiltonian tends to delocalize atoms over the lattice due to tunneling, while the second term tends to localize atoms to lattice sites due to atom-atom interactions. For low lattice depths, the ratio J/U is large and the system behaves as a superfluid. As the lattice depth is increased, the localizing effects of the interaction begin to dominate, and the system undergoes quantum phase transition to a MI phase. The MI phase is characterized by Fock states, where atoms are localized to individual lattice sites with integer filling factor. Due to the external confinement and the initial density distribution of the condensate, this filling factor is a maximum in the center of the trap, and decreases to the edge of the atomic cloud. The result is a series of concentric shells, each with uniform filling. It is this discrete filling which we utilize to eliminate the density shift of our atomic clock.

The density dependent shift in ^{87}Rb is determined by the difference in the scattering lengths a_{11} and a_{21}, where a_{21} is the scattering length between an atom in the $F = 2, m_F = +1$ state and one in the $F = 1, m_F = -1$ state. The resulting mean field energy shift

$$\Delta E = \frac{h^2}{\pi m \rho}(a_{21} - a_{11}) \quad (2)$$

will then resolve to discrete frequency shifts in the microwave

*URL: http://cua.mit.edu/ketterle_group/

$|1,-1\rangle \rightarrow |2,1\rangle$ hyperfine transition for integer lattice filling factors, where ρ is the atomic density. The resulting microwave spectrum for a MI is then a series of peaks, and the frequency difference between neighboring MI shells is then [17]

$$\delta\nu = \frac{U}{h}\frac{(a_{21}-a_{11})}{a_{11}}. \quad (3)$$

For our experiments, the BEC was created using forced radiofrequency (RF) evaporation of a ^{87}Rb atomic cloud in the $|F, m_F\rangle = |1,-1\rangle$ state, as described previously in [18]. The trapping potential was formed by the combination of a Ioffe-Pritchard magnetic trap and a retro-reflected, cross polarized optical dipole trap. The optical trap was oriented perpendicular to the weak axis of the magnetic trap to provide a more spherical geometry for better mode matching to the optical lattice [13]. BECs containing $\sim 1.5\times10^6$ atoms with no discernible thermal component were held for 5 seconds with a constant RF shield to reduce shot-to-shot atom number fluctuations to below 5%. For most measurements, a fast RF sweep through the RF resonance was used to reduce the atom number by ∼75%. A 3D optical lattice was then adiabatically ramped on using an exponential increase with a 40 ms time constant. Two lattice axes were formed by increasing the intensity in retro-reflected beams, while the third axis was formed by rotating the polarization of the retro-reflected optical dipole trap using a liquid crystal waveplate. The lattice beams were all derived from the same laser with λ = 1064 nm, and were detuned from each other by acousto-optic modulators. The beams also all had roughly equivalent $1/e^2$ beams waist radii of 150 μm, focused on the atoms. The lattice depth was increased up to 35 E_{rec} where $E_{rec} = \hbar^2k^2/(2m)$ and $k = 2\pi/\lambda$ is the wavevector of the lattice. After ramping up the lattice, the atoms were held for 50 ms before measurement to compensate for transient nematic effects in the liquid crystal polarization rotator. The resulting MI structure was calculated to contain approximately 7×10^4 atoms in the $n = 1$ shell.

A single two-photon pulse resonant with the $|1,-1\rangle \rightarrow |2,1\rangle$ transition was applied to the atoms in the lattice for some time τ, as depicted in Fig. 1. The pulse consisted of a microwave photon at 6.83 GHz and a RF photon at ≈1.6781 MHz. The microwave synthesizer was an Agilent E8257D running off its internal timebase. The RF synthesizer was an Agilent 33250a, and was synchronized to the 10 MHz timebase of the microwave synthesizer. Magnetic field dependent line shifting and broadening was avoided by working at a bias field of ∼3.23 Gauss, where the two states experience the same first order Zeeman shift [17]. The power of the pulse was adjusted to produce a π pulse for each hold time τ. Immediately after the pulse, the confining potentials were switched off and the atomic cloud was allowed to expand for 3 ms to reduce the column density. Atoms in the $|2,1\rangle$ state were detected with absorption imaging using light resonant with the $5^2S_{1/2}|2,1\rangle \rightarrow 5^2P_{3/2}|3,1\rangle$ transition.

As the lattice is ramped up, the ac Stark shift and the density shift begin to broaden and move the resonance of the $|1,-1\rangle \rightarrow |2,1\rangle$ microwave transition to lower frequencies.

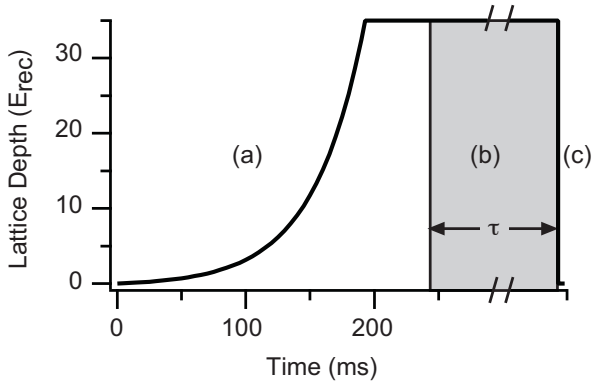

FIG. 1: Diagram of the experimental procedure. (a) The lattice is ramped up to $U = 35E_{rec}$ in 193 ms, then held for 50 ms. (b) The two photon pulse is applied for time τ, then (c) the atoms are released from the trap and imaged in 3 ms time of flight.

As the lattice depth is increased, the tunneling rate decreases until it is completely suppressed at depths greater than approximately 15 E_{rec} due to the transition to the MI phase. Discrete peaks begin to appear in the microwave spectrum, corresponding to cold collision density shifts resulting from integer filling factors within lattice sites. The observation of discrete peaks is direct evidence for the suppression of tunneling by interactions when the MI transition is reached. Tunneling of atoms between sites of different occupation number during the microwave pulse would broaden the discrete peaks and eventually lead to peaks reflecting the clock shift at an averaged density. We estimate the tunneling time in the absence of interactions using a double-well model to be $h/4Jnz$, where z is the number of next neighbors, and n is the filling factor. For $n = 1$, the tunneling time is ∼5 ms at 20 E_{rec}, 13 ms at 25 E_{rec} and 60 ms at 35 E_{rec}. A very deep lattice would localize atoms even for a thermal or non-interacting gas. However, for our lattice depths no discrete spectrum was observed when the cloud was heated during the ramp up by misalignment of the lattice beams. Our spectra were taken under conditions where if the lattice were immediately ramped back down, condensate fraction remaining was greater than 80%.

By using long two-photon pulses, we narrowed the bandwidth of the scan and increased the resolution the $n = 1$ and $n = 2$ peaks from that reported in our previous work [13] (Fig. 2). Using a double Gaussian fit of the form $y = y_o + A_1e^{-(x-x_1)^2/\sigma_1^2} + A_2e^{-(x-x_2)^2/\sigma_2^2}$, the $n = 1$ peak was more than $10\sigma_2$ removed from the $n = 2$ peak, indicating that any higher density contribution to the singly occupied sites was removed at a level better than 10^{-5}. Thus by using the MI phase to separate density shifts into carrier and sideband peaks, we were able avoid density dependent shifts that affect other atomic clock experiments. By increasing the length, and thus narrowing the bandwidth of the microwave pulse, we were able to measure successively smaller linewidths of the singly occupied sites down to 1.0(2) Hz FWHM (Fig. 3). Pulse lengths longer than 1200 ms did not further decrease the width of the transition.

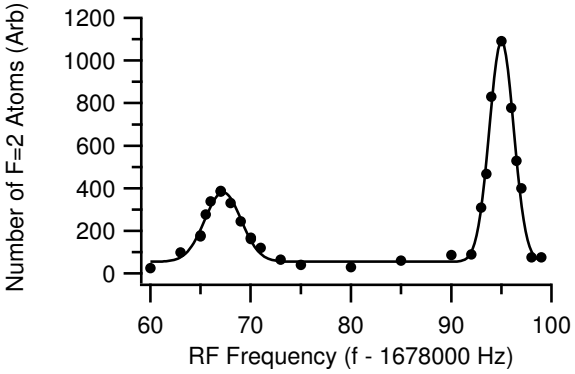

FIG. 2: Microwave scan of atoms in the lattice. The $n = 2$ peak is centered at 1,678,067.2 $\pm$ 0.1 Hz with a FWHM of 4.2 $\pm$ 0.8 Hz, and the $n = 1$ peak is centered at 1,678,095.03 $\pm$ 0.03 Hz with a FWHM of 2.85 $\pm$ 0.08 Hz. The fit is a double Gaussian, and shows that the $n = 2$ peak is move than five linewidths removed from the $n = 1$ peak, eliminating the density shift. The lattice depth was a 35 E_{rec}, and the measurement time was 300 ms.

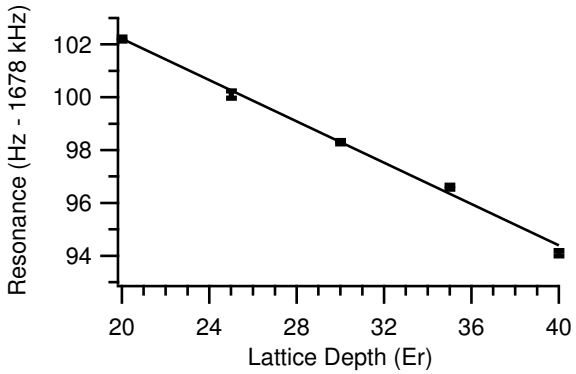

FIG. 4: Center frequency of the $n = 1$ peak vs. lattice depth. The center of the single occupation peak was measured as a function of lattice depth in order to extrapolate to zero laser intensity. The line is a linear fit which gives a zero intercept of 110.04 $\pm$ 0.18 Hz, indicating an ac Stark shift free frequency of 6,834,678,110.04 $\pm$ 0.18 Hz. The error bars are not fully resolved on this graph, with a typical value of $\pm$0.10 Hz.

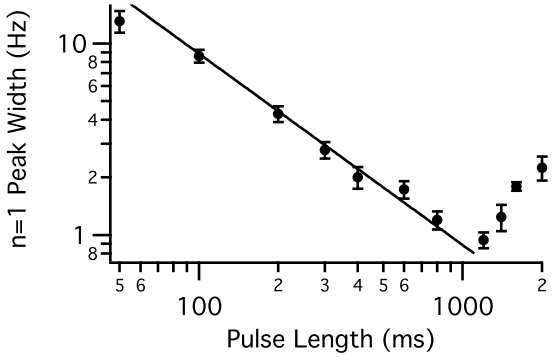

FIG. 3: Width of the $n = 1$ peak vs. two photon pulse length. After loading into the lattice, the width of the single occupation density peak was measured as a function of the interrogation pulse length. The two photon intensity was adjusted to provide a π pulse at each hold time. The line represents the theoretical bandwidth of the pulse. Pulses longer than 1200 ms resulted in larger peak widths due to technical noise, primarily from our microwave synthesizer.

In order to correct for the frequency shift induced by the ac Stark effect, the location of the $n = 1$ peak was measured for a variety of lattice depths in the MI regime. Since the ac Stark shift scales linearly with laser power, measuring the resonance as a function of lattice depth allowed us to quantify this effect. After a linear fit to the data (Fig. 4), extrapolation to a depth of 0 E_{rec} revealed the resonance frequency without any linear laser intensity dependent shifts. This extrapolation increased the uncertainty of the measurement by about a factor of two over that of a typical single frequency measurement. The minimum lattice depth required to clearly resolve the $n = 1$ peak was 20 E_{rec}, and a maximum depth of 40 E_{rec} was used. After extrapolation, the $|1, -1\rangle \rightarrow |2, +1\rangle$ hyperfine transition frequency was measured to be 6,834,678,015.20(18) Hz (statistical). After applying a 4497.3 Hz correction predicted from the Breit-Rabi formula for the finite magnetic field [19], this is 98.4 Hz from the accepted value of 6,834,682,610.90434(3) Hz [20], but the focus of this work was only to control systematic errors resulting from inter-atomic interactions, not to make a high accuracy measurement.

The primary determinant of the peak width was the bandwidth of the two-photon pulse. In the case of a bandwidth limited pulse, the lineshape should be a sinc squared with a FWHM of $0.8859/\tau$. This is shown as the solid line in Fig. 3, which agrees well with the data for $\tau < 1$ s. For times longer than 1 s, several sources of inhomogeneous broadening begin to affect the lineshape. The largest source of inhomogeneous broadening in our experiment is due to a magnetic field gradient across the atomic cloud. Our magnetic trap is operating at the low limit of holding the atoms against gravity, and thus we assume that the entire cloud is trapped in a constant vertical magnetic field gradient of 15 G/cm. Taking a $n = 1$ shell radius of 19 μm, we calculate a field gradient of 58 mG vertically across the entire cloud, implying a broadening of the hyperfine transition of $\sim$0.36 Hz due to the inhomogeneous magnetic field. The effect of the magnetic bias field on the peak width is shown in Fig. 5. Since the magnetic field broadening depends on the size of the atomic cloud, a large atom number could lead to larger linewidths. However, within the statistical uncertainty of the fits, the width of the $n = 1$ peak was not found to be significantly sensitive to atom number in the range $10^5 < N < 10^6$.

Another source of inhomogeneous broadening is the differential ac Stark shift. If the clock measurement samples atoms which are trapped in regions of different laser intensity, the resonance will be broadened. However, the shell structure of the MI phase will tend to minimize effects from the differential ac Stark shift as all of the atoms in the measured shell are trapped in approximately the same laser intensity. If the atomic cloud is small compared to the diameter of the

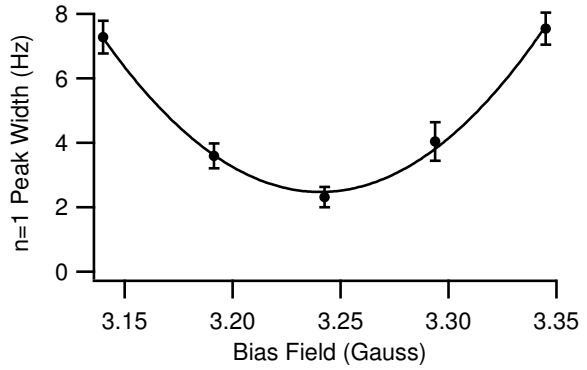

FIG. 5: FWHM of the $n = 1$ peak vs magnetic field. Control of the magnetic field at a level of <20 mG was necessary to minimize inhomogeneous magnetic field broadening. The line is a parabolic fit to guide the eye.

lattice beams, this effect will also be small. Assuming that the measured atoms consist of a shell with radius equal to the Thomas-Fermi radius of the BEC, we calculate that the differential ac Stark shift across the shell results in a broadening of <0.2 Hz. This broadening scales linearly with the inverse of the beam diameters, so narrow beams used for all optical trapping would adversely effect the measurement. For example, 20 μm waist beams would lead to a differential ac Stark shift broadened peak width of $\sim$2 Hz, dominating other sources of broadening currently observed. This broadening, as well as the total ac Stark shift may be reduced by the use of a "magic" wavelength lattice. By carefully choosing λ so that the two interrogated levels are shifted equally by the trapping laser, the ac Stark shift may be reduced by several orders of magnitude [6]. In the absence of a magic wavelength, a blue-detuned lattice laser could be used, trapping the atoms in regions of minimum laser intensity [21].

One possible source of homogeneous broadening is the existence of particle-hole pairs within the $n = 1$ number state[22, 23]. The tunneling term of the Hamiltonian acts as a perturbation on the otherwise uniform array of Fock states in the MI phase, adding a small superposition of $n = 0$ and $n = 2$ noise to the $n = 1$ signal. This manifests itself in our measurement as a small shift of the $n = 1$ peak towards $n = 2$ due to the slightly increased average density. However, this effect scales as J/U, and for a lattice depth of 35 E_{rec}, the 0.2% mixture generates a shift of 0.05 Hz and would be further reduced for larger lattice depths.

Another systematic shift which depends on interactions is the induced dipole-dipole shift [24, 25], where the measurement field drives dipole oscillations in the atoms which effect neighboring lattice sites. Since the measurement wavelength ($\lambda_{\mu w}$ $\approx$50 mm) is very long compared to the lattice spacing (d = 523 nm), there will be a dipole-dipole interaction in the near field regime. However, the very narrow linewidth of the $|1,-1\rangle \rightarrow |2,0\rangle$ transition ($\sim 10^{-8}$ s^{-1}), as well as the relatively large single photon detuning (420 Hz) imply an interaction energy shift of < 0.02 Hz [21]. Experiments using measurements in the optical regime will benefit from a reduced interaction since the energy shift scales as $(\lambda/d)^3$ [25], and careful selection of the lattice geometry can even further suppress this effect [24].

The main source of systematic error in this experiment was the microwave frequency source. Our synthesizer was not linked to any external reference clock, such as GPS, and the specified drift rate of 4.5 ppb per day corresponded to 31 Hz per day at 6.8 GHz. Indeed, frequency jumps as large as 20 Hz over a two day period were observed when temperature stability in the lab was not maintained. Future experiments would certainly implement better master oscillator stabilization. Using a two-pulse Raman technique was investigated, but phase jitter due to synthesizer frequency noise made accurate fitting of the resulting signal difficult. The use of a double pulse method is only limited by the fact that each of the two pulses must have a bandwidth narrow enough to not address any atoms in sites with occupation greater than one, and would improve the accuracy of future experiments.

In conclusion, we have implemented an atomic clock with a BEC trapped in the MI phase of a 3D optical lattice. While our demonstration is not competitive with current atomic clocks, the density discretization technique shown here could be used to increase the precision of optical frequency Ca, Yb, and Sr clocks currently under development [2, 26–30].

[1] F. Pereira Dos Santos, H. Marion, S. Bize, Y. Sortais, A. Clairon, and C. Salomon, Phys. Rev. Lett. **89**, 233004 (2002).

[2] C. W. Oates, E. A. Curtis, and L. Hollberg, Opt. Lett. **25**, 1603 (2000).

[3] S. A. Diddams, T. Udem, J. C. Bergquist, E. A. Curtis, R. E. Drullinger, L. Hollberg, W. M. Itano, W. D. Lee, C. W. Oates, K. R. Vogel, et al., Science **293**, 825 (2001).

[4] C. Degenhardt, H. Stoehr, C. Lisdat, G. Wilpers, H. Schnatz, B. Lipphardt, T. Nazarova, P. Pottie, U. Sterr, J. Helmcke, et al., Physical Review A **72**, 62111 (2005).

[5] N. Davidson, H. Jin Lee, C. S. Adams, M. Kasevich, and S. Chu, Phys. Rev. Lett. **74**, 1311 (1995).

[6] M. Takamoto, F.-L. H. annd Ryoichi Higashi, and H. Katori, Nature **435**, 321 (2005).

[7] C. Fertig and K. Gibble, Phys. Rev. Lett. **85**, 1622 (2000).

[8] Y. Sortais, S. Bize, M. A. S. Zhang, C. Nicolas, C. Mandache, P. Lemonde, P. L. annd G. Santarelli annd N. Dimarcq, P. Petit, A. Clairon, A. Mann, et al., Phys. Scr. **T95**, 50 (2001).

[9] V. A. Sautenkov, H. van Kampen, E. R. Eliel, and J. P. Woerdman, Phys. Rev. Lett. **77**, 3327 (1996).

[10] Z. W. Barber, C. W. Hoyt, C. W. Oates, L. Hollberg, A. V. Taichenachev, and V. I. Yudin, Phys. Rev. Lett. **96**, 83002 (2006).

[11] A. D. Ludlow, M. M. Boyd, T. Zelevinsky, S. M. Foreman, S. Blatt, M. Notcutt, T. Ido, and J. Ye, Phys. Rev. Lett. **96**, 033003 (2006).

[12] P. Lemonde and P. Wolf, Phys. Rev. A **72**, 33409 (2005).

[13] G. K. Campbell, J. Mun, M. Boyd, P. Medley, A. E. Leanhardt,

L. G. Marcassa, D. E. Pritchard, and W. Ketterle, Science **313**, 649 (2006).

[14] D. Kadio and Y. B. Band, *Analysis of a magnetically trapped atom clock* (2006), URL http://arxiv.org/abs/physics/0608024.

[15] M. P. A. Fisher, P. B. Weichman, G. Grinstein, and D. S. Fisher, Phys. Rev. B **40**, 546 (1989).

[16] D. Jaksch, C. Bruder, J. I. Cirac, C. W. Gardiner, and P. Zoller, Phys. Rev. Lett. **81**, 3108 (1998).

[17] D. M. Harber, H. J. Lewandowski, J. M. McGuirk, and E. A. Cornell, Phys. Rev. A **66**, 053616 (2002).

[18] E. W. Streed, A. P. Chikkatur, T. L. Gustavson, M. Boyd, Y. Torii, D. Schneble, G. K. Campbell, D. E. Pritchard, and W. Ketterle, Rev. Sci. Instr. **77**, 023106 (2006).

[19] D. A. Steck, http://steck.us/alkalidata (2003).

[20] C. Salomon, Y. Sortais, S. Bize, M. Abgrall, S. Zhang, C. Nicolas, C. Mandache, P. Lemonde, P. Laurent, G. Santarelli, et al., ICAP 2000 (American Institute of Physics, 2000), p. 23.

[21] G. K. Brennen, C. M. Caves, P. S. Jessen, and I. H. Deutsch, Phys. Rev. Lett. **82**, 1060 (1999).

[22] F. Gerbier, A. Widera, S. Fölling, O. Mandel, T. Gericke, and I. Bloch, Phys. Rev. Lett. **95**, 050404 (2005).

[23] F. Gerbier, A. Widera, S. Fölling, O. Mandel, T. Gericke, and I. Bloch, Phys. Rev. A **72**, 053606 (2005).

[24] D. E. Chang, J. Ye, and M. D. Lukin, Phys. Rev. A **69**, 023810 (2004).

[25] H. Katori, M. Takamoto, V. G. Pal'chikov, and V. D. Ovsiannikov, Phys. Rev. Lett. **91**, 173005 (2003).

[26] T. Udem, S. A. Diddams, K. R. Vogel, C. W. Oates, E. A. Curtis, W. D. Lee, W. M. Itano, R. E. Drullinger, J. C. Bergquist, and L. Hollberg, Phys. Rev. Lett. **86**, 4996 (2001).

[27] T. Udem, R. Holzwarth, and T. W. Hänsch, Nature **416**, 233 (2002).

[28] G. Wilpers, T. Binnewies, C. Gegenhardt, U. Sterr, J. Helmche, and F. Riehle, Phys. Rev. Lett. **89**, 230801 (2002).

[29] F.-L. Hong, M. Takamoto, R. Higashi, Y. F. annd Jie Jiang, and H. Katori, Optics Express **13**, 5253 (2005).

[30] C. W. Hoyt, Z. W. Barber, C. W. Oates, T. M. Fortier, S. A. Diddams, and L. Hollberg, Phys. Rev. Lett. **95**, 83003 (2005).

Appendix E

Science chamber schematics

This appendix contains drawings of the science chambers used on the rubidium machine.

E.1 Hard Disk Platter Science Chamber

The hard disk platter chamber consisted of a six inch radius sphere faced with viewports. A vacuum bellows manipulator sat on top of the chamber to hold and position the hard disk platter. Position control in the pennywindow horizontal axis was achieved with micro-positioner translation stages, and tilt and vertical control was maintained by three jackscrews. The diagram below shows the chamber with the manipulator section rotated 90 degrees about the vertical axis for clarity.

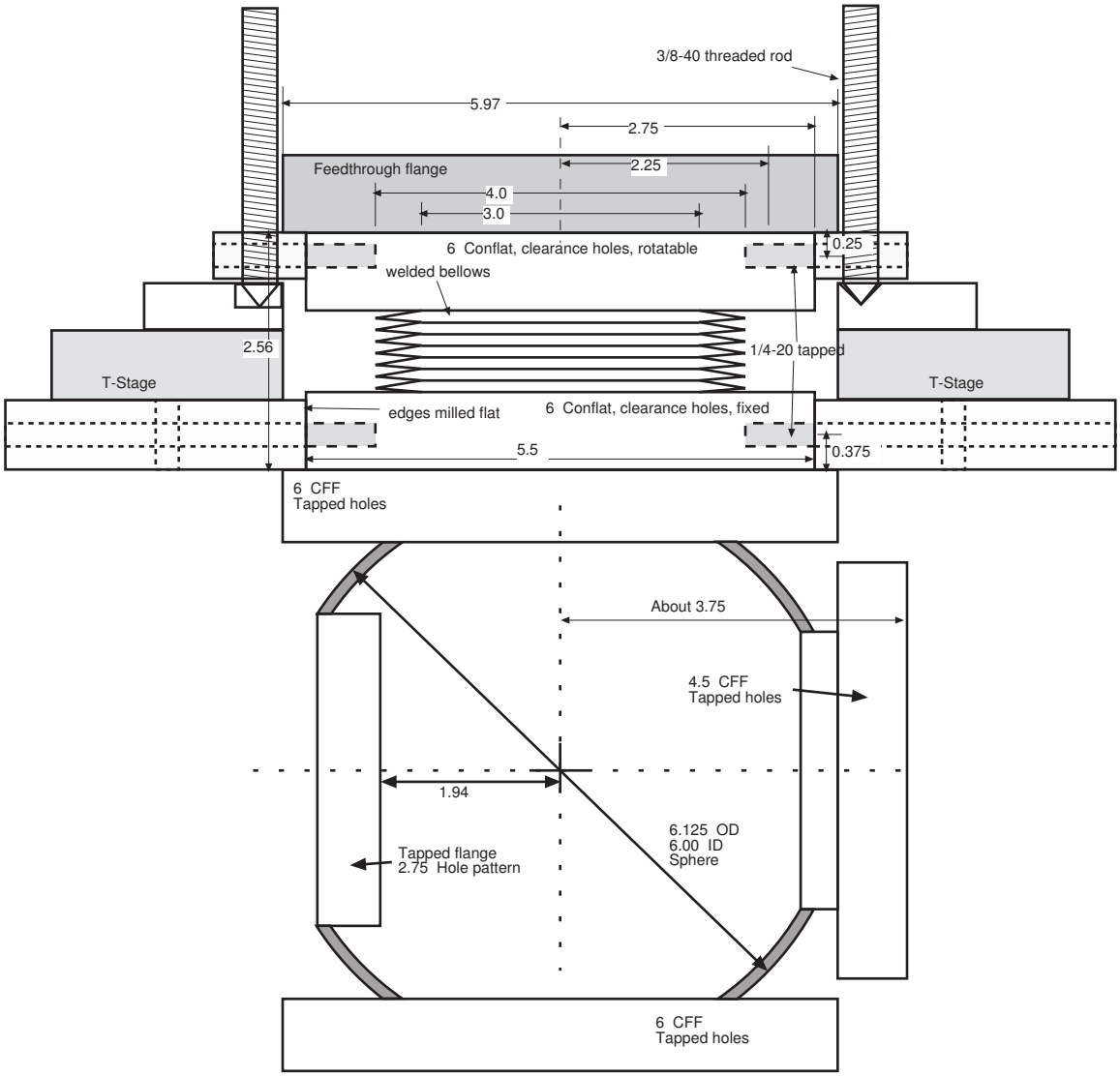

E.2 Optical Lattice Science Chamber

While not used in this work, this science chamber will be installed on the rubidium machine shortly after the completion of this thesis. It was designed to afford a maximum of optical access, while maintaining UHV capability.

E.2.1 Lattices Science Chamber Top View

This science chamber design accommodates six axes; three for lattices and one for imaging, and one for optical transport from the main chamber.

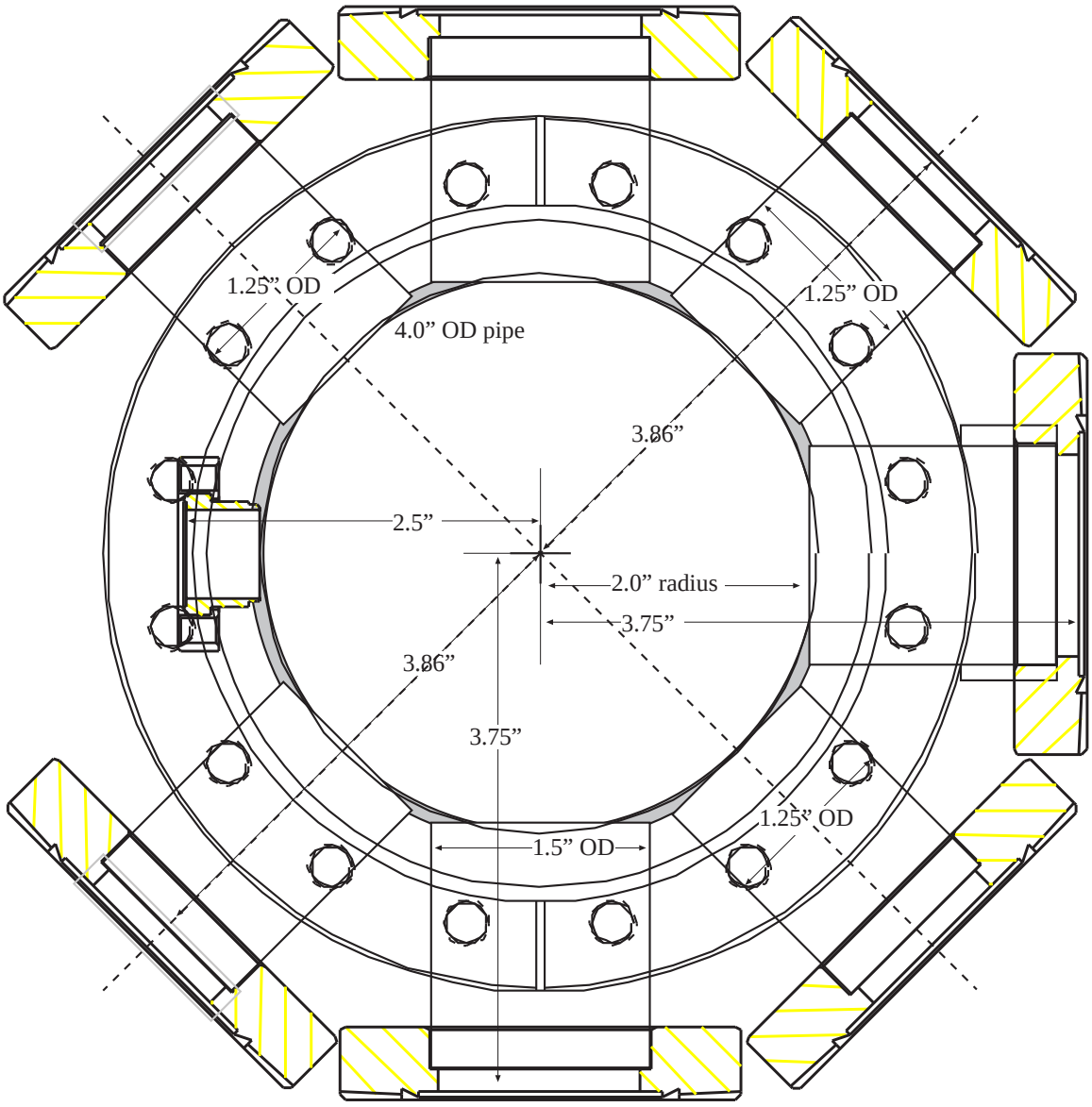

E.2.2 Lattices Science Chamber Side View

Imaging with aperture close for $f = 1$ is achieved through the top viewport.

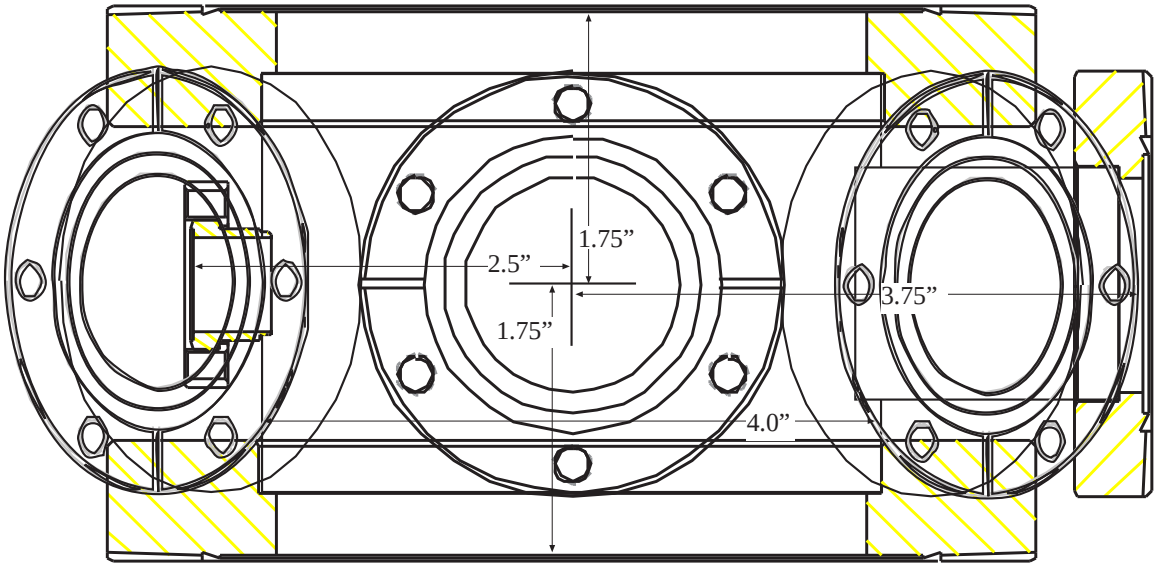

Bibliography

[1] M. H. Anderson, J. R. Ensher, M. R. Matthews, C. E. Wieman, and E. A. Cornell. Observation of Bose-Einstein Condensation in a Dilute Atomic Vapor. *Science*, 269(5221):198–201, 1995.

[2] A. Ashkin. Trapping of Atoms by Resonance Radiation Pressure. *Phys. Rev. Lett.*, 40(12):729–732, 1978.

[3] Z. W. Barber, C. W. Hoyt, C. W. Oates, L. Hollberg, A. V. Taichenachev, and V. I. Yudin. Direct Excitation of the Forbidden Clock Transition in Neutralˆ{174} Yb Atoms Confined to an Optical Lattice. *Phys. Rev. Lett.*, 96(8):83002, 2006.

[4] C. C. Bradley, C. A. Sackett, and R. G. Hulet. Bose-Einstein Condensation of Lithium: Observation of Limited Condensate Number. *Phys. Rev. Lett.*, 78(6):985–989, 1997.

[5] Gavin K. Brennen, Carlton M. Caves, Poul S. Jessen, and Ivan H. Deutsch. Quantum logic gates in optical lattices. *Phys. Rev. Lett.*, 82:1060, 1999.

[6] Gretchen K. Campbell, Jongchul Mun, Micah Boyd, Patrick Medley, Aaron E. Leanhardt, Luis G. Marcassa, David E. Pritchard, and Wolfgang Ketterle. Imaging the mott insulator shells by using atomic clock shifts. *Science*, 313:649–652, 2006.

[7] D. Cassettari, B. Hessma, R. Folman, T. Maier, and J. Schmiedmayer. Beam splitter for guided atoms. *Phys. Rev. Lett.*, 85:54835487, 2000.

[8] D. E. Chang, Jun Ye, and M. D. Lukin. Controlling dipole-dipole frequency shifts in a lattice-based optical atomic clock. *Phys. Rev. A*, 69:023810, 2004.

[9] S. Chu, J. E. Bjorkholm, A. Ashkin, and A. Cable. Experimental Observation of Optically Trapped Atoms. *Phys. Rev. Lett.*, 57(3):314–317, 1986.

[10] Y. Colombe, E. Knyazchyan, O. Morizot, B. Mercier, V. Lorent, and H. Perrin. Ultracold atoms confined in rf-induced two-dimensional trapping potentials. *Europhys. Lett.*, 67:593, 2004.

[11] E. A. Cornell, R. M. Weisskoff, K. R. Boyce, R. W. Flanagan Jr, G. P. Lafyatis, and D. E. Pritchard. Cornell et al. reply. *Phys. Rev. Lett.*, 64(17):2099–2099, 1990.

[12] K. B. Davis, M. O. Mewes, M. R. Andrews, N. J. van Druten, D. S. Durfee, D. M. Kurn, and W. Ketterle. Bose-Einstein Condensation in a Gas of Sodium Atoms. *Phys. Rev. Lett.*, 75(22):3969–3973, 1995.

[13] Kendall B. Davis, Marc-Oliver Mewes, Michael A. Joffe, Michael R. Andrews, and Wolfgang Ketterle. Evaporative cooling of sodium atoms. *Phys. Rev. Lett.*, 74(26):5202–5205, Jun 1995.

[14] C. Degenhardt, H. Stoehr, C. Lisdat, G. Wilpers, H. Schnatz, B. Lipphardt, T. Nazarova, P.E. Pottie, U. Sterr, J. Helmcke, and F. Riehle. Calcium optical frequency standard with ultracold atoms: Approaching 10ˆ{- 15} relative uncertainty. *Physical Review A*, 72(6):62111, 2005.

[15] B. DeMarco, C. Lannert, S. Vishveshwara, and T.C. Wei. Structure and stability of Mott-insulator shells of bosons trapped in an optical lattice. *Phys. Rev. A*, 71(6):63601, 2005.

[16] S. A. Diddams, Th. Udem, J. C. Bergquist, E. A. Curtis, R. E. Drullinger, L. Hollberg, W. M. Itano, W. D. Lee, C. W. Oates, K. R. Vogel, and D. J. Wineland. An Optical Clock Based on a Single Trapped 199 Hg Ion. *Science*, 293(5531):825–828, 2001.

[17] S. Eriksson, F. Ramirez-Martinez, E. A. Curtis, B. E. Sauer, P. W. Nutter, E. W. Hill, and E. A. Hinds. Micron-sized atom traps made from magneto-optical thin films. *cond-mat/0406482*, 2004.

[18] W. Ertmer, R. Blatt, J. L. Hall, and M. Zhu. Laser Manipulation of Atomic Beam Velocities: Demonstration of Stopped Atoms and Velocity Reversal. *Physical Review Letters*, 54(10):996–999, 1985.

[19] Chad Fertig and Kurt Gibble. Measurement and cancellation of the cold collision frequency shift in an 87 rb fountain clock. *Phys. Rev. Lett.*, 85:1622–1625, 2000.

[20] M. P. A. Fisher, P. B. Weichman, G. Grinstein, and D. S. Fisher. *Phys. Rev. B*, 40:546, 1989.

[21] D. G. Fried, T. C. Killian, L. Willmann, D. Landhuis, S. C. Moss, D. Kleppner, and T. J. Greytak. Bose-einstein condensation of atomic hydrogen. *Phys. Rev. Lett.*, 81:3811–3814, 1998.

[22] Fabrice Gerbier, Artur Widera, Simon Fölling, Olaf Mandel, Tatjana Gericke, and Immanuel Bloch. Interference pattern and visibility of a mott insulator. *Phys. Rev. A*, 72:053606, 2005.

[23] Fabrice Gerbier, Artur Widera, Simon Fölling, Olaf Mandel, Tatjana Gericke, and Immanuel Bloch. Phase coherence of an atomic mott insulator. *Phys. Rev. Lett.*, 95:050404, 2005.

[24] Markus Greiner. *Ultracold quantim gases in three-dimensional optical lattice potentials*. PhD thesis, Ludwig-Maximilians-Universit"at München, München, Germany, 2003.

[25] A. Griesmaier, J. Werner, S. Hensler, J. Stuhler, and T. Pfau. Bose-Einstein Condensation of Chromium. *Physical Review Letters*, 94(16):160401, 2005.

[26] T. L. Gustavson, A. P. Chikkatur, A. E. Leanhardt, A. Görlitz, S. Gupta, D. E. Pritchard, and W. Ketterle. Transport of bose-einstein condensates with optical tweezers. *Phys. Rev. Lett*, 88:020401, 2002.

[27] B. V. Hall, S. Whitlock, F. Scharnberg, P. Hannaford, and A. Sidorov. A permanent magnetic film atom chip for boseeinstein condensation. *J. Phys. B: At. Mol. Opt. Phys.*, 39:27–36, 2005.

[28] W. Hänsel, P. Hommelhoff annd T. W. Hänsch, and J. Reichel. Bose-einstein condensation on a microelectronic chip. *Nature*, 413:498–501, 2001.

[29] H.F. Hess. Evaporative cooling of magnetically trapped and compressed spin-polarized hydrogen. *Physical Review B*, 34(5):3476–3479, 1986.

[30] E. A. Hinds and I. G. Hughes. Magnetic atom optics: mirrors, guides, traps, and chips for atoms. *J. Phys. D*, 32:R119, 1999.

[31] Feng-Lei Hong, Masao Takamoto, Ryoichi Higashi, Yasuhiro Fukuyama annd Jie Jiang, and Hidetoshi Katori. Frequency measurement of a sr lattice clock using an si-second-referenced optical frequency comb linked by a global positioning system (gps). *Optics Express*, 13:5253–5262, 2005.

[32] C. W. Hoyt, Z. W. Barber, C. W. Oates, T. M. Fortier, S. A. Diddams, and L. Hollberg. Observation and Absolute Frequency Measurements of theˆ{1} S_ {0}-ˆ{3} P_ {0} Optical Clock Transition in Neutral Ytterbium. *Phys. Rev. Lett.*, 95(8):83003, 2005.

[33] J D Jackson. *Classical Electrodynamics*. Wiley, New York, 3rd edn edition, 1998.

[34] D. Jaksch, C. Bruder, J. I. Cirac, C. W. Gardiner, and P. Zoller. *Phys. Rev. Lett.*, 81:3108, 1998.

[35] M. P. A. Jones, C. J. Vale, D. Sahagun, B. V. Hall, and E. A. Hinds. Spin coupling between cold atoms and the thermal fluctuations of a metal surface. *Phys. Rev. Lett*, 91:080401, 2003.

[36] Hidetoshi Katori, Masao Takamoto, V. G. Pal'chikov, and V. D. Ovsiannikov. Ultrastable optical clock with neutral atoms in an engineered light shift trap. *Phys. Rev. Lett.*, 91:173005, 2003.

[37] W. Ketterle, D. S. Durfee, and DM Stamper-Kurn. Making, probing and understanding Bose-Einstein condensates. *Varenna Summer school*, 1999.

[38] J. I. Kim, J. Schmeidmayer, and P. Schmelcher. Quantum scattering in quasi-one-dimensional cylindrical confinement. *Phys. Rev. A*, 72:042711, 2005.

[39] J. M. Kosterlitz and D. J. Thouless. Ordering, metastability and phase transitions in two-dimensional systems. *J. Phys. C*, 6(1181):12, 1973.

[40] D. C. Lau, R. J. McLean, A. I. Sidorov, D. S. Gough, J. Koperski, W. J. Rowlands, B. A. Sexton, G. I. Opat, and P. Hannaford. Magnetic mirrors with micron-scale periodicities for slowly moving neutral atoms. *J. Opt. B: Quantum Semiclass. Opt.*, 1:371–377, 1999.

[41] A. E. Leanhardt. *Microtraps and Waveguides for Bose-Einstein Condensates*. PhD thesis, Massachusetts Institute of Technology, Cambridge, Massachusetts, 2006.

[42] A.E. Leanhardt, Y. Shin, A.P. Chikkatur, D. Kielpinski, W. Ketterle, and D.E. Pritchard. Bose-einstein condensates near a microfabricated surface. *Phys. Rev. Lett*, 90:100404, 2002.

[43] P. Lemonde and P. Wolf. Optical lattice clock with atoms confined in a shallow trap. *Phys. Rev. A*, 72(3):33409, 2005.

[44] B. Lev, Y. Lassailly, C. Lee, A. Scherer, and H. Mabuchi. Atom mirror etched from a hard drive. *Appl. Phys. Lett.*, 83:395–397, 2003.

[45] Y. Lin, I. Teper, C. Chin, and V. Vuletić. Impact of the casimir-polder potential and johnson noise on bose-einstein condensate stability near surfaces. *Phys. Rev. Lett.*, 92:050404, 2004.

[46] Andrew D. Ludlow, Martin M. Boyd, Tanya Zelevinsky, Seth M. Foreman, Sebastian Blatt, Mark Notcutt, Tetsuya Ido, and Jun Ye. Systematic study of the 87 sr clock transition in an optical lattice. *Phys. Rev. Lett.*, 96:033003, 2006.

[47] Michael Robin Matthews. *Two-Component Bose-Einstein Condensation*. PhD thesis, University of Colorado, Boulder, Colorado, 1999.

[48] G. Modugno, G. Ferrari, G. Roati, R. J. Brecha, A. Simoni, and M. Inguscio. Bose-Einstein Condensation of Potassium Atoms by Sympathetic Cooling. *Science*, 294(5545):1320–1322, 2001.

[49] C. W. Oates, E. A. Curtis, and L. Hollberg. Improved short-term stability of optical frequency standards: approaching 1 Hz in 1 s with the Ca standard at 657 nm. *Opt. Lett.*, 25(21):1603–1605, 2000.

[50] M. Olshanii. Atomic scattering in the presence of an external confinement and a gas of impenetrable bosons. *Phys. Rev. Lett.*, 81(5):938–941, Aug 1998.

[51] H. Ott, J. Fortagh, G. Schlotterbeck, A. Grossmann, and C. Zimmermann. Bose-einstein condensation in a surface microtrap. *Phys. Rev. Lett.*, 87:230401, 2001.

[52] CP Pearman, CS Adams, SG Cox, PF Griffin, DA Smith, and IG Hughes. Polarization spectroscopy of a closed atomic transition: applications to laser frequency locking. *Journal of Physics B Atomic Molecular and Optical Physics*, 35(24):5141–5151, 2002.

[53] F. Pereira Dos Santos, J. Léonard, J. Wang, CJ Barrelet, F. Perales, E. Rasel, CS Unnikrishnan, M. Leduc, and C. Cohen-Tannoudji. Bose-Einstein Condensation of Metastable Helium. *Phys. Rev. Lett.*, 86(16):3459–3462, 2001.

[54] F. Pereira Dos Santos, H. Marion, S. Bize, Y. Sortais, A. Clairon, and C. Salomon. Controlling the cold collision shift in high precision atomic interferometry. *Phys. Rev. Lett.*, 89(23):233004, 2002.

[55] H. Perrin, Y. Colombe, B. Mercier, V. Lorent, and C. Henkel. A bose-einstein condensate bouncing off a rough mirror. *Journal of Physics: Conference Series*, 19:151–157, 2005.

[56] Wolfgang Petrich, Michael H. Anderson, Jason R. Ensher, and Eric A. Cornell. Stable, tightly confining magnetic trap for evaporative cooling of neutral atoms. *Phys. Rev. Lett.*, 74(17):3352–3355, Apr 1995.

[57] W.D. Phillips and H. Metcalf. Laser Deceleration of an Atomic Beam. *Physical Review Letters*, 48(9):596–599, 1982.

[58] T. M. Roach, H. Abele, M. G. Boshier, H. L. Grossman, K. P. Zetie, and E. A. Hinds. Realization of a magnetic mirror for cold atoms. *Phys. Rev. Lett.*, 75:629632, 1995.

[59] C. Salomon, Y. Sortais, S. Bize, M. Abgrall, S. Zhang, C. Nicolas, C. Mandache, P. Lemonde, P. Laurent, G. Santarelli, A. Clairon, N. Dimarcq, P. Petit, A. Mann, A. Luiten, and S. Chang. Proceedings of the 17th international conference on atomic physics. page 23. ICAP 2000, American Institute of Physics, 2000.

[60] V. A. Sautenkov, H. van Kampen, E. R. Eliel, and J. P. Woerdman. Dipole-dipole broadened line shape in a partially excited dense atomic gas. *Phys. Rev. Lett.*, 77:3327–3330, 1996.

[61] S. Scheel, P. K. Rekdal, P. L. Knight, and E. A. Hinds. Atomic spin decoherence near conducting and superconducting films. *Phys. Rev. A*, 72:042901, 2005.

[62] D. Schneble, Y. Torii, M. Boyd, E.W. Streed, D.E. Pritchard, and W. Ketterle. The Onset of Matter-Wave Amplification in a Superradiant Bose-Einstein Condensate. *Science*, 300(5618):475–478, 2003.

[63] Dominik Schneble, Yoshio Torii, Micah Boyd, Erik W. Streed, David E. Pritchard, and Wolfgang Ketterle. The onset of matter-wave amplification in a superradiant bose-einstein condensate. *Science*, 300:475–478, 2003.

[64] Y. Shin, G. B. Jo, T. A. Pasquini, W. Ketterle, D. E. Pritchard, M. Vengalattore, and M. Prentiss. Interference of bose-einstein condensates on an atom chip. *Phys. Rev. A*, 72:021604, 2005.

[65] A. I. Sidorov, R. J. McLean, W. J. Rowlands, D. C. Lau annd J. E. Murphy annd M. Walkiewicz, G. I. Opat, and P. Hannaford. Specular reflection of cold caesium atoms from a magnetostatic mirror. *Quantum Semiclass. Opt.*, 8:713–725, 1996.

[66] C. D. J. Sinclair, E. A. Curtis, I. L. Garcia, J. A. Retter, B. V. Hall, S. Eriksson, B. E. Sauer, and E. A. Hinds. Bose-einstein condensation on a permanent-magnet atom chip. *Phys. Rev. A*, 72:031603, 2005.

[67] Y. Sortais, S. Bize, M. Abgralland S. Zhang, C. Nicolas, C. Mandache, P. Lemonde, P. Laurennt annd G. Santarelli annd N. Dimarcq, P. Petit, A. Clairon, A. Mann, A. Luiten, S. Channg, and C. Salomon. Cold atom clocks. *Phys. Scr.*, T95:50–57, 2001.

[68] D.M. Stamper-Kurn. *Peeking and poking at a new quantum fluid: Studies of gaseous Bose-Einstein condensates in magnetic and optical traps*. PhD thesis, Massachusetts Institute of Technology, Cambridge, Massachusetts, 2000.

[69] Daniel A. Steck. Rubidium 87 D Line Data, revision 1.6. *http://steck.us/alkalidata*, 2003.

[70] E. W. Streed. *87 Rubidium Bose-Einstein Condensates: Machine Construction and Quantum Zeno Experiments*. PhD thesis, Massachusetts Institute of Technology, Cambridge, Massachusetts, 2006.

[71] Erik W Streed, Ananth P Chikkatur, Todd L Gustavson, Micah Boyd, Yoshio Torii, Dominik Schneble, Gretchen K Campbell, David E Pritchard, and Wolfgang Ketterle. Large atom number Bose-Einstein condensate machines. *Rev. Sci. Instr.*, 77:023106, 2006.

[72] Erik W Streed, Ananth P Chikkatur, Todd L Gustavson, Micah Boyd, Yoshio Torii, Dominik Schneble, Gretchen K Campbell, David E Pritchard, and Wolfgang Ketterle. Large atom number Bose-Einstein condensate machines. *Rev. Sci. Instr.*, 77:023106, 2006.

[73] Masao Takamoto, Feng-Lei Hong annd Ryoichi Higashi, and Hidetoshi Katori. An optical lattice clock. *Nature*, 435:321–324, 2005.

[74] Y. Takasu, K. Maki, K. Komori, T. Takano, K. Honda, M. Kumakura, T. Yabuzaki, and Y. Takahashi. Spin-Singlet Bose-Einstein Condensation of Two-Electron Atoms. *Phys. Rev. Lett.*, 91(4):40404, 2003.

[75] C. Cohen Tannoudji and B. Diu annd F. Laloë. *Quantum Mechanics*. Wiley, New York, 1968.

[76] Th. Udem, S. A. Diddams, K. R. Vogel, C. W. Oates, E. A. Curtis, W. D. Lee, W. M. Itano, R. E. Drullinger, J. C. Bergquist, and L. Hollberg. Absolute frequency measurements of the hg^+ and ca optical clock transitions with a femtosecond laser. *Phys. Rev. Lett.*, 86(22):4996–4999, May 2001.

[77] Th. Udem, R. Holzwarth, and T. W. Hänsch. Optical frequency metrology. *Nature*, 416:233–237, 2002.

[78] T. Weber, J. Herbig, M. Mark, H. C. Nagerl, and R. Grimm. Bose-Einstein Condensation of Cesium. *Science*, 299(5604):232–235, 2003.

[79] M. White, H. Gao, M. Pasienski, and B. Demarco. Bose-einstein condensates in rf-dressed adiabatic potentials. *http://arxiv.org/abs/cond-mat/0605393*, 2006.

[80] G. Wilpers, T. Binnewies, C. Gegenhardt, U. Sterr, J. Helmche, and F. Riehle. Optical clock with ultracold neutral atoms. *Phys. Rev. Lett.*, 89:230801, 2002.

[81] Y. Yoshikawa, T. Umeki, T. Mukae, Y. Torii, and T. Kuga. Frequency stabilization of a laser diode with use of light-induced birefringence in an atomic vapor. *APPLIED OPTICS*, 42(33):6645–6649, 2003.

[82] O. Zobay and B. M. Garraway. Atom trapping and two-dimensional bose-einstein condensates in field-induced adiabatic potentials. *Phys. Rev. A*, 69:023605, 2004.

[83] O. Zobay and BM Garraway. Two-Dimensional Atom Trapping in Field-Induced Adiabatic Potentials. *Phys. Rev. Lett.*, 86(7):1195–1198, 2001.